

Computational Modelling Techniques to Determine Patellofemoral Joint Loads

by
Julian David Atkinson

Thesis presented in partial fulfilment of the requirements for the degree of Master of Engineering (Mechanical) in the Faculty of Engineering at Stellenbosch University



UNIVERSITEIT
iYUNIVESITHI
STELLENBOSCH
UNIVERSITY

100
1918 · 2018

Supervisor: Dr J.H. Müller

March 2018

Declaration

By submitting this thesis electronically, I declare that the entirety of the work contained therein is my own, original work, that I am the sole author thereof (save to the extent explicitly otherwise stated), that reproduction and publication thereof by Stellenbosch University will not infringe any third party rights and that I have not previously in its entirety or in part submitted it for obtaining any qualification.

Name: Julian David Atkinson

Date: March 2018

Abstract

Neuromechanical computational tools provide insight into the loads around human joints that cannot be measured in vivo. An automated computational pipeline, designed to run with minimal user intervention that outputs joint kinematics, joint moments, muscle parameters and muscle forces is outlined in this project. The tool uses OpenSim (Simtk-confluence.stanford.edu, 2017) to determine the inputs into CEINMS (CEINMS Simtk.org, 2017), which uses this information in conjunction with the electromyographic (EMG) data to inform a neuromusculoskeletal model that outputs muscle forces and adjusted muscle parameters. These computational tools are open source and freely available. Thirty patellofemoral pain (PFP) subjects were tested during the experimental phase of the project with the EMG, ground reaction force (GRF) and kinematic data of five of the subjects, before and after eight weeks of physiotherapeutic intervention, acting as an input to the tool. The results of the tool can then be used to quantify changes in patients' underlying biomechanics to provide insight into proposed risk factors of PFP.

Before clinical questions can be answered using the results obtained from data, it is crucial to determine whether the outputs of the tool are clinically relevant, and to what extent experimental and modelling errors influence the results. The processing techniques used to filter and smooth the GRF, marker and EMG data is investigated. It is shown that filtering the marker and force plate data at different frequencies introduces an artefact at the point of impact for the knee joint moment. Changing EMG filtering frequency is shown to affect the magnitude of muscles forces produced by CEINMS. A sensitivity of the CEINMS optimiser to biarticulate muscles is identified. However, the exact causal relationship is not known and requires further research. The muscle force results of CEINMS are also affected by changing the EMG normalisation technique. Using maximum voluntary contractions (MVC) to normalise the EMGs is shown to produce muscle forces of a different magnitude to using walking trial maximums (WTM).

Finally, the results across sessions showed high repeatability for the kinematics, dynamics and muscle forces with a coefficient of determination (COD), R^2 of 0.93, 0.93 and 0.83 respectively. All the subjects showed significant change in their muscle forces across sessions ($P < 0.05$) for the majority of their muscles, with only subject AKP 29 showing significant change in less than 14 of the 16 tested muscles. The muscle force results produced shapes that are comparable to literature. While it is concluded that realistic muscle forces are produced, the full extent to which the modelling and experimental errors account for the changes seen between subjects across sessions needs to be further researched. This project presents a semi-automated computational tool that enables joint moment and

muscle force estimation from motion laboratory gait data. Recommendations on data capturing, storage and processing are outlined, which are applicable for related studies requiring biomechanical analysis of human joints.

Uittreksel

Neuro-meganiese numeriese metodes kan gebruik word om laste in die menslike gewrig wat nie in-vivo gemeet kan word nie te beraam. 'n Outomatiese berekeningspyplyn wat minimale gebruiker intervensie benodig, is ontwikkel. Die uittree van die pyplyn is kinematika, spier parameters en spier kragte. Die metode maak van OpenSim (Simtk-confluence.stanford.edu, 2017) gebruik om insette vir CEINMS (CEINMS Simtk.org, 2017) te genereer. Hierdie inligting word dan gebruik om in samewerking met EMG's 'n neuro-spier-skelet model te dryf wat spierkrag en parameters beraam. Die berekeningspyplyn is gebaseer op gratis sagteware wat vrylik bekombaar is. Dertig patellofemorale pyn (PFP) pasiënte is tydens die eksperimentele fase van die projek getoets. Die elektromiografiese (EMG), grond reaksie krag (GRK) en kinematiese data van vyf van die pasiënte, voor en na agt weke se fisioterapeutiese intervensie, is gebruik in die studie. Die resultate van die berekeningspyplyn is gebruik om veranderinge in pasiënte se onderliggende biomeganika te kwantifiseer om sodoende insig te kry in voorgestelde risiko faktore van PFP.

Voordat kliniese vrae beantwoord kon word met behulp van die data, was dit noodsaaklik om vas te stel of die uitsette van die berekeningspyplyn klinies relevant is en in watter mate eksperimentele en modelleringsfoute die resultate beïnvloed. Die verwerkingstegnieke wat gebruik is om die GRK-, merker- en EMG-data te filter is ondersoek. Daar is gevind dat die filter parameters van die merker en kragplaat data by verskillende frekwensies 'n artefak in kniegewrig momente tydens die punt van impak veroorsaak. Die verandering van EMG filter frekwensie het getoon dat die grootte van spierkrag wat deur CEINMS voorspel is, beïnvloed word. Die CEINMS-optimeerder gee teenstrydige resultate vir twee-gewrig-spiere. Die oorsaak in hierdie verband kon nie bepaal word nie en vereis verdere ondersoek. Die spierkrag uitslae vanaf CEINMS word ook beïnvloed deur die EMG normaliseringstegniek: Die gebruik van maksimum vrywillige kontraksies (MVK) in teenstelling met maksimum-binne-loppe-waardes (MBLW) lewer spierkragte van verskillende groottes.

Die uitslae oor sessies toon hoë herhaalbaarheid vir die kinematika, dinamika en spierkragte met 'n koëffisiënt van vasstelling (R^2) van 0.93, 0.93 en 0.83 onderskeidelik. Al die pasiënte het 'n beduidende verandering in hul spierkrag oor die sessies ($P < 0.05$) ondergaan met die uitsondering van een pasiënt (AKP 29) wat 'n beduidende verandering in minder as 14 van die 16 spiere toon. Die spierkrag resultate is goed vergelykbaar met die literatuur. Terwyl daar tot die gevolgtrekking gekom word dat realistiese spierkragte geproduseer is, moet die volledige mate waarin die modellerings- en eksperimentele foute verantwoordelik is vir die veranderinge tussen pasiënte oor sessies verder ondersoek word. Hierdie projek bied 'n semi-outomatiese berekeningspyplyn aan wat spierkrag beraming aan die

hand van bewegingslaboratorium data bemoontlik. Aanbevelings rakende data versameling, berging en verwerking word uiteengesit, wat van toepassing is op verwante studies wat biomeganiese analise van menslike gewrigte vereis.

Acknowledgements

I would like to express my gratitude to the following for their contribution to this project:

- Dr Cobus Müller, thank you for your guidance, advice and support throughout this project and for allowing me to the opportunity to do a Masters under your supervision. The insight I gained has been invaluable.
- Dr John Cockroft, thank you for your valuable insight, and the interest you took in my project. I appreciate the extra time spent on my project.
- Thank you to my fellow BERG members. The motivation, insight and entertainment provided an excellent research environment.
- Thank you to my friends and family, to my parents and Megan, thank you for the constant support over the last two years.
- Finally, thank you to the National Research Foundation for providing the funding that made this project possible.

Table of Contents

List of Figures	ix
List of Tables	xiv
Nomenclature	xv
1. Introduction	1
1.1. Background	1
1.2. Motivation	2
1.3. Objectives	3
1.4. Thesis outline.....	4
2. Literature Review	5
2.1. The lower limb	5
2.1.1. Anatomical definitions	5
2.1.2. Human Gait	5
2.1.3. The hip joint	7
2.1.4. The knee joint.....	8
2.1.5. The ankle joint.....	10
2.2. Biomechanical Information	11
2.2.1. Electromyography	11
2.2.2. Kinematics and kinetics	13
2.3. The OpenSim model	15
2.3.1. Joint geometry.....	15
2.3.2. Muscle geometry.....	17
3. Experimental procedure	18
3.1. Apparatus.....	18
3.1.1. EMG measurements.....	18
3.1.2. Motion capturing.....	19
3.1.3. Ground reaction force measurement	21
3.2. Subjects.....	22
3.3. Laboratory output.....	24
4. Pre-processing	25
4.1. Acquisition	25
4.2. C3D to MAT.....	26
4.3. Data processing	27
4.4. Static processing	27

5. OpenSim	29
5.1. Batch processing	29
5.2. Scaling	30
5.3. Inverse Kinematics	32
5.4. Inverse Dynamics	33
5.5. Residual Reduction Algorithm	34
5.6. Computed Muscle control	36
5.7. Analyses Tool	38
5.8. OpenSim results	39
5.8.1. Scaling	40
5.8.2. Inverse Kinematics	41
5.8.3. Inverse Dynamics	44
5.8.4. Residual Reduction Algorithm	46
5.8.5. Force plate and motion data filtering	47
5.8.6. Computed Muscle Control	52
6. EMG Informed Neuromusculoskeletal modelling software.....	56
6.1. Neuromusculoskeletal models	56
6.1.1. Activation dynamics	56
6.1.2. Contraction dynamics.....	57
6.2. Calibration and Execution.....	59
6.2.1. Calibration optimisation algorithm	61
6.2.2. Running Calibration and Execution	62
6.3. EMG processing	65
6.3.1. Processing techniques in literature.....	65
6.3.2. Processing method	66
6.3.3. Results of EMG processing	67
6.4. Results of CEINMS.....	74
7. Conclusion	78
7.1. Outcomes of the study	78
7.2. Future work	82
7.3. Contributions to the field	83
References.....	84
Appendices.....	93
Appendix A. Marker labels	94
Appendix B. OpenSim results	95
B.1. Inverse Kinematics.....	95

B.2. Inverse Dynamics.....	96
B.3. Force plate and EMG processing.....	97
B.4. Kinematics comparison	107
Appendix C. Simulated Annealing.....	111
Appendix D. EMG processing.....	113
D.1. EMG processing results	113
D.2. EMG normalisation results.....	117
Appendix E. Muscle force results.....	123
Appendix F. Folder layout	124
Appendix G. Computational pipeline diagrams	126
G.1. MOtoNMS	126
G.2. OpenSim	129
G.3. CEINMS.....	131

List of Figures

Figure 1: Anatomical planes and rotations (adapted from Samuelparsons.co.uk, 2017)	5
Figure 2: Human gait cycle (adapted from Vaughan <i>et al.</i> , 1999).....	6
Figure 3: The hip joint (adapted from Schmidler, 2017)	7
Figure 4: The knee joint (adapted from Schmidler, 2017)	8
Figure 5: The ankle joint (Clinical Gate, 2017)	10
Figure 6: The underlying motor control mechanisms, motor units and their components (Merletti <i>et al.</i> , 2004).....	11
Figure 7: Marker set frames and joint centre frames (Capozzo <i>et al.</i> , 2005).....	14
Figure 8: Components of ground reaction forces (adapted from Whittle, 2007) ...	15
Figure 9: Location of the reference frames within rigid segments (Delp <i>et al.</i> , 1990)	16
Figure 10: Sagittal plane knee model created by Delp <i>et al.</i> (1990)	17
Figure 11: EMG designation.....	18
Figure 12: Marker positions for mocap	20
Figure 13: Laboratory layout and reference frames.....	21
Figure 14: Pre-processing flow diagram	25
Figure 15: Motion Lab force plate and global axis	Error! Bookmark not defined.
Figure 16: Computational pipeline flow diagram	29
Figure 17: Scale factor calculation (Simtk-confluence.stanford.edu, 2017)	30
Figure 18: RRA schematic (Anderson <i>et al.</i> , 2006)	34
Figure 19: CMC schematic (Thelen <i>et al.</i> , 2006)	36
Figure 20: Subject comparison of IK averages for session one	42
Figure 21: Subject comparison of IK averages for session four.....	43
Figure 22: Session comparison of the IK for subject AKP 16	43
Figure 23: Subject comparison of ID averages for session one	44
Figure 24: Subject comparison of ID averages for session four	45
Figure 25: Session comparison of the ID for subject AKP 16.....	46
Figure 26: Knee moment and FY residual of AKP 29 Session one	50
Figure 27: Bland and Altman plot for AKP 29 left knee moment during session one	51

Figure 28: Knee moment and FY residual AKP 03 Session one	51
Figure 29: Bland and Altman plot for AKP 03 right knee moment during session one	52
Figure 30: AKP 17 Session one kinematics comparison	54
Figure 31: AKP 17 Session four kinematics comparison	55
Figure 32: Flow diagram showing the relationship between EMGs, Activation Dynamics and Contraction Dynamics (Ceseracciu <i>et al.</i> , 2015)	56
Figure 33: Active and passive force-length curves (Thelen. 2003).....	58
Figure 34: Flow diagram of the calibration procedure.....	60
Figure 35: Flow diagram of execution procedure	60
Figure 36: Calibrated EMG Informed Neuromusculoskeletal modelling flow diagram	62
Figure 37: EMG processing flow diagram	67
Figure 38: Muscle forces and EMGs of AKP 29 filtered at a high-pass cut-off of 30 Hz for the unaffected leg (right) during session one	68
Figure 39: Muscle forces and EMGs of AKP 29 filtered at a high-pass cut-off of 40 Hz during for the unaffected leg (right) of session one.....	69
Figure 40: Muscle forces and EMGs of AKP 29 filtered at a low-pass cut-off of 6 Hz during for the unaffected leg (right) of session one.....	70
Figure 41: Mean EMG at each frequency normalised by the maximum at the frequency	71
Figure 42: Muscle forces for AKP 17 using EMGs normalised using MVC vs WTM.	72
Figure 43: MVC vs WTM normalisation values for session one	73
Figure 44: Legend for the muscle force plots	75
Figure 45: AKP 03 muscle forces.....	75
Figure 46: AKP 16 muscle forces.....	76
Figure 47: AKP 29 muscle forces.....	76
Figure 48: Session comparison of the IK for subject AKP 03	95
Figure 49: Session comparison of the IK for subject AKP 17	95
Figure 50: Session comparison of the IK for subject AKP 29	95
Figure 51: Session comparison of the IK for subject AKP 30	96
Figure 52: Session comparison of the ID for subject AKP 03.....	96
Figure 53: Session comparison of the ID for subject AKP 17.....	96

Figure 54: Session comparison of the ID for subject AKP 29.....	97
Figure 55: Session comparison of the ID for subject AKP 30.....	97
Figure 56: Knee moment and FY residual of AKP 03 session one	97
Figure 57: Bland and Altman plot Subject AKP 03 session one left leg.....	98
Figure 58: Bland and Altman plot Subject AKP 03 session one right leg.....	98
Figure 59: Knee moment and FY residual of AKP03 session four	98
Figure 60: Bland and Altman plot Subject AKP 03 session four left leg	99
Figure 61: Bland and Altman plot Subject AKP 03 session four right leg	99
Figure 62: Knee moment and FY residual of AKP 16 session one	99
Figure 63: Bland and Altman plot Subject AKP 16 session one left leg.....	100
Figure 64: Bland and Altman plot Subject AKP 16 session one right leg.....	100
Figure 65: Knee moment and FY residual of AKP 16 session four	100
Figure 66: Bland and Altman plot Subject AKP 16 session four left leg	101
Figure 67: Bland and Altman plot Subject AKP 16 session four right leg	101
Figure 68: Knee moment and FY residual of AKP 17 session one	101
Figure 69: Bland and Altman plot Subject AKP 17 session one left leg.....	102
Figure 70: Bland and Altman plot Subject AKP 17 session one right leg.....	102
Figure 71: Knee moment and FY residual of AKP17 session four.....	102
Figure 72: Bland and Altman plot Subject AKP 17 session four left leg	103
Figure 73: Bland and Altman plot Subject AKP 17 session four right leg	103
Figure 74: Knee moment and FY residual of AKP29 session one	103
Figure 75: Bland and Altman plot Subject AKP 29 session one left leg.....	104
Figure 76: Bland and Altman plot Subject AKP 29 session one right leg.....	104
Figure 77: Knee moment and FY residual of AKP29 session four	104
Figure 78: Bland and Altman plot Subject AKP 29 session four left leg	105
Figure 79: Bland and Altman plot Subject AKP 29 session four right leg	105
Figure 80: Knee moment and FY residual of AKP30 session one	105
Figure 81: Bland and Altman plot Subject AKP 30 session one left leg.....	106
Figure 82: Bland and Altman plot Subject AKP 30 session one right leg.....	106
Figure 83: Knee moment and FY residual of AKP30 session four.....	106
Figure 84: Bland and Altman plot Subject AKP 30 session four left leg	107

Figure 85: Bland and Altman plot Subject AKP 30 session four right leg	107
Figure 86: AKP 03 Session one kinematics comparison	107
Figure 87: AKP 03 Session four kinematics comparison	108
Figure 88: AKP 16 Session one kinematics comparison	108
Figure 89: AKP 16 Session four kinematics comparison	108
Figure 90: AKP 17 Session one kinematics comparison	109
Figure 91: AKP 17 Session four kinematics comparison	109
Figure 92: AKP 29 Session one kinematics comparison	109
Figure 93: AKP 29 Session four kinematics comparison	110
Figure 94: AKP 30 Session one kinematics comparison	110
Figure 95: AKP 30 Session four kinematics comparison	110
Figure 96: Muscle forces and EMGs of AKP 29 filtered at a high-pass cut-off of 30 Hz for the affected leg (left) during session one	113
Figure 97: Muscle forces and EMGs of AKP 29 filtered at a high-pass cut-off of 40 Hz for the affected leg (left) during session one	113
Figure 98: Muscle forces and EMGs of AKP 29 filtered at a low-pass cut-off of 6 Hz for the affected leg (left) during session one	114
Figure 99: Muscle forces and EMGs of AKP 30 filtered at a high-pass cut-off of 30 Hz for the affected leg (left) during session one	114
Figure 100: Muscle forces and EMGs of AKP 30 filtered at a high-pass cut-off of 40 Hz for the affected leg (left) during session one	115
Figure 101: Muscle forces and EMGs of AKP 30 filtered at a low-pass cut-off of 6 Hz for the affected leg (left) during session one	115
Figure 102: Muscle forces and EMGs of AKP 30 filtered at a high-pass cut-off of 30 Hz for the unaffected leg (right) during session one	116
Figure 103: Muscle forces and EMGs of AKP 30 filtered at a high-pass cut-off of 40 Hz for the unaffected leg (right) during session one	116
Figure 104: Muscle forces and EMGs of AKP 30 filtered at a low-pass cut-off of 6 Hz for the unaffected leg (right) during session one	117
Figure 105: AKP 03 WTM vs MVC normalisation	117
Figure 106: AKP 16 WTM vs MVC normalisation	118
Figure 107: Muscle forces for AKP 29 using EMGs normalised using MVC vs WTM	118
Figure 108: BA plot for AKP 03 session one normalisation muscle forces	119

Figure 109: BA plot for AKP 03 session four normalisation muscle forces	119
Figure 110: BA plot for AKP 16 session one normalisation muscle forces	120
Figure 111: BA plot for AKP 16 session four normalisation muscle forces	120
Figure 112: BA plot for AKP 17 session one normalisation muscle forces	121
Figure 113: BA plot for AKP 17 session four normalisation muscle forces	121
Figure 114: BA plot for AKP 29 session one normalisation muscle forces	122
Figure 115: BA plot for AKP 29 session four normalisation muscle forces	122
Figure 116: Legend for the muscle force plots	123
Figure 117: AKP 17 muscle forces.....	123
Figure 118: AKP 30 muscle forces.....	123
Figure 119: Outer project folder	124
Figure 120: Session folder layout within CEINMS Data folder	124
Figure 121: Session folder layout within Elaborated Data	125
Figure 122: MO to NMS outer code flow diagram	126
Figure 123: C3D2MAT flow diagram.....	127
Figure 124: Acquisition flow diagram	127
Figure 125: Data Processing flow diagram	128
Figure 126: Static Interface flow diagram	128
Figure 127: OpenSim flow diagram	129
Figure 128: Scale flow diagram.....	130
Figure 129: IK flow diagram	130
Figure 130: ID flow diagram.....	130
Figure 131: RRA flow diagram	130
Figure 132: CMC flow diagram	131
Figure 133: Analyse flow diagram	131
Figure 134: CEINMS outer flow diagram	131
Figure 135: Calibration flow diagram	132
Figure 136: Execution flow diagram	132

List of Tables

Table 1: Muscles responsible for movement in the hip	8
Table 2: Muscles responsible for movement in the knee	9
Table 3: Muscles responsible for ankle movement.....	10
Table 4: EMG electrode positions.....	19
Table 5: Marker position designation.....	20
Table 6: Subject details	23
Table 7: Force Plate frame local to global rotations.....	26
Table 8: Segment scaling marker pairs	31
Table 9: Scaling errors calculated in OpenSim	40
Table 10: Percentage change between segment scaling factors	41
Table 11: Inter-session coefficient-of-determination values for IK.....	44
Table 12: Inter-session coefficient of determination values for ID.....	46
Table 13: RRA maximum residual forces	47
Table 14: Force plate and marker low-pass cut-off frequencies.....	49
Table 15: CMC Residuals.....	53
Table 16: CMC Reserves.....	53
Table 17: Musculotendon Default values and changes.....	61
Table 18: Trials used for Calibration and Execution of CEINMS	64
Table 19: EMG cut-off frequencies	67
Table 20: Test decision value H , and P value for the muscle forces normalisation data for session one.....	73
Table 21: Coefficient of determination for the muscle forces	74
Table 22: Test decision value H , and P value for the muscle forces.....	77

Nomenclature

Variables

a_i	Body acceleration
$a_j(t)$	Activation of the muscle
A_j	Non-linear shape factor
C_1	Subject-specific parameter one
C_2	Subject-specific parameter two
C_j	Equality constraints
$C(q, \dot{q})$	Vector of Coriolis and centrifugal forces
d	Electromechanical delay
d_m	Muscle mapping element
e_1	Experimental marker distance
$e(t)$	Muscle excitation signal
$f_{act,i}$	Actuator forces
$f_{act,i}^{opt}$	Optimal actuator forces
F_{exp}	Experimentally measured ground reaction force
$F_{residual}$	Residual force
F_X	Residual force in X-direction
F_Y	Residual force in Y-direction
F_Z	Residual force in Z-direction
F^t	Tendon force
g	Gravitational constant
$G(q)$	Vector of gravitational forces
k_v	Velocity error gain
k_p	Position error gain
\vec{k}_v	Velocity control error gain
\vec{k}_p	Position control error gain
l_m	Instantaneous fibre length
l_t	Tendon length

l_{ts}	Tendon slack length
\tilde{l}_m	Fibre length
L_m^0	Optimal fibre length
m_1	Model marker distance
m_i	Body segment mass
M_X	Residual moment around X-axis
M_Y	Residual moment around Y-axis
M_Z	Residual moment around Z-axis
$M(q)$	System mass matrix
$M_{t,d,r}$	Predicted joint moments
$\overline{M}_{t,d,r}$	Experimental joint moments
$P(r, j)$	Penalty function
q	Vector of generalised coordinates
q_j	Coordinate value
$q_{ik}(t)$	Kinematics produced by Inverse Kinematics
\dot{q}	Generalised velocity
\ddot{q}	Generalised acceleration
\ddot{q}_j^*	CMC desired accelerations
q_j^{exp}	Weighted difference between the experimental coordinate
$\vec{q}_{rra}(t)$	Kinematics produced by Residual Reduction Algorithm.
R^2	Coefficient of determination
s	Scaling factor
$u_j(t)$	Neural activation
v^m	Fibre velocity
v^{max}	Maximum muscle contraction velocity
w_i	Marker weights
$x_i(q)$	Position of the model marker
x_i^{exp}	Weighted difference between the experimental marker position
α	Muscle gain coefficient
β_1	Recursive coefficients one
β_2	Recursive coefficients two

ϵ	Tendon strain
τ	Vector of generalised forces
ω_j	Coordinate weights
φ	Pennation angle
φ_0	Pennation angle at optimal length

Abbreviations

%BW	Percentage Body Weight
AJC	Ankle Joint Centre
ASIS	Anterior Superior Iliac Spine
BF	Bicep Femoris
BOPS	Batch OpenSim Processing Scripts
C3D	Coordinate three-dimensional
CAF	Central Analytical Facility
CEINMS	Calibrated EMG Informed Neuromusculoskeletal modelling software
CMC	Computed Muscle Control
COD	Coefficient of Determination
COM	Centre of Mass
COP	Centre of Pressure
DOF	Degree of Freedom
ECG	Electrocardiographic
EET	Equilibrium Elastic Tendon
EMG	Electromyography
GRF	Ground Reaction Forces
HJC	Hip Joint Centre
ID	Inverse Dynamics
IET	Integration Elastic Tendon
IK	Inverse Kinematics
KJC	Knee Joint Centre
LG	Lateral Gastrocnemius
PFP	Patellofemoral Pain
MG	Medial Gastrocnemius

MOCAP	Motion Capture
MTP	Metatarsophalangeal
MTU	Musculotendon Units
MU	Motor Unit
MVC	Maximum Voluntary Contraction
NMS	Neuromusculoskeletal
RF	Rectus Femoris
RMS	Root Mean Square
RRA	Residual Reduction Algorithm
ST	Semitendinosus
TA	Tibialis Anterior
VL	Vastus Lateralis
VM	Vastus Medialis
WLS	Weighted least-squares
WTM	Walking Trial Maximum
XML	Extensible Markup Language

1. Introduction

1.1. Background

Patellofemoral pain (PFP) is a common condition identified in orthopaedic practice. PFP is experienced in different pain locations and at different pain levels, making it difficult to define. It is characterised by a dull, aching pain in the anterior aspect of the knee (Hettrich and Lietchi, 2015; Witvrouw *et al.*, 2005). PFP is prevalent in - but not limited to - adolescents and females (Boling *et al.*, 2010). A primary healthcare facility in Cape Town found that out of 362 patients with peripheral or spinal joint pain, knee pain occurred in isolation in 13.3% of patients and an additional 56.6% of patients when combined with other joint pains (Parker and Jelsma, 2010). Symptoms of PFP can include pain during activities, which require repeated flexion and extension of the knee, and pain during extended periods of sitting. This pain limits PFP sufferers' mobility and impedes everyday activities such as kneeling, walking and stair ambulation (Hettrich and Lietchi, 2015).

The aetiology of PFP is still widely debated. The most common hypothesis is that PFP is caused by patella maltracking, although this is not a consistent finding (MacIntyre *et al.*, 2006). Individuals with patellofemoral pain were found to have higher PF joint stress profiles when compared with individuals without pain (Farroohki *et al.*, 2011). PFP is also believed to be linked to activity rather than being anthropometric. While the causes of PFP are multifactorial, predictors such as limited flexibility of the gastrocnemius and quadriceps, knee extension weakness and excessive knee valgus during landing have been identified (Pappas and Wong-Tom, 2012). Biomechanical risk factors (the focus of this study), identified during single leg squatting, include reduced peak hip internal rotation during gait, increased peak trunk ipsilateral lean, hip abduction and knee valgus. Due to difficulties in measurement and modelling, patellofemoral interface loads and pressures are a common under-researched aetiological factor. New models and measurement techniques have the potential to investigate these interface loads and pressures accurately.

Physiotherapy is the prevailing treatment for anterior knee pain. Pharmacological and surgical treatment has been inadequate, invasive and expensive. The nature of anterior knee pain is such that often the underlying causes are not immediately known, as such surgical treatment is only appropriate in cases where there is a well-defined structural abnormality that can be linked to anterior knee pain (Sanchis-Alfonso *et al.*, 2016). Limited health resources in South Africa create a necessity for cost-effective, evidence-based approaches. Coherent clinical evidence helps health

practitioners understand the effect of the intervention on the underlying physiological mechanisms.

Computational musculoskeletal modelling is an essential tool for modern biomechanical analysis. Modelling is an attempt to represent reality. It has the potential to be a powerful tool for improving the understanding of human mechanisms (Nigg and Herzog, 2007). Musculoskeletal modelling software and new optimisation-based tools (CEINMS Simtk.org, 2017) are capable of more accurately determining muscle forces and knee joint loads which cannot yet be measured *in vivo* (Besier *et al.*, 2005).

1.2. Motivation

Anterior knee pain is a widespread disorder, with a need for an evidence-based approach to the intervention. The most significant motivation for the parent study, for which this project forms a part, is the benefit it will provide to both patellofemoral pain sufferers as well as people responsible for treating the problem. To develop meaningful interventions, clinicians require evidence of the effect of treatment on the biomechanical system. Fundamental to better understanding the aetiology of knee pain is the quantification of changes in proposed risk factors (muscle activation patterns and loading distribution, stress magnitude and distribution) due to the selected treatment. Inter-subject variability should be eliminated by making each subject his/her control thereby improving the understanding of the underlying causal mechanisms and their relationship with the subject's pain. The lack of patient-specific intra-subject studies investigating the relationship between PFP and the underlying mechanisms warrants such a study.

Another motivation is to create computational tools which can be used by other researchers, and for further studies within the research community. Automated processing techniques that are modifiable, and can be adapted to specific studies allows for future researchers to potentially "plug and play" similar input data. To answer clinical questions about physiological changes observed in the results, it is necessary to understand the limitations of the modelling tools, and understand the extent to which experimental and modelling errors contribute to results. Therefore, in addition to setting up automated pipelines, investigations of the processing techniques and methods provide the research community with guidance on how to process biomechanical data for similar kinds of analysis.

This project is a continuation of a previous masters project (de Jongh, 2015). A number of challenges were faced during the de Jongh (2015) study. These included a shortage of force plates, changes in the testing facility and changes in the motion capture techniques. Due to these problems, the previous project was unable to compare pre- and post-intervention results to determine if there is a correlation between the patellofemoral biomechanics and the pain experienced by a subject.

The continuation of this project is motivated by the proposed improvements for future work described in the previous project. The most notable improvement is the inclusion of two additional force plates in the testing facility which allows for a complete force balance to be performed between the subject and the ground, this is discussed further in the Apparatus section of the Experimental procedure.

1.3. Objectives

This project forms part of a broader longitudinal study in which the aim is to assess the effect of a subject tailored physiotherapeutic intervention on patellofemoral risk factors and clinical outcomes in subjects that experience anterior knee pain. The study uses each participant as his/her control, eliminating inter-subject variability. The scope of this project within the more extensive study is to perform computational modelling using the data from the subject testing to ultimately determine patellofemoral joint loads.

In addition to providing computational modelling results, this project aims to create an automated pipeline, so that future data or modified data can be applied to the same pipeline without extensive user intervention. This pipeline minimises the requirements for user intervention along the processing pipeline. In line with creating an automated pipeline, another aim is to investigate the signal processing techniques recommended by industry and to improve these techniques in the context of their requirements for the next step in the pipeline. The aim is to use computational modelling to compare pre- and post-intervention biomechanics and determine if there is a correlation between specific risk factors, treatment and pain. To achieve the desired aims of this project, the following objectives have been identified:

- Measure joint geometry, kinematic and kinetic drivers of the musculoskeletal model during over-ground gait.
- Develop an automated modelling pipeline in OpenSim (Simtk-confluence.stanford.edu, 2017) to determine kinematics, joint moments, joint moment arms and muscle lengths.
- Extend the modelling pipeline to apply the OpenSim results to the Calibrated EMG informed Neuromusculoskeletal Software to estimate muscle forces.
- Extract electromyography (EMG) results, and determine appropriate filtering to use in muscle force prediction.

1.4. Thesis outline

- Chapter Two: A literature study is performed, describing human gait, the anatomy of the human lower extremity with a focus on the knee and the patellofemoral joint which is the joint of interest for this project. A description of biomechanical data relevant to this project is described regarding its use and limitations as described in the literature.
- Chapter Three: The experimental procedure that allowed for the collection of data analysed in this project is described. The hardware and software used in data acquisition are described, as well as some internal lab procedures. The participant requirements are listed as well as the subject details of the participating subjects. Finally, a summary of the information received from the lab is given.
- Chapter Four: The pre-processing procedure is described step by step. The technique by which data are processed and partitioned is described.
- Chapter Five: The detailed description of the OpenSim pipeline is given. This includes the theory of each step, as well as the context of each step within the overall modelling pipeline, the results of each step and comparisons and discussion of inter-step results, as well as dynamics results due to different processing techniques.
- Chapter Six: The method used to calculate muscle forces is described. The theory, as well as the implementation, is given, with a comparison and discussion of results based on different EMG processing techniques, and a final results section with the full pipeline that was ultimately implemented.
- Chapter Seven: The report is concluded concerning the achievement of the objectives laid out for the project. The potential for future work and the contribution of this project to the field of computational biomechanics is outlined.

2. Literature Review

2.1. The lower limb

Humans are unique in that they are bipedal. The human lower limb is adapted for the locomotion, weight bearing and erect posture associated with upright bipedal beings (Palastanga *et al.*, 2002). Within this section, the physiology and anatomy of the three main lower limb joints – the hip, knee, and ankle joint – will be discussed as per Palastanga, *et al.*, 2002. Anatomical definitions are also explained as well as the human gait, to understand the context in which the lower limb joints function.

2.1.1. Anatomical definitions

Figure 1 below contains anatomical reference planes and rotations, which are repeatedly used throughout this text.

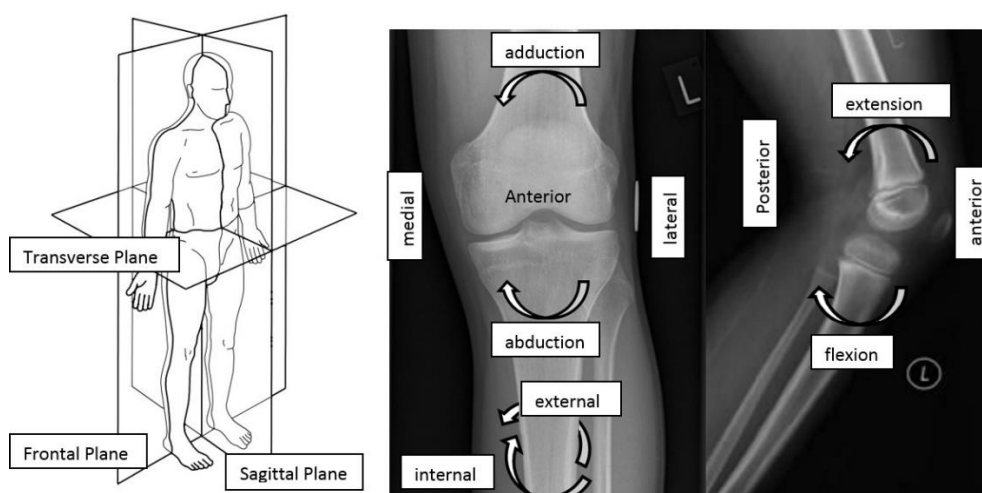


Figure 1: Anatomical planes and rotations (adapted from Samuelparsons.co.uk, 2017)

2.1.2. Human Gait

Bipedal walking has two conditions: periodic movement of each foot from one position of support to the next and sufficient ground reaction forces (GRF) to support the body. Periodic movement is the fundamental characteristic of human gait. Normal human gait describes a regular cyclic action against which a patient's gait can be compared. Most movement during human gait occurs in the sagittal plane. However, the frontal and transverse planes should not be ignored (Vaughan *et al.*, 1999).

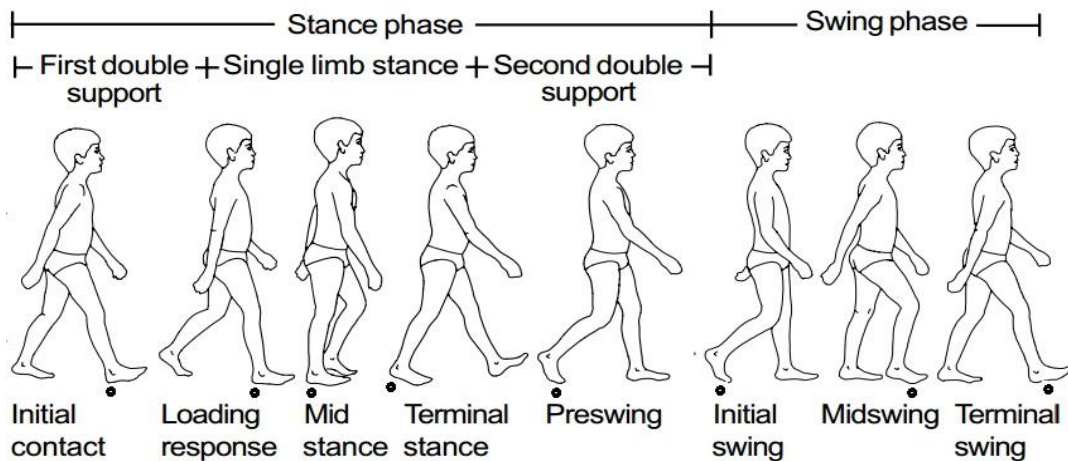


Figure 2: Human gait cycle (adapted from Vaughan *et al.*, 1999)

Figure 2 above shows the phases and sub-phases of human gait. The two main phases of human gait are the stance phase (occurs over 60% of the cycle) and the swing phase (occurs over 40% of the cycle). The stance phase (1-5) and swing phase (6-8) events as described in Vaughan *et al.*, 1999 are as follows:

1. Heel strike/Initial contact: Point at which the body's centre of gravity is at its lowest point (0%).
2. Foot-flat/Loading response: The plantar surface of the foot makes contact with the ground (0-10%).
3. Midstance: The swinging foot passes the stance foot, and the centre of gravity is at its high point (10-30%).
4. Heel-off/terminal stance: The heel loses contact with the ground and push-off is initiated (30-50%).
5. Toe-off/Pre-swing: Terminates the stance phase as the foot leaves the ground (50-60%).
6. Acceleration/Initial swing: The beginning of the swing phase, begins as soon as the foot leaves the ground and the hip flexor muscles are activated to move the foot forward (60-70%).
7. Midswing: Occurs when the foot passes directly beneath the body (70-85%).
8. Deceleration: Muscle action works to slow the leg and stabilise the foot in preparation for the next heel strike (85-100%).

2.1.3. The hip joint

The hip joint is the connection between the lower limb and the trunk. It is a synovial ball and socket joint, as shown in Figure 3. The femoral head articulates with the acetabulum in the pelvic bone. This deep socket allows a wide range of motions as well as transmission of large forces relating to a person's full body weight during a range of activities such as running, walking and stair ambulation. The hip moves in all three anatomical planes: flexion/extension in the sagittal plane, abduction/adduction in the frontal plane and internal/external rotation in the transverse plane (Logan, 2005).

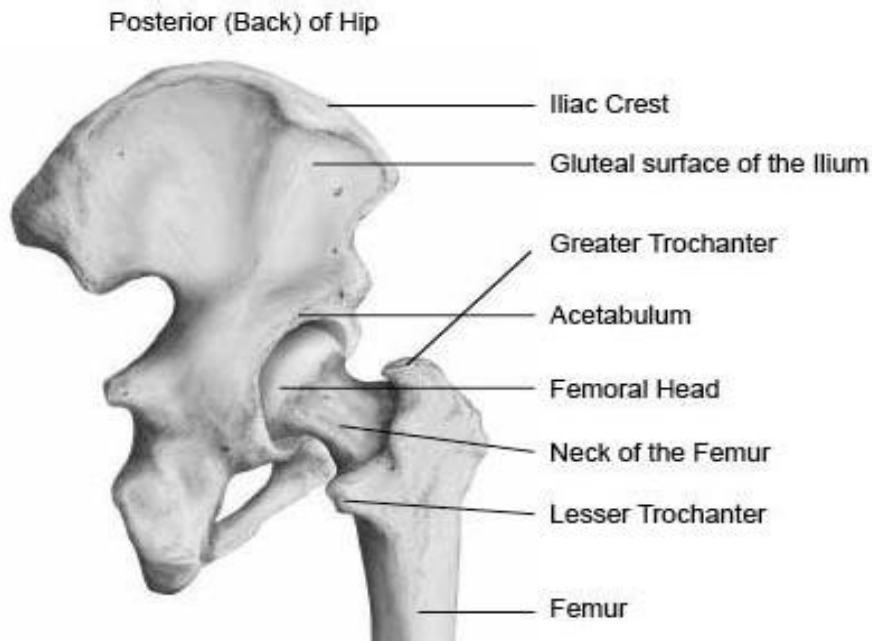


Figure 3: The hip joint (adapted from Schmidler, 2017)

To facilitate and control the movements of the hip a significant amount of strength and stability are required. The capsular ligaments are crucial in limiting and controlling all of the movements of the hip. The capsular ligaments are the iliofemoral, pubofemoral and ischiofemoral ligaments which are relaxed under flexion and taut under extension. The hip joint requires the following muscles, seen in Table 1 below to strengthen it and produce the necessary movement:

Table 1: Muscles responsible for movement in the hip

Movement	Muscle
Flexion	Psoas major, iliacus, pectineus, rectus femoris and Sartorius
Extension	Gluteus maximus and hamstrings (semitendinosus, semimembranosus and bicep femoris)
Abduction	Gluteus maximus, medius and minimus, and tensor fascia lata
Adduction	Adductor magnus, logus and brevis, gracilis, and pectineus
Internal rotation	Gluteus medius and minimus, tensor fascia lata, psoas major, and iliacus
External rotation	Gluteus maximum, piriformis, obturator internus, gemellus superior and inferior, quadrates femoris and obturator

2.1.4. The knee joint

Figure 4 below shows the functional anatomy of the knee joint. The knee is one of the most complex joints in the body. It is a synovial bicondylar hinge joint with three separate articulations, namely: the patellofemoral joint (patella and anterior distal femur), the tibiofemoral joint (proximal tibia and distal femur) and the fibulotibial joint (fibula and proximal tibia) (Palastanga *et al.*, 2002; TeachMeAnatomy, 2016).

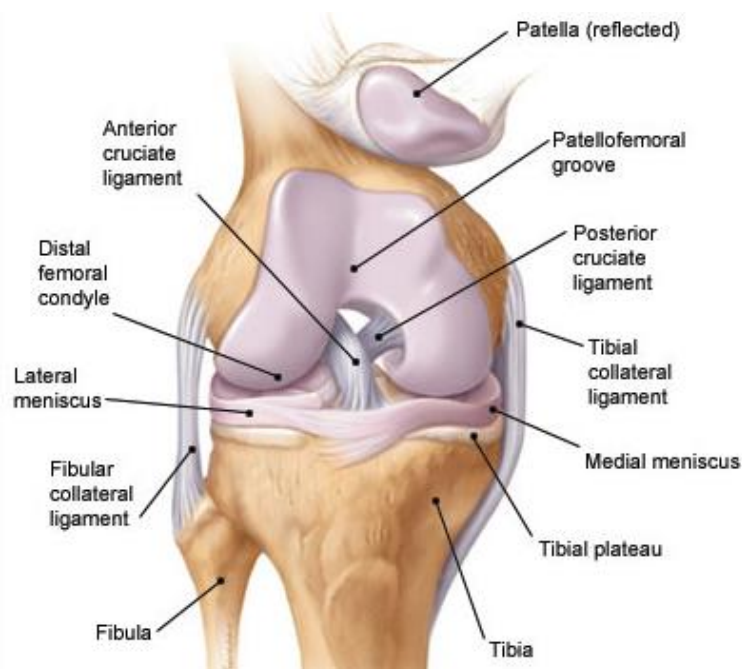


Figure 4: The knee joint (adapted from Schmidler, 2017)

The knee joint is functionally a hinge joint with flexion and extension in the sagittal plane however it does allow for abduction/adduction and a small degree of rotation, mostly when the knee is flexed, and the foot is on the floor. There is usually an inverse relationship between stability and mobility in joints. However, the knee is an exception with both functions being made possible by interactions between ligaments and muscles and complex articulations within the joint. The high level of mobility comes at a cost, due to the relatively weak interlocking in the knee joint, it is susceptible to strains and dislocations (Palastanga *et al.*, 2002).

The knee plays a critical role in locomotion. It acts with the ankle to be the forward propeller of the body. To support the full weight of a body and perform its essential function, the knee has a number of favourable characteristics: the surfaces of the tibia and femur are expanded to support the load; it has strong collateral and intracapsular ligaments; finally, it is reinforced by the aponeurosis and tendons. The muscles responsible for movement in the knee are described in Table 2 below.

Table 2: Muscles responsible for movement in the knee

Movement	Muscle
Flexion	Hamstring (semitendinosus, semimembranosus and bicep femoris), gastrocnemius, gracilis, Sartorius, and popliteus
Extension	Quadriceps femoris (rectus femoris, vastus lateralis, vastus medialis and vastus intermedius) and tensor fascia lata
Lateral rotation	Bicep femoris
Medial rotation	Semitendinosus, semimembranosus, gracilis, Sartorius and popliteus

2.1.5. The ankle joint

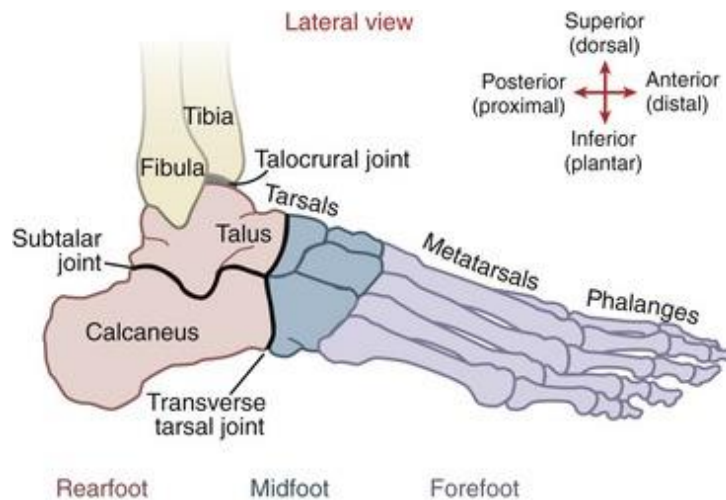


Figure 5: The ankle joint (Clinical Gate, 2017)

Figure 5 above shows the functional anatomy of the ankle joint. The ankle joint is a synovial hinge joint with the only movement in the sagittal plane, plantarflexion (flexion) and dorsiflexion (extension). The ankle adjusts the line of gravity, seesawing backwards and forwards, to keep it within the limits of the supporting surface. The ankle acts with the subtalar and metatarsal joints, supported by the axial rotation of the knee to provide a three degree of freedom movement that provides stability and mobility (Palastanga *et al.*, 2002). Table 3 shows the muscles used in plantarflexion and dorsiflexion of the ankle joint.

Table 3: Muscles responsible for ankle movement

Movement	Muscle
Planterflexion	Gastrocnemius (medial and lateral), soleus, plantaris, flexor longus, peroneus longus
Dorsiflexion	Tibialis anterior, extensor hallucis, extensor longus

The axis of the ankle joint is not parallel to the axis of the knee. It is set obliquely 20-25° to the frontal plane due to the outward rotation of the lower end of the tibia. Due to the obliquity of the ankle joint, compensation is necessary to allow for simultaneous movement of both the knee and ankle joints in the transverse plane. The subtalar joint provides this compensation. Articulation occurs between the distal ends of the tibia and fibula proximally and the body of the talus distally. The trochlea surfaces of the tibia and talus are the weight-bearing surfaces. The medial and lateral malleoli grip the body of the talus and act as the stabilising surfaces (Palastanga *et al.*, 2002).

2.2. Biomechanical Information

2.2.1. Electromyography

Electromyography (EMG) is the measurement of electrical signals transmitted by motor neurons that cause muscles to contract (Basmajian *et al.*, 1985). These signals can be measured non-invasively and indirectly reflect the neural drive to muscles (Sartori *et al.*, 2016). To understand these bioelectric signals, it is essential to understand the underlying muscle physiology. In this case, it is of particular importance to understand the “inverse problem”, that is, how do EMG signals represent muscle mechanics and guide the identification and description of these mechanics (Merletti *et al.* 2004).

A motor unit (MU) consists of a α -motoneuron which stems from the spinal cord, and the muscle fibres that the motoneuron innervates, as shown in Figure 6. Direct cortical control of the muscle activity is provided by the link between the corticospinal tract and the α -motoneuron (Merletti *et al.*, 2004). The firing pattern of the MU is determined by the net membrane current induced by the synaptic innervation sites. The number of MUs present in a muscle differs significantly across different muscles, as well as the force generating a capacity of these MUs. Motor units have therefore been categorised into three different categories based on chemical and contractile characteristics (Merletti *et al.*, 2004). Fast-twitch, fatigable muscles; fast-twitch, fatigue-resistant muscles and slow-twitch fatigue-resistant muscles.

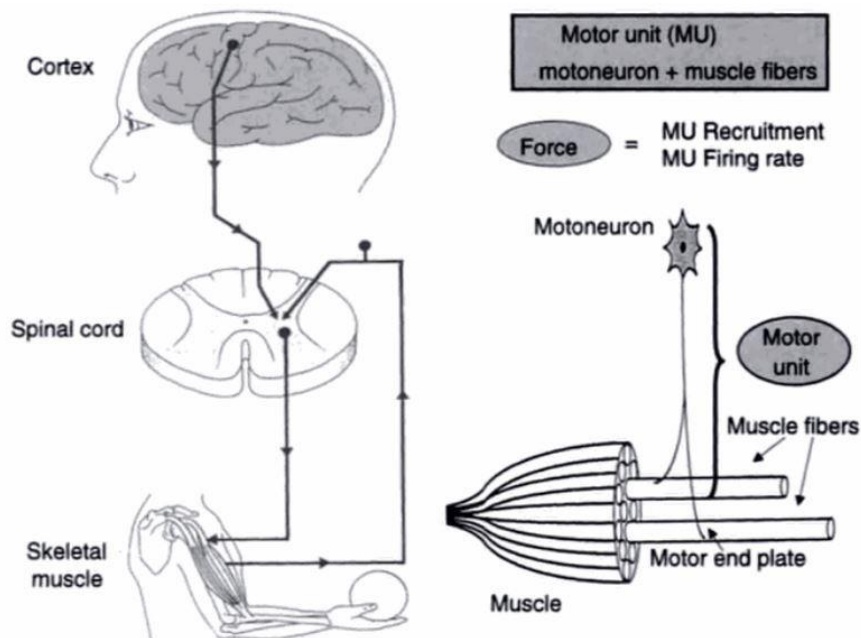


Figure 6: The underlying motor control mechanisms, motor units and their components (Merletti *et al.*, 2004)

Muscle strength is increased by the central nervous system recruiting more active motor units (spatially) and by increasing the firing rate (Emedicine.medscape.com, 2017). Surface EMG detects the motor unit's spatial and temporal interference pattern at the location of detection. The nature of motor unit activation produces a measured signal that is a zero-mean stochastic process where the standard deviation is proportional to the number of active motor units and the rate at which those units are activated (Clancy *et al.*, 2002).

Clancy *et al.* (2002) group EMG analysis into three major stages: electrode selection and placement; processing of the acquired EMG; and interpretation and further modelling derived from the estimated EMG. The first stage was determined by the physiotherapist who formed part of the primary project, while this study is interested in the second and third stage. The second stage is of particular importance because of the sensitivity of the results based on processing techniques, and the subsequent effects of the changes in results on the results of later modelling techniques forming part of stage three.

To extract the relevant information from the EMG signals, it is essential to understand the sources of noise that infiltrate the signal. Understanding the frequencies of these sources allows for the removal, or reduction of the noise during processing. Surface EMG, used in this project, is sensitive to electrode noise. The electrode-skin interface has a reactive impedance, dependant on the electrode size, the signal frequency and the current density at the electrodes (Clancy *et al.*, 2002). A high impedance can cause reduced signal amplitude and distortion but can be reduced by using a signal amplifier with an input impedance at least 100 times higher than the expected electrode impedance. Careful skin preparation during electrode placement helps reduce the electrode impedance to acceptable levels (Clancy *et al.*, 2002).

Motion artefacts are introduced into the EMG signal via relative motion between the electrode and the skin, and via a change in the inherent potential difference of the skin due to skin deformation and stretching (Webster, 1984). The first kind of motion artefact can again be reduced by careful electrode placement, ensuring that the separation between the electrode and the skin is minimised. Motion artefacts are also removed from the resultant signal through conditioning, with the power density of the motion artefact mostly below 20 Hz (Clancy *et al.*, 2002). Cable motion artefacts are introduced if unshielded cables move through ambient magnetic or electric fields. Shielded cables provide a solution but are also susceptible to artefacts caused by friction and deformation of the cable generating static charges which are picked up by the measurement system (Klijn and Kloprogge, 1974).

Power line interference is introduced by ambient electromagnetic fields in the vicinity of Alternating Current (AC) power lines. The frequency of these fields is

50 Hz in South Africa. The magnitude of this noise can be reduced by shielding the recording equipment and by careful cable handling (Clancy *et al.*, 2002). This signal can also be treated in signal conditioning. Other sources of noise include inherent noise within the electronic instrumentation, with a low amplitude but a broad band of frequency. This is not a critical concern because there is a high signal to noise ratio. Other biosignals might also infiltrate the EMG signal (Redfern, Hughes and Chaffin, 1993). In particular electrocardiographic (ECG) signals, however, this is less problematic when the electrode sites are in the lower limbs, as with this project. Literature specific to EMG signal processing is further discussed in EMG processing.

2.2.2. Kinematics and kinetics

In biomechanics, kinematics refers to the study of human motion without the inclusion of the resultant forces. Kinetics is the study of motion taking into account the resultant forces and torques (Knudson, 2012). The recording of kinematic and kinetic data is made possible by the use of motion capture (mocap) cameras and force plates respectively. These tools used in conjunction make it possible to determine joint powers and moments in three dimensions.

Mocap in gait analysis is the process of recording the movement of limb segments and the joints that connect them (VICON, 2017). The most widely used system and the system used in this study is an optical-passive system. A passive optical system uses infrared cameras to track retroreflective markers (Kirk *et al.*, 2005). An infra-red-light source from the camera illuminates the markers in the cameras field of view, and dim the surrounds allowing a two-dimensional image from the camera to be recorded (Whittle, 1996). The use of multiple cameras allows for the combination of two-dimensional marker positions to be used to stereometrically calculate the position of each marker in three-dimensional space for the duration of a specified activity within the cameras capture volume (Davis *et al.*, 1991).

The reliability of kinematic data depends on a number of factors. These include but are not limited to soft tissue artefacts (Leardini *et al.*, 2005), physiological variability between human subjects, and variation in marker placement (Kadaba *et al.* 1989). Marker placement has been identified as a wide-ranging source of error in gait analysis. In identifying lower extremity landmarks Della Croce *et al.*, (2005) reported intra-observer variability ranging between 5 and 21 mm, and inter-observer variability between 12 and 25 mm. It is therefore vital that the individual placing markers during a study is trained, and that the same individual places the markers for every subject during the experimental testing. Soft tissue artefacts arise due to relative motion between markers placed on a subject, and the underlying bony segment of interest (Lucchetti *et al.*, 1998). These artefacts exist within the same frequency range as high-frequency components of motion, so care needs to be taken when dealing with kinematic data and analysing results.

Once the kinematic data has been captured it can be used to calculate the angle of the primary joints in three-dimensions, and how those joint angles change during the gait cycle (Whittle, 1996). In human movement analysis, the body segments are modelled as rigid bodies. In order to determine joint angles, the position of the rigid segment needs to be constructed in space for each time frame sampled by the camera system. Two pieces of information are necessary for this reconstruction: one relative to morphology and one relative to movement (Capozzo *et al.*, 2005). A local frame associated with a bony segment can be reconstructed using the instantaneous position of at least three non-collinear markers, as shown in Figure 7 (a). These frames can then be used to describe the stationary or time-varying location of a segment in a global frame. Joint kinematics is then the relative movement between two segments, given the position and orientations of the local frames of each segment relative to the global frame (Capozzo *et al.*, 2005).

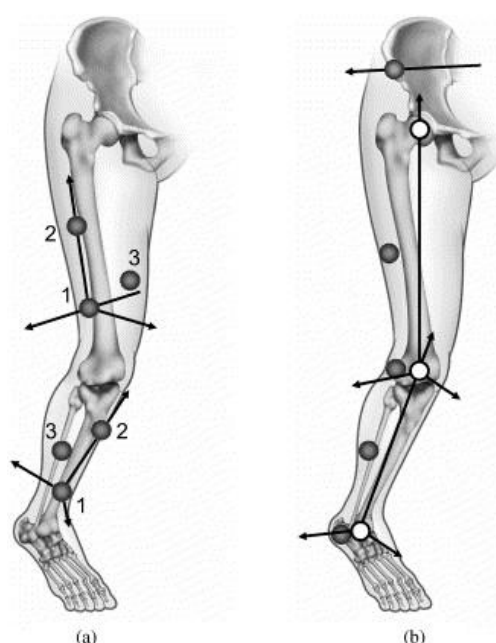


Figure 7: Marker set frames and joint centre frames (Capozzo *et al.*, 2005)

The kinetics of a subject is informed by ground reaction forces, measured by force plates on the ground. The output of the force plates is an electrical signal which can be used to produce the three components of force (vertical, lateral and fore-aft, as seen in Figure 8), the two coordinates of the centre of pressure and the moment about the vertical axis (Whittle, 2007).

The GRF data in isolation is not of great value. However, when combined with the kinematic data and human data, it can be used to perform a mechanical analysis of gait (Whittle, 1996). The human data refers to knowledge of the relative mass, moments of inertia and centres of gravity of limb segments (Clauser *et al.*, 1969). The combination of the kinematic and kinetic data are used to calculate joint angles,

joint moments, musculotendon lengths and moment arms. GRF describe the total force applied by the foot on the ground in the transverse, frontal and sagittal plane, as shown in Figure 8. Further literature, investigations and discussions on the processing of kinematic and kinetic data take place in Force plate and motion data filtering.

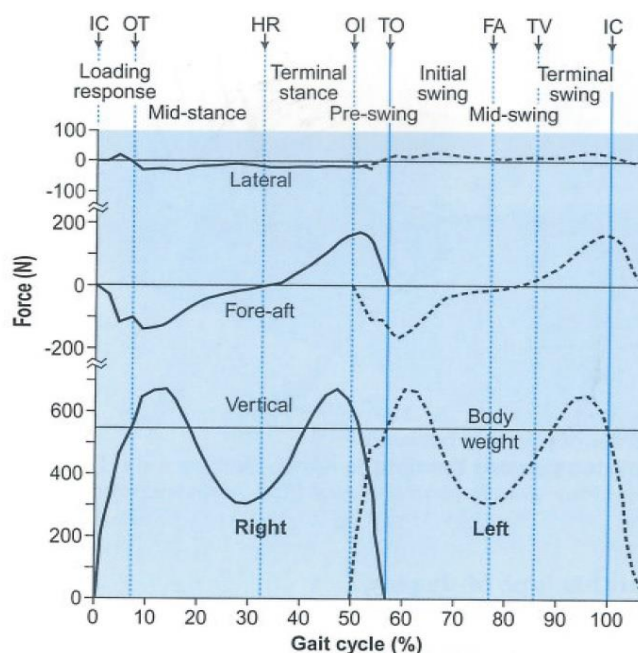


Figure 8: Components of ground reaction forces (adapted from Whittle, 2007)

2.3. The OpenSim model

The model provided by OpenSim, the Gait2392 model, is a three-dimensional 23 degree-of-freedom (DOF) model of the human musculoskeletal system. The model combines lower extremity joint descriptions defined by Delp *et al.* (1990), lower back joint and anthropometry adopted by Anderson and Pandy (1999) and a modified planar knee model created by Yamaguchi and Zajac (1989). The Gait2392 model contains 76 muscles actuated by 92 musculotendon units (MTU) in the lower limbs and torso.

2.3.1. Joint geometry

The lower extremity is made up of seven rigid body segments: pelvis, femur, patella, tibia/fibula, talus, foot and toes. Each segment has its fixed reference frame as shown in Figure 9. The relative motion of these segments defines the knee, hip, ankle, subtalar and metatarsophalangeal joints.

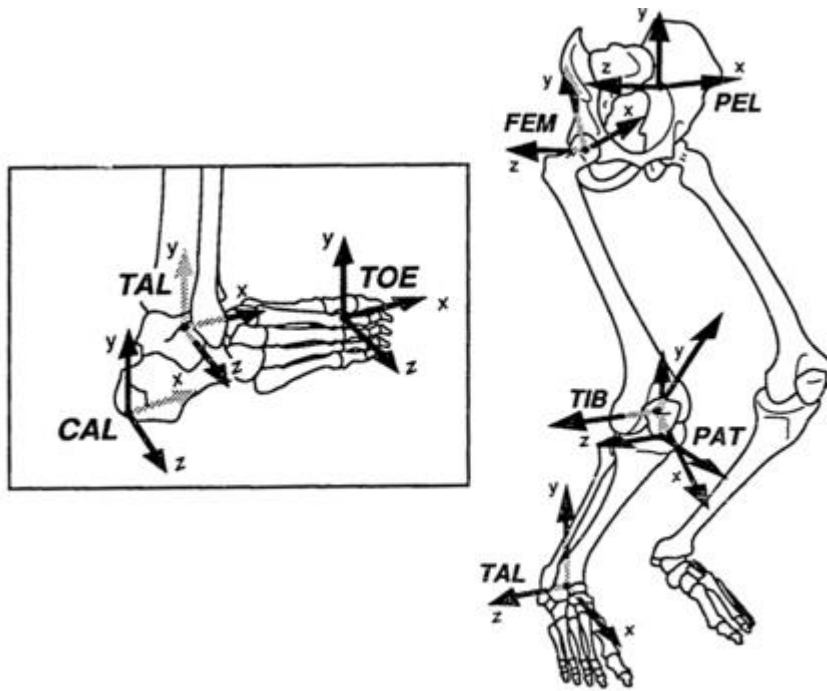


Figure 9: Location of the reference frames within rigid segments (Delp *et al.*, 1990)

The pelvic frame, seen in Figure 9, is defined as the midway point between the left and right anterior superior iliac spine (ASIS). OpenSim defined the neutral position as the pelvic frame aligned with the ground frame. This differs from what has been found in a clinical setting where neutral pelvic tilt is subject specific and is often closer to 10 degrees (Lembeck *et al.*, 2005). This may cause differences when comparing pelvic tilt results to literature.

The hip joint is modelled as a ball and socket joint. Three orthogonal axes are fixed in the femoral head about which the femoral reference frame rotates defining the transformation between the hip and the femur. The knee joint is a more complicated joint model because of its multi-bone and ligament structure. In order to reduce the computational cost of determining the extensor moment arm of the knee Yamaguchi *et al.* (1989) created a simplified knee model.

The simplified model is a single DOF model which accounts for the kinematics of both the patellofemoral joint and the tibiofemoral joint in the sagittal plane without losing the patella levering mechanism. This planar knee model was adopted by Delp *et al.* (1990) and modified by defining the transformation between the femoral, tibial and patella reference frames as functions of the knee angle. The model with the femoral condyles represented as ellipses, and the tibial plateau as a line segment is shown in Figure 10. The contact point of the tibiofemoral joint depends on the knee angle and as specified according to data reported by Nisell *et al.* (1986).

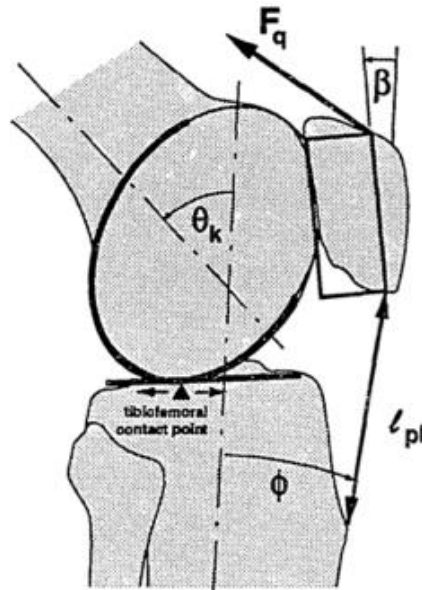


Figure 10: Sagittal plane knee model created by Delp *et al.* (1990)

The knee model ultimately adopted in OpenSim is a further adaptation of the model created by Delp *et al.* (1990). In the OpenSim version, the patella has been removed to avoid kinematic constraints. The insertions of the quadriceps on the tibia have been modelled as moving points within the tibial reference frame. The ankle, subtalar and metatarsophalangeal joints (seen in Figure 5) have been modelled as frictionless revolute joints.

The orientation and location of the axes for the joints are modified versions of the joints described by Inman (1976). The modification in the OpenSim model is an 8-degree rotation of the vertical axis of the metatarsophalangeal (MTP) joint. This is done to reduce disarticulation of the joint. This problem does not typically occur in the ankle and subtalar joints, so they are left as described by Inman (1976).

2.3.2. Muscle geometry

Anatomical landmarks on the bone models are used to define the lines of action for the muscle-tendon actuators. A series of line segments represents each muscle-tendon path. For muscles in which wrapping occurs, or are constrained by retinacula, intermediate via points are used to represent the muscle path more accurately. Other muscles can be sufficiently defined by origin and insertion landmarks only. The number of via points activated depends on the body position.

3. Experimental procedure

Experimental procedure describes and discusses the experimental setup and procedures followed in the primary study of which this project forms a part. The experiments took place at the Central Analytical Facilities (CAF) Motion Laboratory at Stellenbosch University's Tygerberg Medical Campus. Before the data was packaged in the Coordinate three-dimensional (C3D) format, the experimental data obtained during the testing underwent some pre-processing in the motion laboratory.

Ethical approval for this study, and the primary study for which this forms part of has been obtained from the Committee on Human Research at the Health Research Council of Stellenbosch University (Ref: N13/05/078).

3.1. Apparatus

3.1.1. EMG measurements

Electrical signals transmitted by motor neurons cause muscle contractions. EMG is an electronic diagnostic tool that translates these signals into data that can be interpreted by a specialist (Mayo Clinic, 2015). A telemyo, Noraxon-10-channel, wireless EMG system (Noraxon USA, 2017) is used to capture muscle activation data. Surface electrodes are attached at predetermined muscle points and connected to the telemyo sensors, which wirelessly links to the relevant software on a computer. Electrodes are placed on the muscles as described in Table 4 and shown in Figure 11:

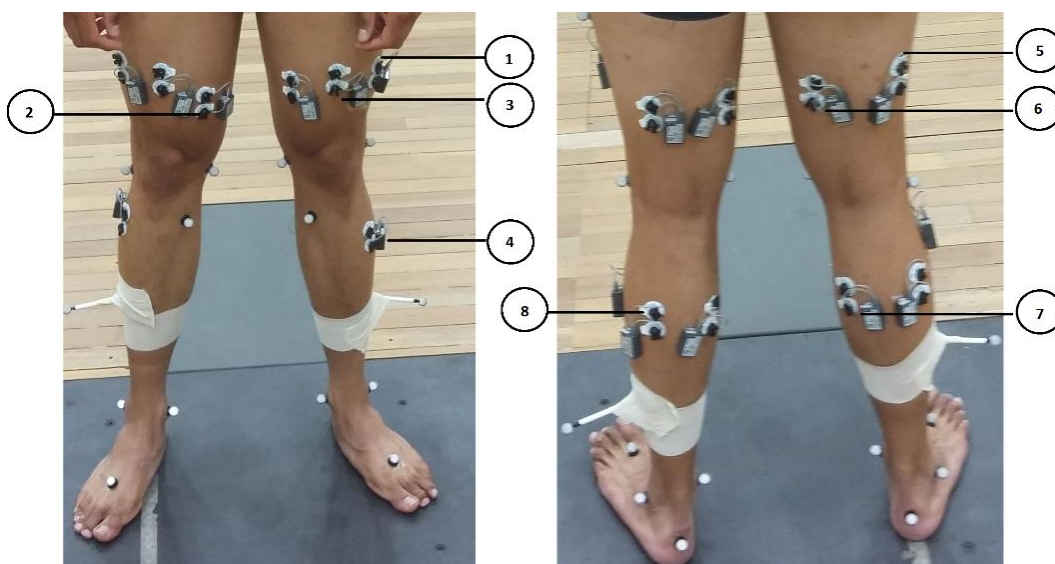


Figure 11: EMG designation

Table 4: EMG electrode positions

EMG Position	Muscle (Placed on the right and left limb)
1) Electrode placed at 2/3 on the line from the anterior spina iliaca superior to the lateral side of the patella.	Vastus Lateralis (VL)
2) Electrode placed at 80% on the line between the anterior spina iliaca superior and the joint space in front of the anterior border of the medial ligament.	Vastus Medialis (VM)
3) Electrode placed at 50% on the line from the anterior spina iliaca superior to the superior part of the patella.	Rectus Femoris (RF)
4) Electrode placed at 1/3 on the line between the tip of the fibula and the tip of the medial malleolus.	Tibialis Anterior (TA)
5) Electrode placed at 50% on the line between the ischial tuberosity and the lateral epicondyle of the tibia.	Biceps Femoris (BF)
6) Electrode placed at 50% on the line between the ischial tuberosity and the medial epicondyle of the tibia.	Semitendinosus (ST)
7) Electrode placed on the most prominent bulge of the muscle.	Medial Gastrocnemius (MG)
8) Electrode placed at 1/3 of the line between the head of the fibula and the heel.	Lateral Gastrocnemius (LG)

To compare muscle activities, it is necessary to normalise the EMG signals. The normalisation tests consist of 10 second maximum voluntary isometric contractions (MVC) of each muscle group listed in Table 4 above. Normalisation reference values can also be extracted from the walking trials. These are known as walking trial maximums (WTM) and are discussed further in EMG processing. Data from the quadriceps, medial and lateral hamstrings, tibialis anterior and medial and lateral gastrocnemius is then captured during testing, indicating when the muscle is activated and to what extent.

3.1.2. Motion capturing

Motion capture is the process of recording the movement of objects or people. This study uses optical passive mocap, which uses retroreflective markers that are tracked by infrared cameras (Vicon Motion Systems, n.d.). The motion analysis is performed using a Vicon Motion Analysis (Ltd) (Oxford, UK) system with Nexus software (© Vicon Motion Systems Ltd., Oxford UK). The reflective markers are

attached to the subject's body by a trained physiotherapist at predetermined landmarks shown in Figure 12 and described in Table 5 below. The cameras capture the position of the markers in three-dimensional space captured at 200 Hz.

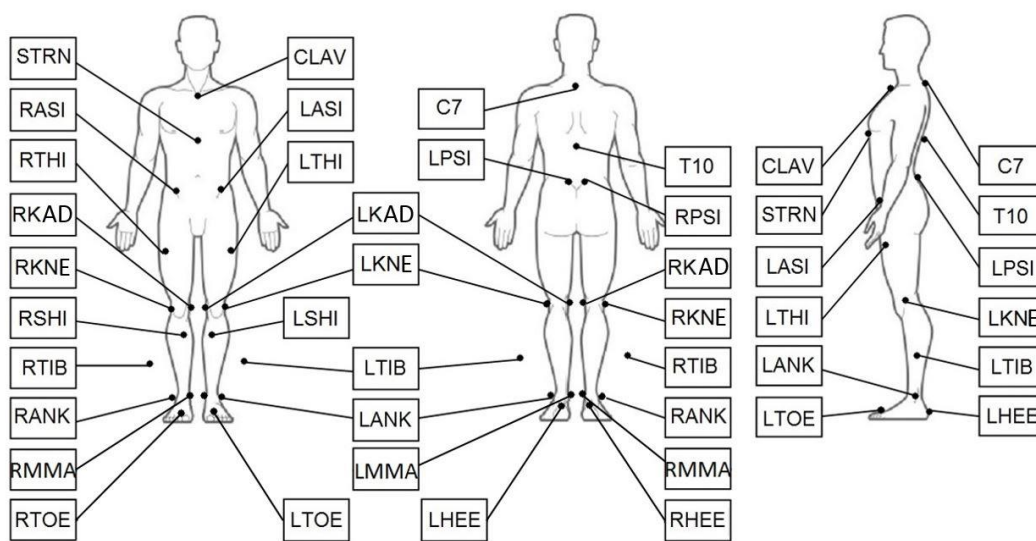


Figure 12: Marker positions for mocap

Table 5: Marker position designation

Marker Position	Marker Designation
7 th Cervical Vertebrae	C7
10 th Thoracic Vertebrae	T10
Clavicle	CLAV
Sternum	STRN
Superior anterior iliac spine	RASI – LASI
Posterior superior iliac spine	LPSI – RPSI
Thigh	RTHI – LTHI
Medial knee	RKAD – LKAD
Lateral knee	RKNE – LKNE
Shin	RSHI – LSHI
Tibial wand marker	RTIB – LTIB
Lateral Ankle	RANK – LANK
Medial Ankle	RMMA – LMMA
Toe	RTOE – LTOE
Heel	RHEE – LHEE

3.1.3. Ground reaction force measurement

The motion laboratory, part of the central analytics facility, at Tygerberg medical campus has three force plates. One large Bertec FP9060-15 force plate and two smaller Bertec FP6040-PT force plates on either side of the larger one. The large force plate is glued in and secured to the foundations, while the two smaller plates are not. These three force plates are used to measure ground reaction forces between the subject and the floor. The force plates measure the ground reaction forces at a frequency of either 1000Hz, 1500Hz or 3000Hz. This frequency is included in the input file received from the lab.

This project aims to determine loads at the knee joint. To determine these loads the contact force and kinematics need to be determined during the duration of the impact on the force plate, and specifically during the stance phase. However, the forces applied to the foot not striking the force plate are also necessary to perform a successful gait analysis. The three force plates are necessary because a full force balance on the subject is required during the full gait cycle, and this is only possible if all of the contact forces are known. Therefore, it is fundamental that both feet land on separate force plates during the walking test.

The force plates record three-dimensional ground reaction forces between the subject and the ground as well as the centre of pressure (COP) and the resulting moment on the force plate in a global coordinate system. The use of three force plates is new to this project. The previous project by de Jongh (2015) used only one force plate. The addition of the force plates eliminates the need to superimpose forces applied to the foot not striking the force plate. The layout of the three force plates is shown in Figure 13.

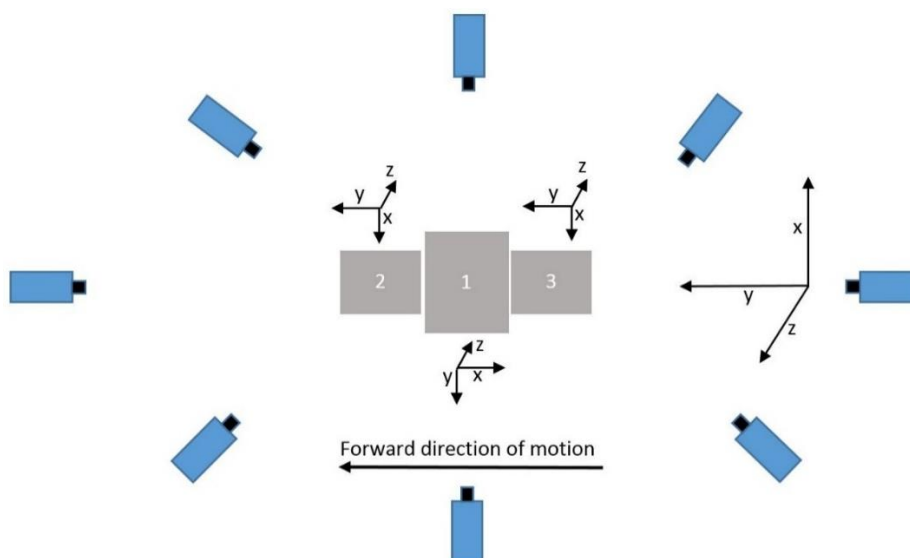


Figure 13: Laboratory layout and reference frames

Figure 13 shows the coordinate system of each force plate, as well as the global coordinate system of the laboratory. The marker positions are recorded in the global coordinate system, and the force plate forces are recorded in their respective coordinate systems. The positive direction of motion is described as the global positive y-direction. To analyse the data the local coordinate systems need to be rotated to correspond to the global coordinate system. The force plate rotation is discussed further in Acquisition.

3.2. Subjects

The research participants treated in this study were required to meet specific requirements to be eligible to take part in the study. The subjects comprised of males and females between the ages of 14 and 40 as this is the range in which anterior knee pain is most commonly experienced (while eliminating osteoarthritis). An initial screening questionnaire was filled in by the participants to determine whether they experienced symptoms of patellofemoral knee pain during at least two of the following activities: prolonged sitting, stair ascent and descent, squatting, running, kneeling, lunging and jumping. After completing the initial questionnaire, participants are then assessed by an experienced physiotherapist and included if they meet the following criteria:

- Experience anterior knee pain
- Have had no previous surgery involving the lower extremity of the symptomatic limb.
- Have no history of patella dislocation or subluxation.
- Have had no previous traumatic injuries to the menisci, cruciate or collateral ligaments in either leg
- Do not require foot orthosis for pes plantus (flat-footed) or cavus (high instep).
- Have no possible underlying degeneration and instability of the knee joint.
- Have not received any conservative treatment from the onset of pain, including physiotherapy, non-steroidal anti-inflammatory drugs or corticosteroids.
- Have not had any previous traumatic injuries to the menisci, cruciate or collateral ligaments in either limb.

- Have no signs of inflammation.

For the primary study, a total of 31 subjects with anterior knee pain were tested and treated, with the data obtained used in this project. The overall procedure that the subjects went through was as follows: screening questionnaire and clinical assessment, the experimental procedure pre-intervention during the initial testing at the CAFs motion lab. After which an MRI was taken of the affected limb(s). The subject then underwent eight weeks of physiotherapeutic intervention and monitoring. Finally, a full experimental procedure was performed after the full intervention was completed. The EMG, GRF and motion analysis is performed with the same procedure as the initial test. The experimental procedure is described below.

The subjects were treated based on their priority kinematic risk factor. These risk factors occurred on either leg or bilaterally. The occurrence of the risk factor on a particular leg did not necessarily correlate to the leg which experienced pain. The risk factors were defined as follows:

- a) Decreased left, right or bilateral knee flexion in stance
- b) Increased left, right or bilateral peak hip adduction
- c) Decreased left, right or bilateral peak hip internal rotation
- d) Increased left, right or bilateral knee extension throughout the gait cycle

Table 6 contains the description of the subjects that are analysed and discussed in this report. The priority risk factors in the third column are referenced from the list above.

Table 6: Subject details

Subject	Affected side	Priority kinematic factor
AKP03	Left	a - Bilateral
AKP16	Right	a - Bilateral
AKP17	Right	c - Right
AKP29	Left	b - Bilateral
AKP30	Left	c - Left

After the subjects have had the markers and EMGs applied as prescribed above, they can perform the walking and static trials. The static trial involves the subjects standing on force plate one with their arms extended to ensure visibility of all the markers. The purpose of the static trial is to scale the musculoskeletal model. The walking trial involves the subject walking across the laboratory, with their feet

successively hitting each force plate. There can be no overlap in foot strike between the force plates. A walking trial is successful if the subject walks across all three force plates, with no overlap and no software or hardware malfunction. Once the subject has performed three successful trials on each leg, the trials are completed. The subject also undergoes maximum voluntary contraction trials. These MVC trials are performed with a trained physiotherapist with the aim of achieving maximum muscle excitation against the resistance of the physiotherapist. This procedure is performed for each muscle group on which EMGs have been placed.

3.3. Laboratory output

Ultimately the laboratory outputs the data in C3D format. This format is used widely in the biomechanics field and is designed for the storage of a wide variety of data and their associated parameters (C3d.org, 2017). Some laboratory processing and quality controls are performed before the data are placed in the C3D files. This processing included event detection of foot strike and foot off using a 20 N threshold on the force plate value, and heel marker trajectories used to assign the events to the correct foot. A C3D file is created for each trial, including the static trial and the maximum voluntary contraction trials. Each walking trial C3D file contains the following data:

- Raw labelled marker position frames
- Raw labelled EMG data
- Raw labelled force plate data containing ground reaction forces
- Force platform information including type, origin and corner positions
- Frame rated for the marker, EMG and Force plate data
- Foot strike and toe-off events for three gait cycles centred around Force plate one
- Plug in Gait kinematics results
- Recorded subject data including subject mass and anatomical measurements

The MVC C3D files contain only the labelled EMG data. The static files contained only the labelled marker and force plate data.

4. Pre-processing

A single C3D file is received from the laboratory with all the necessary information for each trial. The information includes the marker positions, the ground reaction forces as well as the muscle activation signals. Pre-processing is performed for the data to be usable in OpenSim.

The pre-processing procedure followed for this project achieves three goals (as shown in Figure 14). Data are placed in logical and user-friendly locations creating a user-friendly filing and naming system. It extracts relevant information and places it in the relevant files and folders with the correct naming conventions so that it is usable by OpenSim. To feed the relevant data to OpenSim, non-real information and artefacts are removed, and the data are filtered and cleaned. The pre-processing is performed using scripts written in *MATLAB* (Mathworks, 2017). The description of each pre-processing step follows.

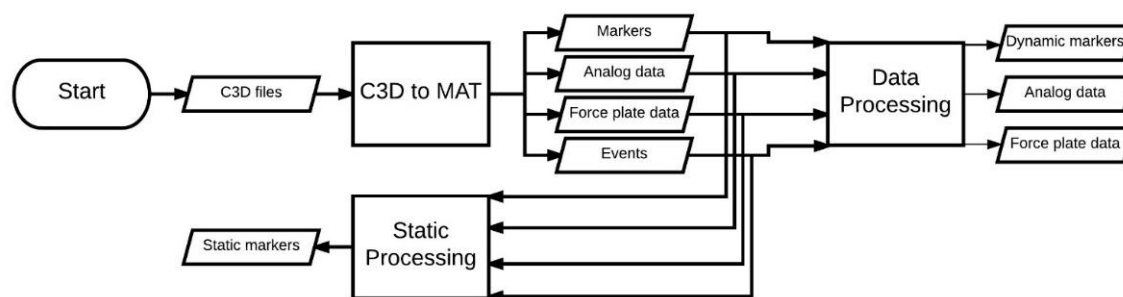


Figure 14: Pre-processing flow diagram

4.1. Acquisition

Before starting the pre-processing pipeline, it is necessary to create an acquisition settings file, which describes the acquisition of the data during one session. It also includes information which is specific to the lab in which the tests are performed, as well as project specific marker and EMG protocols. The lab, marker and EMG information is saved in separate settings files which can be loaded into and added to the acquisition settings file for each new session of every subject. The inputs and setup files for the Acquisition process are shown in Figure 123 of Appendix G.1. MOtoNMS.

The laboratory specifications include details relevant to the laboratory, which can be used in every acquisition settings file for the project. The following settings are specified. The orientation of the global coordinate system of the laboratory in which the experiments took place; the Motion Lab coordinates are as follows: Y – direction of motion, Z – vertical axis, X – right-hand rule. The force plate type. Different force plates return different data. The force plates in the Motion lab are type two, and so

output their data as follows: $[F_x F_y F_z M_x M_y M_z]$. The rotation between the force platforms and the global coordinates describe the orientation of each force plate within the global coordinate system. The force plate's rotations performed to line up the force plate coordinate system with the laboratory coordinate system is described in Table 7, and shown in Figure 13.

Table 7: Force Plate frame local to global rotations

Force plate	Rotation about X (deg)	Rotation about Y (deg)	Rotation about Z (deg)
1	180	0	90
2	0	180	0
3	0	180	0

The markers protocol contains the markers used during the dynamic trials and the markers used during the static trial separately. The EMG protocol contains a list of instrumented muscles as well as which leg is instrumented. This information is described above in Experimental procedure. The information specific to the session is the trial list, which includes the trial type (walk or static), the repetition number, the motion direction, as well as the description of which foot hits which force plate for each trial. This information will be used during the pre-processing.

4.2. C3D to MAT

The first step of the pre-processor is to extract the relevant information from the C3D files and place it in separate, organised files that are readable by *MATLAB* (.mat files). This tool makes use of the open-source freely available Biomechanical ToolKit (Barre and Armand, 2014). For C3D2MAT to run, it is necessary that the user specifies the input directory containing the C3D files. New subfolders for each trial (i.e., each C3D file in the input folder) are created within a *sessionData* folder. Within these folders, separate .mat files are created containing marker data, force platform data, analogue data which contains the EMGs as well as the events within the C3D which contain the points at which foot strike and foot off occur for each foot. The marker labels, analogue data labels, subject data recorded during the session, force platform information and rates are common to all the trials and are therefore saved in separate files in the *sessionData* folder, as shown in Figure 120 of Appendix F. Folder layout. The inputs and outputs of C3D to MAT are shown in Figure 122 of Appendix G.1. MOtoNMS.

4.3. Data processing

Data processing is responsible for processing dynamic trials, to create usable input files for OpenSim. Data processing contains three major steps: marker elaboration, GRF elaboration and EMG processing. During marker elaborations, a piecewise cubic interpolation takes place on the marker trajectories to fill potential gaps. Interpolation only takes place if the gap is smaller than a user-specified maximum gap size. The value is assigned relative to a 60 Hz frame rate, so a specified gap used at a different frame rate is calculated and set.

Force Plate and marker filtering have a significant effect on the calculation of moments and forces at joints in the musculoskeletal model. The built-in filter is a zero-lag low-pass second-order Butterworth filter, with the cut-off frequency chosen by the user. This filter is applied to both the marker data and the force plate data. To remove noise and motion artefacts from marker data, some high-frequency components of movement are removed. If the force plate data are not filtered accordingly, a mismatch occurs between the marker data and force plate data, and high residual forces occur. An investigation of the effects of different filtering frequencies is performed in Residual Reduction Algorithm.

The above processing procedure is performed over a specific analysis window. For this project, the analysis window was automatically determined using the events file saved during the C3D to Mat step. The analysis window was chosen as the period from the first event to the last event. Finally, force plate and marker data are projected onto the global coordinate system used in OpenSim. The rotations and directions are taken from the description of motion direction and force plate rotations described in Acquisition.

The files produced by Data processing are shown in Figure 120 of Appendix F. Folder layout, under the file *dynamicElaborations*. Figure 124 of Appendix G.1. MOtoNMS shows the inputs and outputs of Data processing in a flow diagram.

4.4. Static processing

The purpose of static processing is to create a file containing static trial marker trajectories to be used during the scaling process in OpenSim. Static elaboration applies the same filtering procedure to the forces and markers that take place during the data processing step, so the main difference is the joint centre estimation. The software can estimate the hip, knee and ankle joint centre. The knee and ankle joint centres (KJC and AJC respectively) are calculated by taking the midpoint between specified markers in the setup file while the hip joint centre (HJC) is calculated using the procedure described in Harrington *et al.* (2007).

The HJC is calculated using the superior anterior iliac spine markers and the posterior superior iliac spine markers. The AJC is calculated using the lateral and medial knee markers, and the KJC is calculated using the medial and lateral knee markers. During the experimental procedure, it was not possible to place medial knee markers on all subjects due to contact during the walking trials. For these subjects, it was not possible to calculate the KJC. Figure 125 of Appendix G.1. MOtoNMS shows the inputs and outputs of the static processing tool.

5. OpenSim

OpenSim ([Opensim.stanford.edu](https://opensim.stanford.edu), 2017) is a freely available tool for musculoskeletal modelling and dynamic simulation. OpenSim has an active online community that connects researchers and facilitates the sharing and creation of simulations that can be analysed, improved and tested through collaboration.

This chapter covers the full OpenSim pipeline. The computational pipeline is outlined as well as each step of the pipeline regarding its theory, where it fits into the automated computational procedure and the results for that section. Figure 15 shows an overview of the OpenSim pipeline (Step B), and how it fits into the full pipeline. Figure 126 in Appendix G.2. OpenSim shows a more detailed description of the pipeline with Figure 127 to Figure 132 showing the relationship between respective steps.

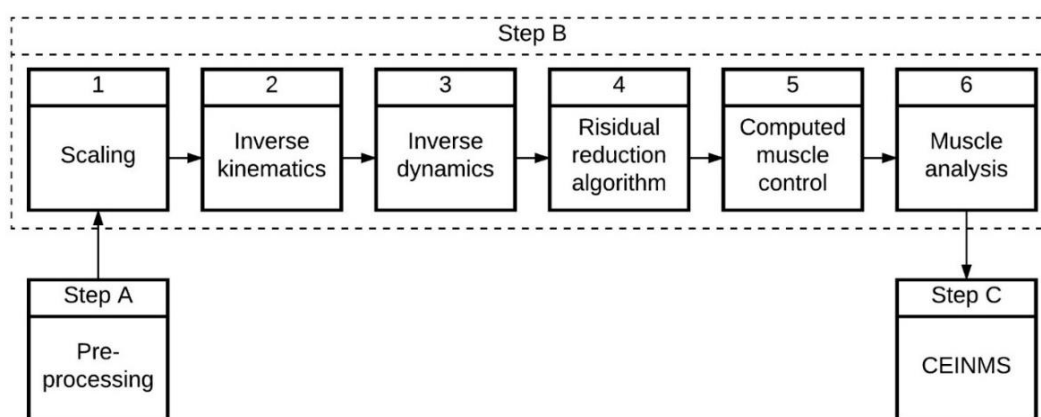


Figure 15: Computational pipeline flow diagram

5.1. Batch processing

Traditionally OpenSim is run through its user interface. This requires the user to manually input all the required descriptions to run that particular function. Alternatively, the user can edit the Extensible Markup Language (XML) files manually or by using the existing OpenSim application programming interface (API).

For this project an existing OpenSim project, Batch OpenSim Processing Scripts (BOPS) ([BOPS Simtk.org](https://bops.simtk.org), 2017) was modified and improved to run automatically through the full pipeline. The automated pipeline was also modified to loop through subjects which had the relevant inputs created during the Pre-processing. Figure 126 to Figure 132 of Appendix G.2. OpenSim outlines the modelling pipeline and provides detailed flow diagrams of the inputs and outputs for every step of the pipeline.

5.2. Scaling

The purpose of the scale tool is to adjust the anthropometry of a generic OpenSim musculoskeletal model to match that of a specific subject as closely as possible. The pre-scaled model used is the *gait2392* model supplied by OpenSim and discussed above in the Literature Review. This model contains 23 degrees of freedom, with 92 musculotendon actuators that represent 76 muscles in the lower extremities and torso. The generic model contains virtual markers that match the anatomical placement of markers on the subject. Weightings are then assigned to these markers based on the level of confidence of the placement on the subject. The markers that are placed on bony landmarks contain the highest level of confidence. Figure 16 shows the relationship between the virtual and experimental markers.

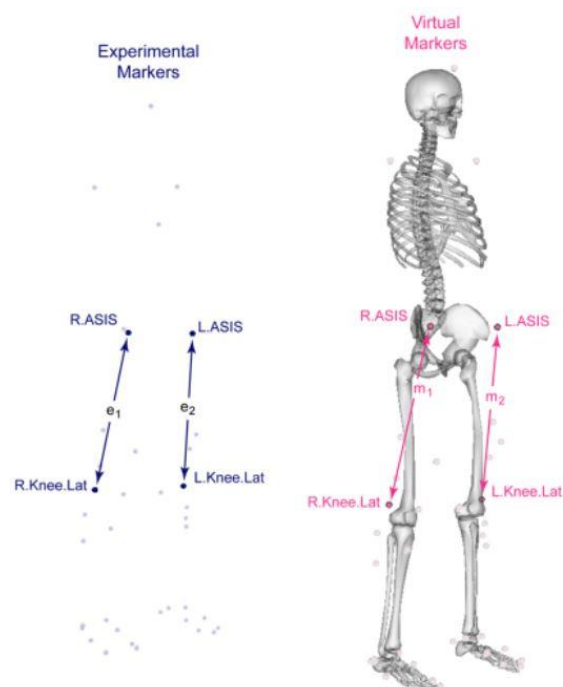


Figure 16: Scale factor calculation (Simtk-confluence.stanford.edu, 2017)

Scaling is performed during four major steps. First, scale factors are calculated. For each segment, scale factors are calculated using experimental distances between experimental markers (in blue in Figure 16) relative to the distance between the same virtual marker pair on the generic model (in pink in Figure 16). The experimental marker positions are taken from the static marker trajectories file output by the static processing step of the pre-processor. The distance (e_1 and e_2) is then calculated by taking the average distance between the two markers across a set of specified frames during the static trial. The virtual marker distance (m_1 and m_2) are taken from the generic model in its default pose. The scale factors are then calculated as follows:

$$s = \frac{s_1 + s_2}{2} \quad (1)$$

where:

$$s_1 = \frac{e_1}{m_1} \text{ and } s_2 = \frac{e_2}{m_2} \quad (2)$$

Table 8: Segment scaling marker pairs

Segment	Scaling pair one	Scaling pair two
Pelvis	RASI LASI	RPSI LPSI
Foot	RHEE RTOE	LHEE LTOE
Thigh	RKJC RHJC or RKNE RHJC	LKJC LHJC or LKNE LHJC
Shank	RKJC RAJC or RKNE RAJC	LKJC LAJC or LKNE LAJC
Torso	C7 LPSI	-

Secondly, the model's geometry is then scaled based on the scale factors calculated above, from the marker pairs listed in Table 8 (markers list detailed in Appendix A. Marker labels). This includes the joint frame locations, mass centre location, force application points as well as muscle attachment points. The KJC markers were used for scaling if the medial knee markers were present. Otherwise, the lateral knee markers were used in place of the joint centre markers. Kainz *et al.* (2017) have shown that using joint centres to scale a musculoskeletal model has a significant increase in accuracy, particularly for the thigh and shank segment.

Thirdly, after the geometry has been scaled, the mass of the model is adjusted to correspond to the mass of the subject. The *preserve the mass distribution* setting is applied to maintain the generic mass distribution of the body segments. Finally, the optimal fibre length and tendon slack length, which are length-dependent components, are modified using a ratio calculated from the length before scaling to the length after scaling.

Once the scaling process is completed, the scaling tool adjusts the virtual marker positions to match the experimental marker positions, again based on a set of user-specified weightings. A weighted least-squares (WLS) problem is used to calculate the marker adjustment, the WLS problem is discussed further below in Inverse Kinematics. The output of the scale tool is the scaled and adjusted subject-specific model. The Root Mean Square (RMS) and maximum marker error for the specific marker with the most significant error are also recorded. The error is the distance between the virtual marker and the experimental marker at the end of the scaling process. OpenSim advises that the errors should be below 10 millimetres for the RMS error and below 20 millimetres for the maximum marker error for bony

landmarks. If the errors are not within the stipulated bounds, it is recommended that the virtual markers are adjusted in the generic model to better match the experimental marker placements.

5.3. Inverse Kinematics

The aim of the Inverse Kinematics (IK) tool is to produce joint angles (defined in OpenSim as coordinates) and marker translations that best match the experimental positions observed in the testing procedure. The kinematics of the rigid segments is limited by the joints setup inherent in the OpenSim model, as seen in Chapter 2.3.

The marker and coordinate “matching” is achieved mathematically through a weighted least squares problem, where the solutions attempt to minimise both the marker and coordinate errors. The marker error is the distance between the computed model markers calculated by IK and the experimental markers. Similarly, the coordinate error is the difference between the computed coordinate in IK and the experimental coordinate, where the experimental coordinates are joint angles obtained directly from the motion capture system. The inclusion of the coordinate tracking is optional. This case is a weighted problem because the user specifies specific weights to markers for which there is higher confidence. The equation for the WLS problem is as follows:

$$\min_q \left[\sum_{i \in \text{markers}} w_i \|x_i^{\text{exp}} - x_i(q)\|^2 + \sum_{j \in \text{unprescribed coords}} \omega_j (q_j^{\text{exp}} - q_j)^2 \right] \quad (3)$$

Where q is the vector of generalised coordinates, w_i are the marker weights, ω_j are the coordinate weights. The first term is the weighted difference between the experimental marker position, x_i^{exp} and the position of the corresponding marker on the model, $x_i(q)$. The second term is the weighted difference between the experimental coordinate, q_j^{exp} and the value of the coordinate at j , q_j .

The inputs for the IK tool are the scaled subject-specific musculoskeletal model, the experimental marker trajectories, with the experimental coordinates excluded, as shown in Figure 128 of Appendix G.2. OpenSim. Weightings for each marker on the model are applied based on the confidence of the marker placement. Along with the generalised coordinates, the IK tool also provides the user with RMS and maximum marker error. OpenSim advises that these values remain below 20 millimetres and 40 millimetres respectively.

5.4. Inverse Dynamics

The aim of the Inverse Dynamics (ID) tool is to generate net forces and torques at each joint that account for the known motion of the model. The ID tool requires the model kinematics which it uses in conjunction with the ground reaction forces to calculate the generalised forces and torques at the joints.

The generalised positions, velocities, and accelerations define the motion of the model. Consequently, the forces and torques at each joint are calculable using only the motion of the subject. Due to the simplification of the musculoskeletal model, loss of realistic movement data through filtering and other errors, accuracy can be improved significantly by including the ground reaction forces. Net joint torques and forces at each joint are solved using Newton's Equations of Motion, in the form of equation (4).

$$M(q)\ddot{q} + C(q, \dot{q}) + G(q) = \tau \quad (4)$$

where

$q, \dot{q}, \ddot{q} \in R^N$ are the vectors of generalised positions, velocities and accelerations, respectively, and N is the number of degrees of freedom.

$M(q) \in R^{N \times N}$ is the system mass matrix.

$C(q, \dot{q}) \in R^N$ is the vector of Coriolis and centrifugal forces.

$G(q) \in R^N$ is the vector of gravitational forces.

$\tau \in R^N$ is the vector of generalised forces that is being determined.

All of the terms on the left-hand side of equation (4) are known through direct measurement or based on estimations or assumptions, with the vector of generalised forces unknown. The inclusion of the ground reaction forces eliminates and informs some of the unknowns on the right-hand side, allowing for a faster and more accurate calculation.

The inputs for the ID tool are the scaled subject-specific musculoskeletal model created in the Scaling procedure, the generalised coordinates from the IK procedure and the external reaction forces extracted from the C3D files during Data processing, as shown in Figure 130 of Appendix G.2. OpenSim. The external loads, output in Data processing, are described in a separate settings file, *external_loads.xml*. This file contains the link to the GRFs as well as a description of which foot hit which force plate. This information is automatically written to the

external loads file based on the descriptions in the events file, and the acquisition file described in C3D to MAT and Acquisition respectively.

5.5. Residual Reduction Algorithm

The purpose of the Residual Reduction Algorithm (RRA) is to create an adjusted subject-specific musculoskeletal model that is more dynamically consistent with the kinematics and GRF. This dynamically consistent model reduces the residual forces that counter the non-real effects of the model.

The musculoskeletal model contains 23 degrees of freedom, 17 of which occur between the rigid joints of the model, and the other 6 degrees of freedom are three rotational and three translational between the pelvis and the ground. During processing large compensatory forces, which account for the six degrees of freedom between the pelvis and the ground, are applied to the pelvis to reduce modelling errors and assumptions (for example, a model with no arms) as well as non-real kinematics due to marker data processing. Because of the aforementioned dynamic inconsistencies, the GRF and accelerations do not satisfy Newton's Second Law,

$$F = ma. \quad (5)$$

The residuals are therefore applied to account for the inconsistency:

$$F_{exp} + F_{residual} = \sum_{i=1}^{segments} m_i(a_i - g) \quad (6)$$

where each body segment i has a mass of m_i and an acceleration of a_i with g being the acceleration due to gravity. The residuals are determined over the full duration of the specified movement. The centre of mass (COM) of the model's torso is adjusted slightly to reduce the residual forces, after which the RRA is applied to alter the kinematics, \vec{q}_{ik} , as shown in Figure 17.

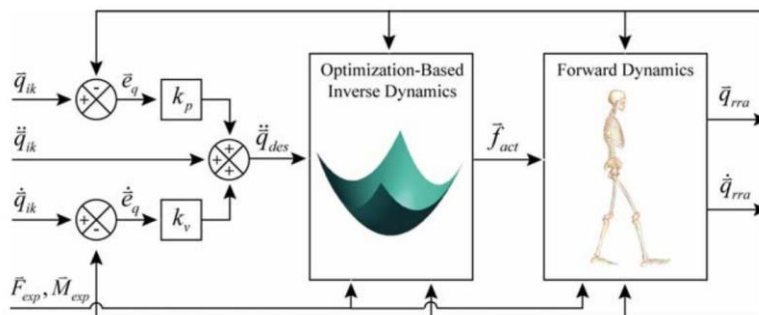


Figure 17: RRA schematic (Anderson *et al.*, 2006)

After the adjustment of the torso, adjustments are made to the kinematics to solve a control problem. The control problem uses idealised joint moments to control each joint and residual forces to actuate the six degrees of freedom between the model and the ground. The algorithm performs a forwards dynamic simulation, computing actuator forces, $\vec{f}_{act}(t)$, that will move the model from its current position, $\vec{q}_{rra}(t)$, towards the desired position, $q_{ik}(t + T)$, in the next time step, as shown in Figure 17.

The actuator forces are determined by minimising a performance criterion,

$$J(\vec{f}_{act}) = \sum_{i=1}^{Act} w_i \left(\frac{f_{act,i}}{f_{act,i}^{opt}} \right)^2 + \sum_{i=1}^{Act} \omega_i \left(\ddot{q}_{des,i}(t + T) - \ddot{q}_{rra,i}(t) \right)^2 \quad (7)$$

where $f_{act,i}$ and $f_{act,i}^{opt}$ are the force and optimal force of the i^{th} actuator respectively. w_i and ω_i are the weights in the actuator stresses and acceleration errors respectively. $\ddot{q}_{des,i}(t + T)$ is the desired acceleration of the i^{th} model coordinate. The desired coordinates are computed using a proportional-derivative control law, their calculation, and relationship to the IK coordinates is shown in Figure 17 and are described as follows:

$$\begin{aligned} \ddot{q}_{des,i}(t + T) = & \ddot{q}_{ik,i}(t + T) + k_v \left(\dot{q}_{ik,i}(t) - \dot{q}_{rra,i}(t) \right) \\ & + k_p \left(q_{ik,i}(t) - q_{rra,i}(t) \right) \end{aligned} \quad (8)$$

where k_v and k_p are gains on the velocity and position errors respectively. The first six actuator forces calculated in equation (8) are the residuals and, the remaining components are the joint moments. The new kinematics, $\vec{q}_{rra}(t)$, differs slightly from the original kinematics, $q_{ik}(t)$, allowing the residuals to be reduced (Anderson *et al.*, 2006).

The inputs for the RRA tool are two settings files, the scaled subject-specific model, the kinematics calculated from the IK tool and the GRF data as shown in Figure 130 of Appendix G.2. OpenSim. The ground reaction force data are described in the same external load's file used in ID. The settings files used in RRA are the RRA tracking tasks and RRA actuators. The tracking tasks file assigns weightings to joint angles to define how strictly each one is tracked, which allows joints with a high level of confidence to be tracked more accurately. The RRA actuators file contains the ideal force or torque actuator that is applied to every degree of freedom of the body. Six residual actuators are applied to the scaled pelvis, and the other 17 coordinate actuators are applied between the rigid joints and replace the model's muscles.

5.6. Computed Muscle control

The purpose of Computed Muscle Control (CMC) is to compute the excitations to individual muscles that drive the subject-specific dynamic musculoskeletal model. CMC uses feedforward and feedback control to drive the kinematics of the dynamic model to match a set of desired kinematics, which in this case is the output of the RRA. This approach is an extension of the approach taken by Lewis *et al.* (1993) described by Thelen *et al.* (2003).

Before the actuator controls calculated by CMC can be determined it is necessary to calculate the initial states first, which can then be input into the algorithm. The states are made up of the generalised coordinates, generalised speeds, as well as the muscle states. Initial values of generalised coordinates and speeds can be determined directly from the kinematics. However, initial muscle states are unknown. CMC therefore applies the first 0.030 seconds of simulation to calculating the initial states, which are then applied to the tracking algorithm.

CMC achieves the tracking through a combination of proportional-derivative control and static optimisation, as shown in Figure 18.

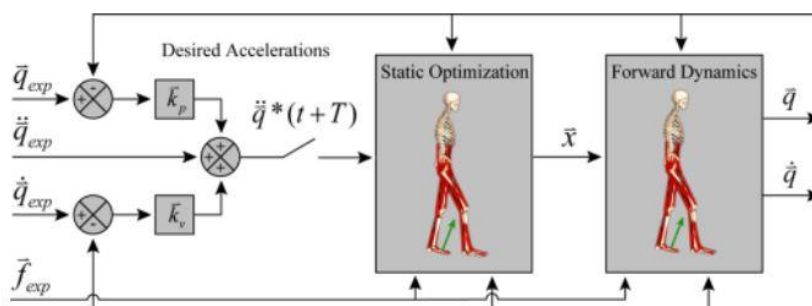


Figure 18: CMC schematic (Thelen *et al.*, 2006)

The first step in the CMC algorithm, as shown in Figure 18, is to calculate a set of desired accelerations, $\ddot{\vec{q}}^*$. These accelerations will drive the model coordinates, \vec{q} toward the experimentally determined coordinates, \vec{q}_{exp} . The desired accelerations are therefore determined using the following proportional-derivative control equation:

$$\ddot{\vec{q}}^*(t+T) = \ddot{\vec{q}}_{exp}(t+T) + \vec{k}_v[\ddot{\vec{q}}_{exp}(t) - \ddot{\vec{q}}(t)] + \vec{k}_p[\dot{\vec{q}}_{exp}(t) - \dot{\vec{q}}(t)] \quad (9)$$

Where \vec{k}_v and \vec{k}_p are the feedback control gains on the velocity and positional errors. T represents a minor step in the future at which accelerations are computed.

This is necessary because the muscle forces that are applied to the body cannot change instantaneously. T is left at its default value of 0.010 seconds. If the desired accelerations are achieved, the errors are driven to zero. In order for this process to occur in a critically damped fashion, the velocity gain can be chosen using the following relation:

$$\vec{k}_v = 2\sqrt{\vec{k}_p} \quad (10)$$

The second step in CMC computes a set of actuator controls, \vec{x} , that when input into the system equations of motion will realise the desired accelerations, $\ddot{\vec{q}}^*(t + T)$. Muscle excitations act as actuator controls, although any actuator could be used. The loads are distributed across associated actuators using static optimisation. CMC formulates the static optimisation problem in one of two ways, either the slow target or the fast target optimisation. The slow target is described in equation (11) as follows:

$$J = \sum_{i=1}^{n_x} x_i^2 + \sum_{j=1}^{n_q} \omega_j (\ddot{q}_j^* - \ddot{q}_j)^2 \quad (11)$$

The performance criterion, J , is a weighted sum of squared actuator controls and the sum of desired acceleration errors. The desired acceleration errors, drives the model accelerations, \ddot{q}_j toward the desired acceleration, \ddot{q}_j^* . The fast target technique is similar to the slow target with the elimination of the acceleration errors, and the inclusion of an equality constraint. The fast target is explained in equation (12) as follows:

$$J = \sum_{i=1}^{n_x} x_i^2 \quad (12)$$

$$C_j = \ddot{q}_j^* - \ddot{q}_j \quad \forall j$$

The fast target technique requires the set of equality constraints, C_j , to be minimised to within a prescribed tolerance set for the optimiser. This method is faster and produces better results (Thelen *et al.*, 2006), however it will fail if the constraint is not met. This failure occurs if the musculoskeletal model muscles are not strong enough to reproduce the desired accelerations.

To limit the failure of the fast target method, reserve actuators are augmented to the model to account for strength deficiencies in the muscles. These reserve actuators have a low optimal force and therefore require high excitations to apply significant loads to the model. These high excitations are penalised in both the slow

and fast target techniques. The reserve actuator values should be low relative the primary actuators, indicating that the model is strong enough.

The final step of CMC, as shown in Figure 18, is a typical forward dynamic simulation. Within every time step, T , the desired accelerations are calculated, the static optimisation is run and the forward dynamics simulation is performed. This procedure is performed until the end of the prescribed time period.

The inputs to the CMC tool are three setup files, the kinematics from RRA, the adjusted subject-specific model created during RRA as well as the ground reaction forces extracted during the Data Processing step of the pre-processing. Again the ground reaction forces are described in an external loads description file which is the same one as used in RRA, with the kinematics updated to that calculated during RRA.

The three setup files used in CMC are the CMC tasks, CMC Actuators and CMC control constraints. The tasks setup file, like the RRA tasks file, specifies which joint angles in the model should follow the desired kinematic trajectory, and a relative weighting is applied to adjust the accuracy to which coordinates are tracked. The CMC actuators file performs the same function as the RRA actuators file, containing ideal force and torque actuators for every degree of freedom of the model.

The Control Constraints file is only used in the CMC function. Each actuator in the model has a maximum and minimum *excitation* value set in the control constraints file. These maximums and minimums act to limit the controllers to stay within the prescribed values. The control constraints can also be used to set individual actuators on or off, and the range in which they act. The inputs and outputs of the CMC tool are shown in Figure 131 of Appendix G.2. OpenSim.

5.7. Analyses Tool

The purpose of the analyses tool is to produce results of an existing simulation. The tool steps through the given set of input data specifying the state of the model, and runs a prescribed analysis at each step, depending on the required output data. For this project, it was only necessary to use the *BodyKinematics* and *MuscleAnalyses* tools provided within the analyses tool.

The input to the Analyse tool are the states and the controls which are both outputs of the CMC tool. The external reaction forces applied to the model are also included in the inputs. The states are variables of a model that are governed by differential equations. These are values that are integrated during a simulation which are the generalised coordinates and velocities and are required to specify the configuration of every model. Muscle states, fibre lengths and muscle activations are examples of muscle states (Simtk-confluence.stanford.edu, 2017).

The controls of a model are the variables used as the control parameters in optimisation problems. Controls are independent variables, like muscle excitations, which are not governed by differential equations but are free to take on values between one and zero. The external loads are the same as those applied during ID, RRA and CMC, describing the forces applied to each foot.

The outputs of the body kinematics function are the centre of mass and orientation positions of each rigid body within the model, their velocities and their accelerations. This includes the position, velocity and acceleration of the overall centre of mass of the model. The output of the muscle analyses tool are the moments and moment arms at each degree of freedom of the model, as well as muscle and tendon lengths.

5.8. OpenSim results

The assessment of the OpenSim results in this project is multi-faceted. It is first necessary to ensure that the input data, as well as the pipeline up to the point being studied, are producing results that are in line with the literature. The results can then be checked for repeatability. After this, if reliable results are being produced, they can be looked at clinically.

In general, for this report, the results are plotted per session per leg. This is done for two reasons. Firstly, it is known that the results of the scaling and the kinematics are sensitive to marker placement (Szczerbik and Kalinowska, 2011). Therefore, the legs are plotted separately so as not to distort the effects of leg-specific marker placement through averaging. It is also important to note that the results of each leg are separate because they come from separate trials. This occurs because when analysing trials, only the results of the full gait cycle beginning at the footstrike of force plate one (the middle force plate as shown in Figure 13) can be analysed. This is because this gait cycle has the full set of known ground reaction forces for the full cycle.

Secondly, the subjects are separated for similar reasons. Again, changes due to marker placement would be distorted, hidden or smoothed due to averaging. Also, subjects have different risk factors and affected legs, so their abnormalities would be hidden when averaging across subjects. Plotting each leg and session separately allows a deeper level of scrutiny however it is not possible to plot the details for every subject in the body of the report due to space constraints. Results for subjects which indicate the observed trends are therefore displayed in the body, and the results for the remaining subjects are placed in the appendices.

When comparing sessions, it is important to note that subject AKP 03 and AKP 16 both only had two trials on their unaffected leg (right and left respectively) in session 4, so although it appears that there is better repeatability for those sessions,

there are in fact fewer trials. Every other session for all the subjects had three trials per leg in every session.

5.8.1. Scaling

One of the principal aims of this project is to create a pipeline, which can be applied to a range of subjects automatically, and part of achieving that objective is to identify critical points at which problems might occur. Scaling is one such point. The scaling process is sensitive to marker positions, and changes in marker positions across sessions affect the kinematics and scaling of the subjects (Szczerbik and Kalinowska, 2011). This project is particularly susceptible to this problem due to the time between testing sessions.

To automate the pipeline, it is necessary to reduce the user input at each step. This translates to creating a generic model that can be used across a broad sample of subjects that maintains acceptable scaling errors. Table 9 shows the RMS and maximum scaling errors for each subject during each session. The markers which were responsible for the maximum error are listed alongside the distance they were adjusted by.

Table 9: Scaling errors calculated in OpenSim

Subject	Session 1 (mm) [marker]		Session 4 (mm) [marker]	
	RMS	Max	RMS	Max
AKP03	22.2	34.0 [CLAV]	23.5	38.4 [RASI]
AKP16	29.7	53.7 [T10]	32.7	59.2 [RTHI]
AKP17	26.7	41.7 [RTHI]	2.2	05.4 [C7]
AKP29	1.9	5.4 [C7]	26.2	54.2 [LASI]
AKP30	1.8	4.2 [C7]	31.1	66.8 [RASI]
	Green: low marker error		Red: high marker error	

Markers can be placed in two categories: technical markers and anatomical markers. Anatomical markers are placed on the bony landmarks and are used to calculate the scaling factors discussed above; these markers need to be placed at the exact point. Technical markers are not placed at bony landmarks and are used in conjunction with anatomical markers to create local frames for rigid segments (as discussed in the Kinematics and kinetics section of Biomechanical Information and shown in Figure 7). These markers do not need to be placed in exact locations, but rather along a particular axis. It is, therefore, necessary that they are moved to the position in which they occur experimentally. From Table 9 it is clear that the majority of the markers at which the maximum errors occur are not at bony landmarks and are in fact technical markers.

The OpenSim User manual (Delp *et al.*, 2007) recommends that for anatomical markers errors should remain below 10 millimetres and 20 millimetres for RMS and maximum errors respectively. It is clear from the table that this was not always achievable with the automated pipeline. To reduce user intervention, and increase the speed of the procedure of the automated pipeline, it is not feasible for the user to update the generic model for each subject. A compromise needs to be made to allow for each model to be as close to acceptable errors as possible. This requires accurate marker placement during the experimental phase that corresponds across subjects and sessions.

An intra-subject comparison is particularly sensitive. When comparing subjects to themselves, it becomes more important to place anatomical markers in the corresponding and correct positions, otherwise, differences between ensuing results become less comparable due to the introduction of session differences. As described above, the first step of scaling is to calculate scale factors that are used to create a subject-specific musculoskeletal model by enlarging or reducing the five segments shown in Table 8. Table 10 shows the percentage change in the scale factors of the first and final session for each segment.

Table 10: Percentage change between segment scaling factors

Segment	AKP03 Δ	AKP16 Δ	AKP17 Δ	AKP29 Δ	AKP30 Δ
Pelvis	0.77	-1.03	-2.74	-9	-15.9
Foot	0.2	-0.1	0.91	1.06	1.09
Thigh	-1.93	3.34	1.57	-1.34	2.65
Shank	3.04	-1.61	-3.58	-2.56	-3.68
Torso	0.07	-4.33	2.05	5.5	1.59
	Green: no intervention			Red: markers adjusted	

This table shows the variability between marker placements of anatomical markers. If the markers are placed in the identical positions, these values should be zero. The generic model was only adjusted during the scaling procedure if the percentage change across sessions was higher than 5%. Otherwise, the automated procedure ran through the scaling process uninterrupted. Consequently, only subject AKP 29 and AKP 30 were adjusted to improve scaling performance.

5.8.2. Inverse Kinematics

Kinematic differences in gait between PFP sufferers and healthy subjects has been shown to be inconclusive (Barton *et al.*, 2009). In the review performed by Barton *et al.* (2009) kinematic differences for PFP sufferers were as follows: differences in rearfoot kinematics, reduced and earlier peak hip internal rotation and the most significant finding, a reduction in knee flexion angle at heel strike and early stance.

These findings, however, were inconsistent between studies. Figure 19 and Figure 20 show the average kinematics for the gait cycle of all the subjects for session one and session four respectively.

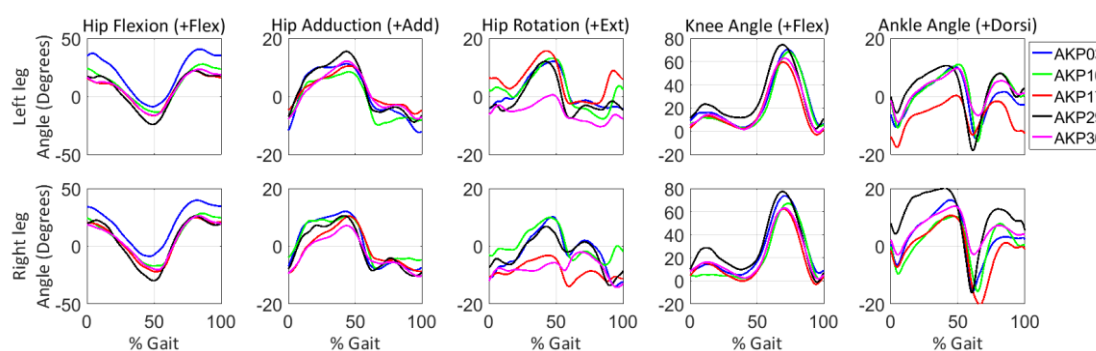


Figure 19: Subject comparison of IK averages for session one

Upon inspection of Figure 19 and Figure 20 it is clear that while the shape is consistent across subjects, there is often an offset for a particular subject, for example, the right ankle angle of subject AKP 29 in session one, or the right hip rotation of subject AKP 17 in session 4. While these results might reflect some change from the norm, it is also hypothesised that these offsets are due to marker misplacement. The ankle angle and hip rotation angle are particularly susceptible to these errors because the markers used to calculate these angles are close together, so their shapes are more sensitive to misplacement.

Nadeau *et al.* (1997) studied the gait of subjects with patellofemoral pain syndrome and reported on the hip flexion, knee flexion and ankle flexion. The results that are shown in this study match the results reported in that study. There are exceptions, however. In session one subject AKP 16 shows almost no knee flexion in the stance phase for the right leg trials. While Nadeau *et al.* (1997) and Barton *et al.* (2009) found a reduction in knee flexion during stance, and this is the risk factor for this subject (as shown in Table 6) it is still out of the reported bounds for the knee flexion to be zero during stance.

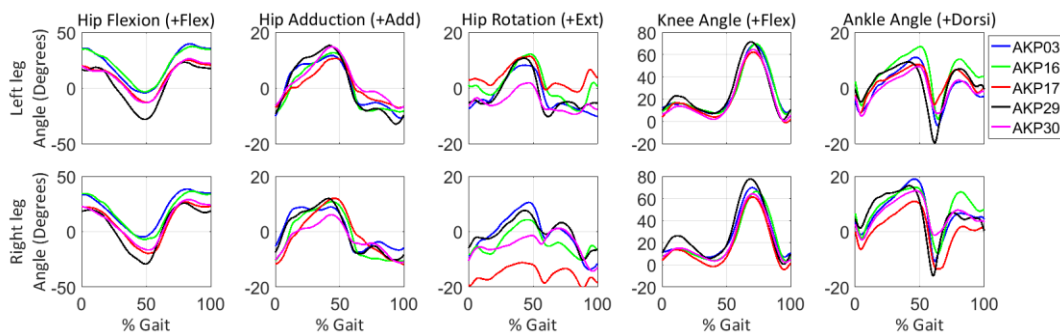


Figure 20: Subject comparison of IK averages for session four

Hip rotation and hip adduction results require special consideration. The lower extremity kinetic chain is made of the hip, knee and ankle joint (Palmitier *et al.*, 1991). The simplification of the knee joint as a one degree of freedom joint in OpenSim then affects the joints in series in the kinetic chain. The lack of the ability for the knee to rotate internally and externally, or to have any adduction-abduction movement, translates these rotations to the hip and the ankle.

Figure 21 shows the comparison of the IK results between sessions for subject AKP 16. The shaded region shows the maximum and minimum region for each session while the bold lines indicate the average. Figure 47 to Figure 50 in the B.1. Inverse Kinematics section of the Appendices shows the same comparison for the remaining subjects.

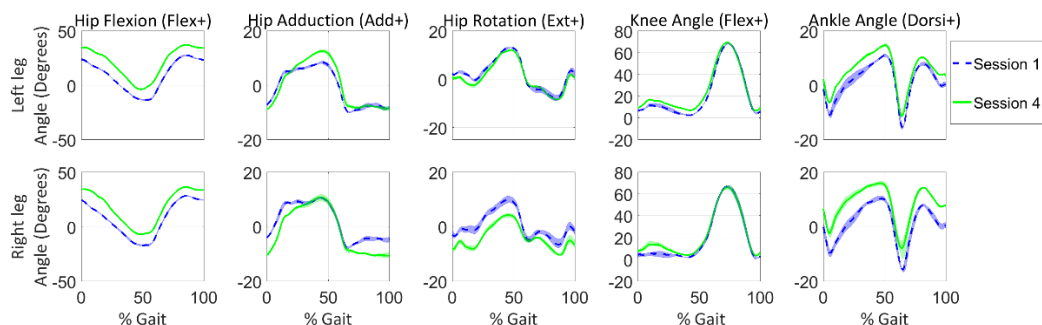


Figure 21: Session comparison of the IK for subject AKP 16

Figure 21 and the figures in the B.1. Inverse Kinematics section of the Appendices serves two purposes. They allow a comparison of the pre- and post-intervention kinematics and make the repeatability of each session apparent. The thickness of the shaded region represents the repeatability of trials across a session. All of the subjects show good repeatability between trials in a session. Table 11 shows the coefficient of determination (COD) between sessions for the kinematics of every subject. There is a high repeatability between sessions on average ($R^2 = 0.93 \pm 0.11$).

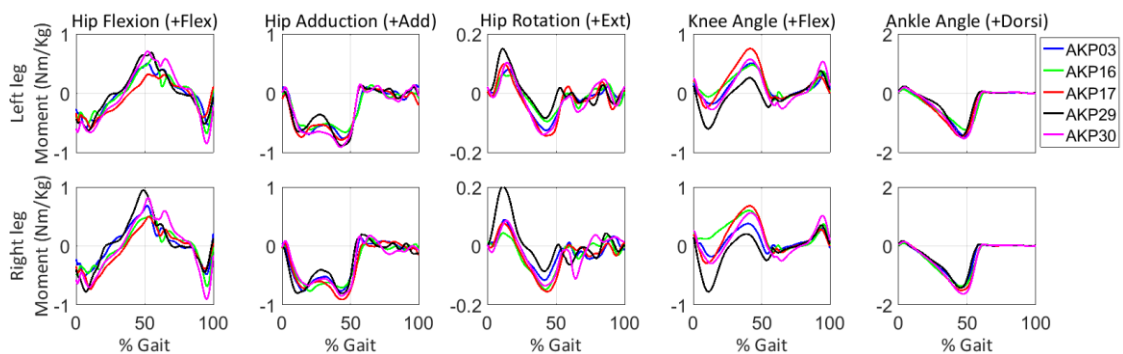
Table 11: Inter-session coefficient-of-determination values for IK

Joint	AKP 03 (R^2)		AKP 16 (R^2)		AKP 17 (R^2)		AKP 29 (R^2)		AKP 30 (R^2)	
	Left	Right								
Hip Flexion	(0.99)	(1.00)	(0.99)	(0.98)	(0.98)	(0.99)	(0.99)	(0.99)	(0.99)	(0.99)
Hip Adduction	(0.97)	(0.98)	(0.94)	(0.91)	(0.93)	(0.96)	(0.98)	(0.98)	(0.97)	(0.95)
Hip Rotation	(0.94)	(0.98)	(0.97)	(0.83)	(0.83)	(0.44)	(0.91)	(0.85)	(0.81)	(0.88)
Knee Angle	(0.97)	(0.99)	(0.99)	(0.98)	(0.95)	(0.98)	(0.98)	(0.98)	(0.99)	(0.97)
Ankle Angle	(0.83)	(0.98)	(0.98)	(0.93)	(0.42)	(0.91)	(0.82)	(0.94)	(0.92)	(0.95)

As with the subject comparison, there is again an offset between sessions which is responsible for the lower COD values, (as shown in AKP 17's right hip rotation visible in Figure 48 in Appendix B.1. Inverse Kinematics). As detailed above it is hypothesised that this is due to an offset in the marker placement. It is, therefore, more appropriate to compare the change in shape between the sessions rather than the absolute change.

5.8.3. Inverse Dynamics

The ID results show the net moments at each joint. The moments will ultimately be used in the computation of muscle forces further down the pipeline. However, they also offer an insight into what is occurring at the particular joint. Figure 22 and Figure 23 show the average dynamics for the separate leg of every subject, normalised by their body weight. The results show an agreeable shape across subjects.

**Figure 22:** Subject comparison of ID averages for session one

Subject AKP 29, being the primary exception, shows an increased hip external rotation and knee extension moment across both legs in session one (Figure 22). While Nadeau *et al.* (1997) reported reduced knee external moment for PFP patients, the values seen in Figure 22 fall within the reported region of healthy subjects in other studies using OpenSim (Trinler and Baker, 2017). The increase in

knee and hip rotation might also be partially explained by the offset in knee angle kinematics discussed in the Inverse Kinematics and shown in Figure 19.

Besier *et al.* (2009) reported on the knee flexion-extension moment in stance phase for PFP subjects, and Nadeau *et al.* (1997) reported on the knee flexion-extension, ankle dorsiflexion-plantarflexion and hip flexion-extension moments for the full gait cycle. The knee flexion moment results from this project are comparable to Besier *et al.* (2009), which shows an initial extension moment and then a flexion moment of about 0.8Nm/Kg. Nadeau *et al.* (1997) show a reduced knee flexion moment and an increased extension moment compared to the results shown in this study. The ankle moment shown in Nadeau *et al.* (1997) is comparable to the results shown in this study, with a small initial dorsiflexion moment, followed by a sizeable plantarflexion moment of around 1.5 Nm/Kg. The hip flexion-extension moments were equally comparable, with an initial extension moment followed by a significant flexion moment peaking below 1 Nm/Kg.

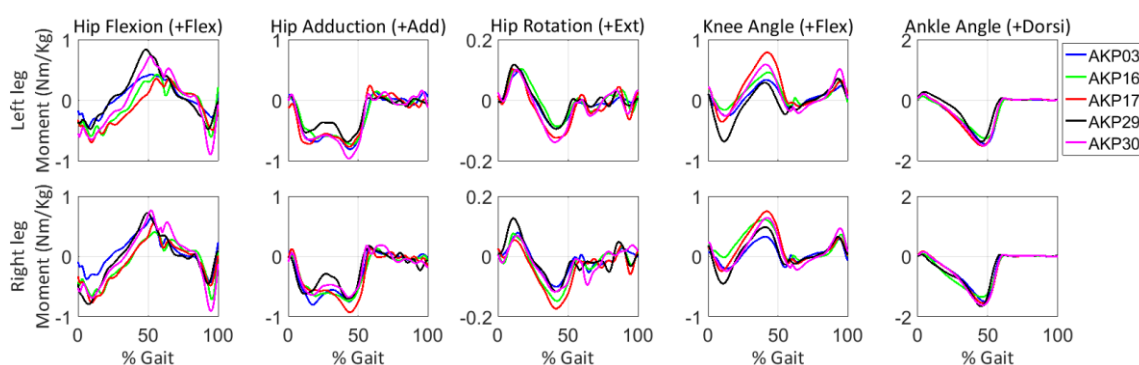


Figure 23: Subject comparison of ID averages for session four

Reporting of the hip adduction moment and hip rotation moment was limited in studies of patellofemoral pain. However, the shape of these results was agreeable with results that were seen for healthy subjects (Trinler and Baker. 2017; Fliger *et al.*, 2016; Lin *et al.*, 2011). With only minor differences seen between knee, ankle and hip flexion moments of healthy and PFP subjects (Besier *et al.*, 2009; Nadeau *et al.*, 1997) it is fair to assume that the hip adduction and hip rotation moments can be compared against healthy subjects for the general shape. Figure 24 shows the comparison of the ID results between the first and final session for AKP 16.

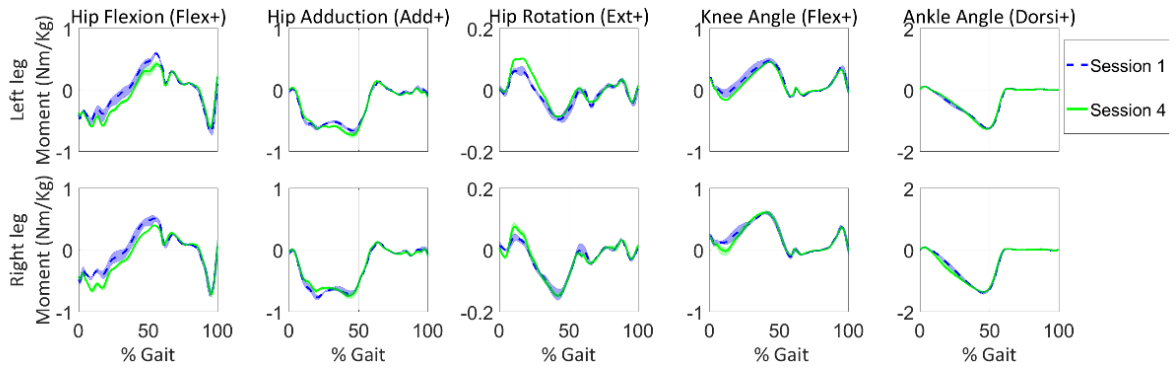


Figure 24: Session comparison of the ID for subject AKP 16

The same figures for the remaining subjects are shown in Figure 51 to Figure 54 of Appendix B.2. Inverse Dynamics. The shaded region displays the maximum and minimum result for the trials on that particular leg. The figures show high repeatability between the trials in both sessions of every subject. There are also no significant changes across the subjects. The most significant change appears in the knee moment of subject AKP 29 on the unaffected (right) leg, with a decrease in the extension moment and an increase in the flexion moment during stance, as shown in Figure 53 of Appendix B.2. Inverse Dynamics. Subject AKP 16 shows a reduced knee flexion moment during early stance phase in session one on the affected (right) leg, shown in Figure 24. This stems from the kinematics of the subject discussed above and shown in Figure 21. Session four does not show the same problem. Table 12 shows the COD for the inter-session comparison of every subject. The table shows a high average repeatability between sessions ($R^2 = 0.93 \pm 0.05$), with the lowest COD value equal to 0.74 indicating high repeatability.

Table 12: Inter-session coefficient of determination values for ID

Joint moment	AKP 03 (R^2)		AKP 16 (R^2)		AKP 17 (R^2)		AKP 29 (R^2)		AKP 30 (R^2)	
	Left	Right								
Hip Flexion	(0.90)	(0.98)	(0.92)	(0.90)	(0.80)	(0.92)	(0.93)	(0.94)	(0.93)	(0.95)
Hip Adduction	(0.98)	(0.98)	(0.98)	(0.98)	(0.94)	(0.95)	(0.94)	(0.93)	(0.94)	(0.88)
Hip Rotation	(0.90)	(0.96)	(0.92)	(0.92)	(0.84)	(0.88)	(0.83)	(0.85)	(0.91)	(0.91)
Knee Angle	(0.87)	(0.96)	(0.96)	(0.92)	(0.86)	(0.89)	(0.94)	(0.74)	(0.91)	(0.92)
Ankle Angle	(0.99)	(0.99)	(0.99)	(0.98)	(0.98)	(0.98)	(0.97)	(0.98)	(0.98)	(0.99)

5.8.4. Residual Reduction Algorithm

The OpenSim user manual (Delp *et al.*, 2007) describes threshold values for RRA residuals as “good”, “okay” or “bad”. These residuals are listed for the generic subject of mass 75kg. The results have been presented as a percentage of Body Weight (%BW). “Good” residuals are listed from 0 – 10 N (0 – 1.36 %BW) and 0 – 50

Nm (0 – 6.8 %BW) for force residuals and moment residuals respectively. “Okay,” residuals are between 10 – 25 N (1.36 – 3.4%BW) and 50 – 75 Nm (6.8 – 10.2 %BW) for force residuals and moment residuals respectively. Residuals that are greater than the previously mentioned residuals are described as “bad” (Delp *et al.*, 2007). Table 13 shows the maximum errors for the residuals which account for each degree of freedom between the model pelvis and the ground.

Table 13: RRA maximum residual forces

Residual (%BW)	AKP 03		AKP 16		AKP 17		AKP 29		AKP 30	
	1	4	1	4	1	4	1	4	1	4
F_X	1.15	0.75	1.09	0.94	0.65	0.68	1.28	1.93	0.74	0.6
F_Y	2	2.07	1.82	3.15	2.23	2.81	2.70	2.61	1.89	1.52
F_Z	0.57	0.67	0.93	0.47	0.68	1	1.63	0.83	0.47	0.39
M_X	6	5.07	4.95	5.59	3.6	3.96	5.37	5.69	5.4	6.49
M_Y	1.72	1.23	1.96	1.37	2.7	3.73	3.83	4.19	1.72	1.79
M_Z	6	5.07	4.95	5.59	3.6	3.96	5.37	5.69	5.4	6.49
	“Good”				“Okay”				“Bad”	

Table 13 shows the maximum residuals for each subject during session one and session four. Typically, force residuals were highest in the Y direction (vertical) as this is where the most significant mismatch between forces occurs. The most substantial forces occur in the Y direction, so it is apparent that this is where the most significant mismatch between forces and kinematics will occur. The F_Y residuals are still all within the “okay” range. The rest of the force residuals are all in the good range, except for AKP 29, which has an “okay” F_Z and F_X residual in session one and four respectively. Every moment residual is in the good range. The kinematics of RRA are shown alongside the kinematics output by CMC and IK in the Computed Muscle Control section of the OpenSim results.

5.8.5. Force plate and motion data filtering

The filtering of the marker and force plate data significantly influences inverse dynamics. Experimental kinematics have been shown to be dynamically inconsistent with measured force plate data (Kuo, 1998), with the problem exacerbated by processing. Van den Bogert *et al.* (1996) investigated the optimal filtering for inverse dynamics analysis. Data from simulated running movements, with known intersegmental loading, was used to investigate the effect of low-pass filtering on the calculation of intersegmental loading. A two-dimensional musculoskeletal model with four rigid segments was used in the simulation. Van den Bogert *et al.* (1996) found that when unfiltered data, captured at high sampling

rates were used, Inverse dynamics results were identical to known intersegmental loads.

Capturing and recording at such high sample rates is not possible in practice due to the presence of noise and the computational cost of using such high sampling rates. It was then found that when using realistic sampling rates with real noise, the results were susceptible to the filtering procedure. The errors occur mainly at the impact point and are therefore not related to noise in the data. It is proposed that these errors are caused by the removal of high-frequency components of segment acceleration. Some high horizontal GRF impact peaks are then left unaccounted for. It then advised that markers and forces should be filtered at the same frequency, removing inconsistencies between the two inputs.

Kristianslund *et al.* (2012) performed a similar study. They investigated the effects of low-pass filtering on data obtained from trials involving 123 elite handball players performing sidestep cutting. This study was particularly significant because it had a large sample size and because it investigated the effects in both the sagittal and frontal plane. Similar results to those in Van den Bogart *et al.* (1996) were found. Evident impact artefacts were found when using different cut-off frequencies to process force and marker data. It is advised that once a suitable frequency has been chosen to filter marker data, that frequency should be applied to the force plate data.

Roewer *et al.* (2012), Bisseling *et al.* (2006) and Bezodis *et al.* (2012) all investigated the effects of filtering marker and force plate data on inverse dynamics results for high impact activities. The results agreed with those produced by van den Bogart *et al.* (1996) and Kristianslund *et al.* (2012). These studies propose filtering the marker data and the force data at the same frequency and conclude that peaks that occur shortly after impact are in fact artefacts. These studies investigated high impact activities like jumping and sprinting, for which there would be more high-frequency components. While the impact on walking may be less severe, it is valuable to investigate the effects.

The residual reduction algorithm offers a novel method for investigating the effects of marker and force plate data processing. As mentioned above, the residual forces calculated by RRA account for modelling and processing errors as well as non-real elements between the model and the ground. Therefore the mismatch between the marker data and the force plate data should be visible in an increase in the residuals that accounts directly for such problems. By comparing the residual forces across different frequencies as well as the inverse dynamics results, insight can be gained on the filtering effects of a relatively low impact activity like walking.

The raw marker data were filtered at five different frequency combinations to compare the effects and to investigate if similar trends can be seen to those found

in the literature discussed above. The difference being that the data being compared here is a relatively low impact activity. The introduction of residual force comparison is also a novel approach. Table 14 shows the different frequency combinations that were used to filter the marker data and the force plate data respectively. As described in Data processing, the filtering was done with a zero-lag second-order low-pass Butterworth filter.

Table 14: Force plate and marker low-pass cut-off frequencies

No.	Marker cut off frequency (Hz)	FP cut-off frequency (Hz)
1	6	30
2	10	10
3	10	15
4	15	15
5	15	50

Figure 25 shows subject AKP 29's session one left and right knee moments, as well as the vertical residuals for the average of the left and right trials, for the different force plate and marker filtering frequencies. Figure 27 shows the same results for subject AKP 03. These figures contain the results on the foot opposite to the foot which is going through the gait cycle. The purpose of this is to show foot strike at the 80% point of stance phase (50% of the gait cycle), rather than at the beginning of the figure where the point of interest is broken up by the y-axis of the figure.

The bold lines contain the data which was filtered at the same frequency, and the plain lines contain the data filtered at different frequencies. In the interest of space, the figures for every subject during both sessions have been placed Appendix B.3.

Force plate and EMG processing. The two figures contain the ‘best’ and ‘worst’ results based on the hypothesis detailed above.

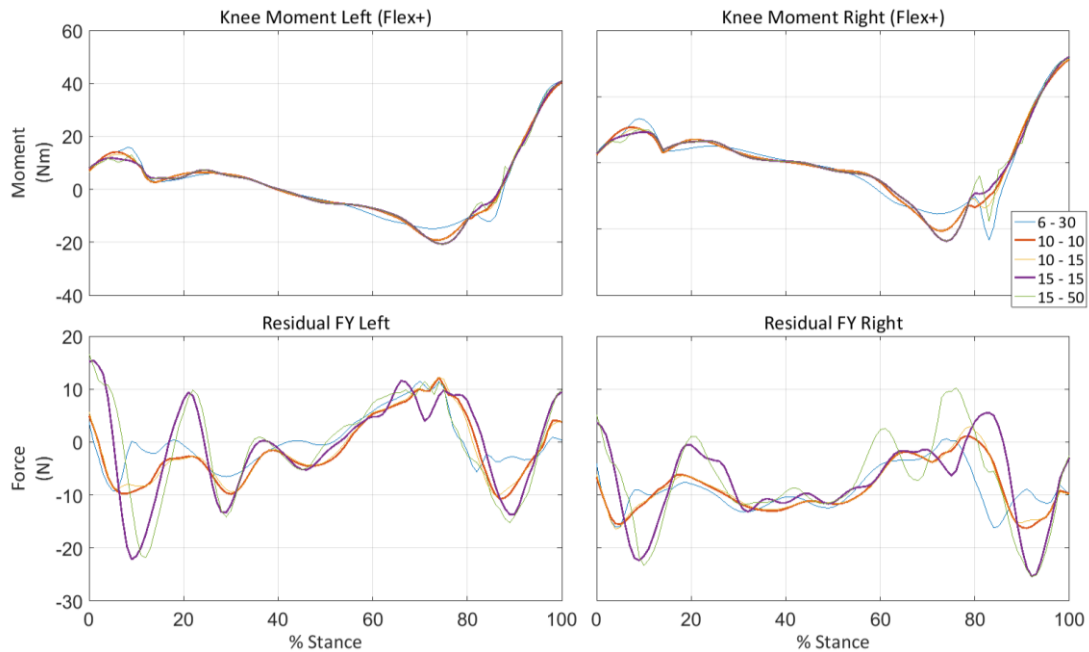


Figure 25: Knee moment and FY residual of AKP 29 Session one

In the right knee moments of Figure 25, the data which was filtered at different frequencies has a more prominent spike at 80% when compared to the data filtered at the same frequency. The most significant spike is in the 6 – 30 Hz filtering frequency (plain blue line), followed by the 15 – 50 Hz (plain green line), and then a small spike in the 10 – 15 Hz (plain yellow line). Both bold lines contain significantly smaller, but still visible upward spikes, with no downward spike. The left knee moments in Figure 25 show almost no disturbance at around 80% of stance phase. However, there is a small downward spike in the 6 – 30 Hz cut-off frequencies line. Between all the subjects this is the case with the least evidence of an artefact at foot strike. Figure 26 and Figure 28 shows the Bland and Altman. (1999) plot of the data shown in Figure 25 and Figure 27 respectively. The data are plotted with the colours matching those used in Table 14. The 10 – 10 Hz frequency is used to compare against the remaining frequency combinations. The number assigned to each data point is equal to the percentage of stance phase of that point.

Figure 26 shows a mean on zero, indicating that on average the processing methods produce the same results as the 10 – 10 Hz. The points furthest from the mean line indicate the positions at which the data strayed furthest from the 10 – 10 Hz value. It is clear that the 6 – 30 Hz (blue) and 15 – 50 Hz (green) data strays furthest from the mean at around 80 percent of stance phase, which is the point of impact.

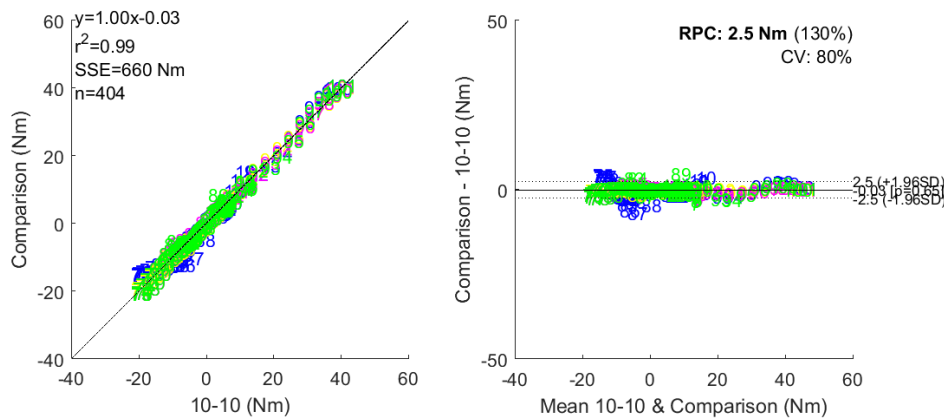


Figure 26: Bland and Altman plot for AKP 29 left knee moment during session one

Figure 27 shows the most significant evidence of peaks around foot strike, particularly for the right knee moment. In the data filtered at different frequencies there are three peaks: an upwards peak at 80%, followed by a sharp and significant downwards peak, followed again by an upwards peak. The data filtered at the same frequency (the bold lines), also has the initial upwards peak, with far less noteworthy peaks after the initial peak.

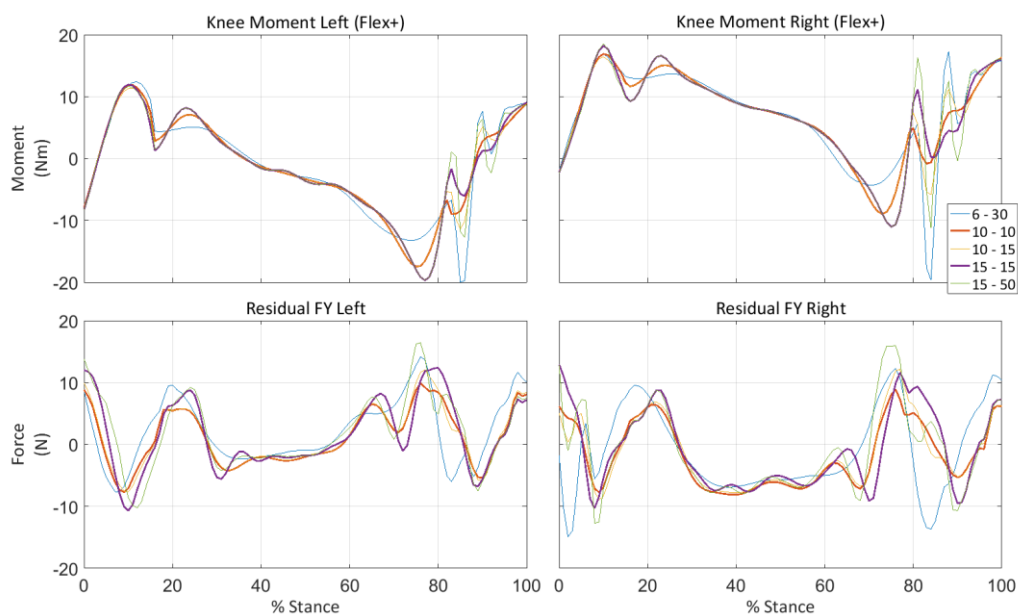


Figure 27: Knee moment and FY residual AKP 03 Session one

The most significant finding is that the data filtered at 10 – 15 cut-off frequencies (the yellow line) has far more significant peaks than the data filtered at the 15 – 15 Hz frequency (purple line), despite the higher filtering frequency of the force plate data. Figure 28 shows the Bland and Altman plot for the data displayed on the top right of Figure 27. Again, the mean of all of the processing methods is on zero,

indicating that the processing techniques produce the same result on average. It is visible from this figure that the 6 – 30 Hz (blue) data and the 15 – 50 Hz (green) show the highest deviation from the 10 – 10 Hz value, particularly between 80 and 90 percent of stance phase. This supports the hypothesis that the data filtered at different frequencies introduces artefacts at foot strike.

Figure 28 shows the 15 – 15 Hz data with a few points (82 and 83 percent of stance phase) showing a significant difference to the 10 – 10 Hz data, however, from Figure 27 it is clear that at this point (83 percent stance phase), both the 10 – 10 Hz data and the 15 – 15 Hz data have an upwards peak, with the 15 – 15 Hz upwards peak being more significant. The marker filtering also appears to introduce a slight phase shift in the knee moment; this is mainly visible between 60 and 80 percent of stance phase in Figure 27. This phase shift is also partly responsible for the 15 – 15 Hz (purple) data appearing to stray further from the 10 – 10 Hz data when compared to the 10 – 15 Hz (yellow) data in Figure 28.

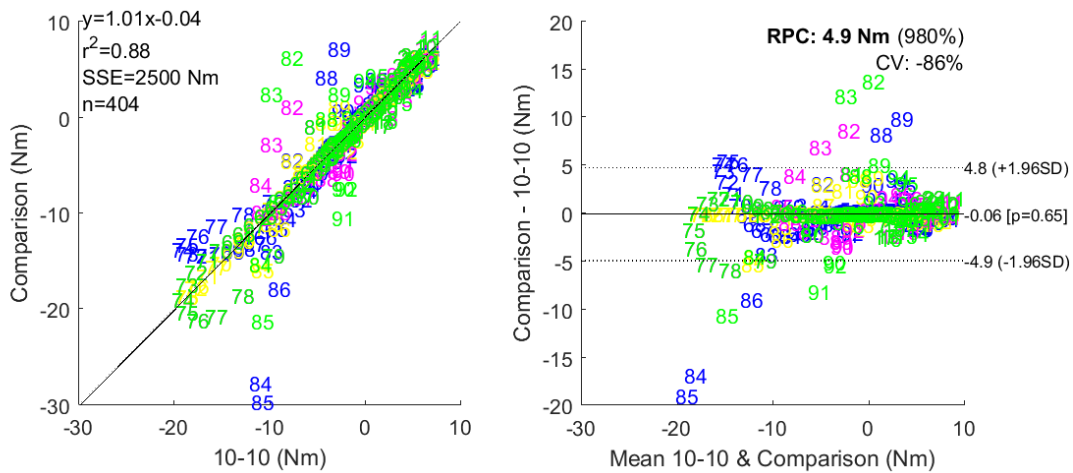


Figure 28: Bland and Altman plot for AKP 03 right knee moment during session one

The hypothesis that the mismatch would be visible in the residual values is not observed. The residual value appears to be more dependant on the force plate filtering with little dependency on the marker filtering. The residual values remain within acceptable levels, so the majority of the residual forces can be attributed to the expected dynamic inconsistencies within the model, with the inconsistencies due to processing challenging to isolate.

5.8.6. Computed Muscle Control

The residuals produced by CMC are evaluated in the same way as in Residual Reduction Algorithm with the description provided by the OpenSim user manual (Delp *et al.*, 2007). Table 15 shows the maximum residual values output by CMC.

Six residual force values fell within the “bad” range as defined by Delp *et al.* (2007). The worst was the F_X residual of subject AKP 30, which was less than one percent of body weight above the prescribed “okay” value. The rest of the force residuals fell within the “okay” range except for the F_Y residual of both sessions for AKP 30. The moment residuals all fell within the “good” range except for the M_Y residual for session one of subject AKP 16, which fell in the middle of the “okay” range.

Table 15: CMC Residuals

Residual (%BW)	AKP 03		AKP 16		AKP 17		AKP 29		AKP 30	
	1	4	1	4	1	4	1	4	1	4
F_X	2.81	2.87	2.47	2.39	3.14	2.79	3.1	3.49	3.06	4.32
F_Y	3.23	3.61	1.96	1.83	2.91	2.16	2.14	2.46	0.82	0.98
F_Z	3.48	2.66	2.71	1.81	2.62	3.53	3.14	3.68	3.1	2.42
M_X	1.95	1.49	1.61	1.63	1.88	2.25	2.69	3.19	2	2.14
M_Y	6.44	5.74	8.38	5.65	5.02	4.75	6.65	7.06	6.59	5.69
M_Z	0	0	0	0	0	0.3	0	0	0.28	0
	“Good”				“Okay”				“bad”	

Table 16 shows the reserve torque values produced during CMC. As discussed in Chapter 5.6 the reserve actuators are augmented to the model to account for strength deficiencies in the muscles. Delp *et al.* (2007) describe “good” threshold values between 0 – 25 Nm, “okay” threshold values between 25 – 50 Nm and “bad” threshold values between 50 – 75 Nm. These values should also be low relative the torque produced by the primary muscle.

Table 16: CMC Reserves

Reserve (Nm)	AKP 03		AKP 16		AKP 17		AKP 29		AKP 30	
	1	4	1	4	1	4	1	4	1	4
Ankle	15.7	23.2	15.4	34.1	7.6	16.9	19.4	21.3	18.7	15.4
Knee	0	0	0	0	0	0	0	0	0	0

Hip	3.2	0.2	0.8	0	2.3	4.1	3.2	6.6	2.8	0.1	
Lumbar	0	0	0	0	0	0	0	0	0	0	
mtp	2	2.2	2.2	2.3	3.7	3.1	2.5	2	1.7	1.9	
Subtalar	6.8	3.2	2.7	3.7	10.6	7.2	6.2	6.4	3.8	2.9	
	“Good”				“Okay”			“Bad”			

Only session four of subject AKP 16 had a reserve torque outside of the “good” range, which fell within the “okay” range (shown in Table 16). The ankle reserve torque for subject AKP 16 is 10 Nm outside of the “good” range.

Figure 29 shows the resultant right and left knee and ankle angle for session one of subject AKP 17 from IK, RRA and CMC. The results for session four are shown in Figure 30, the results for the remaining subjects can be found in Appendix B.4. Kinematics comparison. Through stance phase (up to 60% of gait) all the resultant kinematics track each other accurately, except for the ankle angle in early stance, where RRA shows a decreased gradient. The most significant change in the kinematics is the change in the RRA kinematics during the swing phase of both the ankle and the knee. As described in Chapter 5.5, the RRA adjusts the kinematics to satisfy a control problem. It is hypothesised that the adjustment made in swing phase occurs to balance the mass centre of the model to maintain the model in a more upright position.

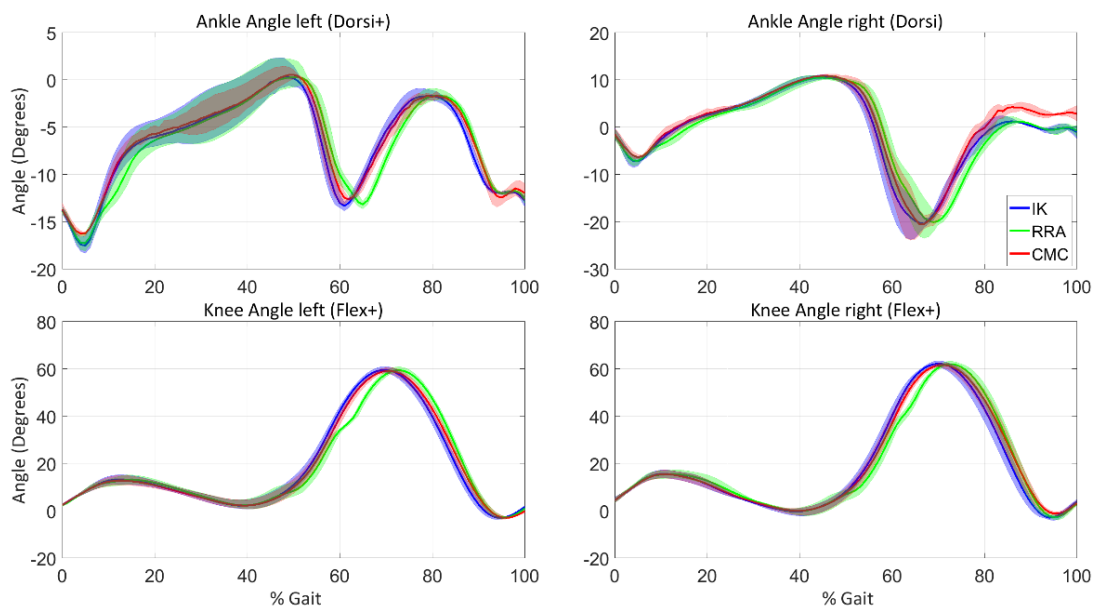


Figure 29: AKP 17 Session one kinematics comparison

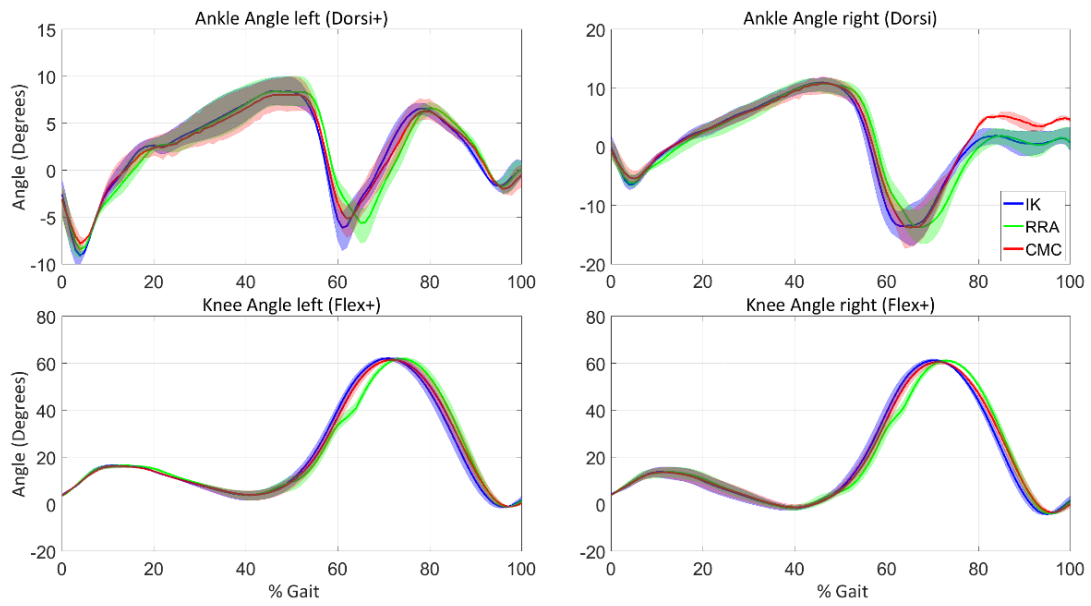


Figure 30: AKP 17 Session four kinematics comparison

The resultant kinematics from RRA are fed into CMC, as well as the adjusted model produced by RRA. Despite the CMC set to track the RRA kinematics, the result follows the result of IK more closely.

6. EMG Informed Neuromusculoskeletal modelling software

Calibrated EMG Informed Neuromusculoskeletal modelling software (CEINMS) uses calculated joint moments, muscle parameters, and experimentally recorded EMG results to determine the neural drive and the instantaneous kinematics and forces of the musculotendon units. CEINMS also uses an optimisation-based calibration procedure to produce a subject-specific file that contains musculotendon parameters that differ non-linearly between subjects.

6.1. Neuromusculoskeletal models

CEINMS provides models which fall into two categories: Activation dynamics, which characterises the conversion from muscle excitation to muscle activation, shown in Figure 31. Activation dynamics can be broken down further into two stages, muscle excitation to neural activation, and neural activation to muscle activation. The other parameter category is contraction dynamics, which characterise the conversion from muscle activation and musculotendon kinematics to musculotendon forces.

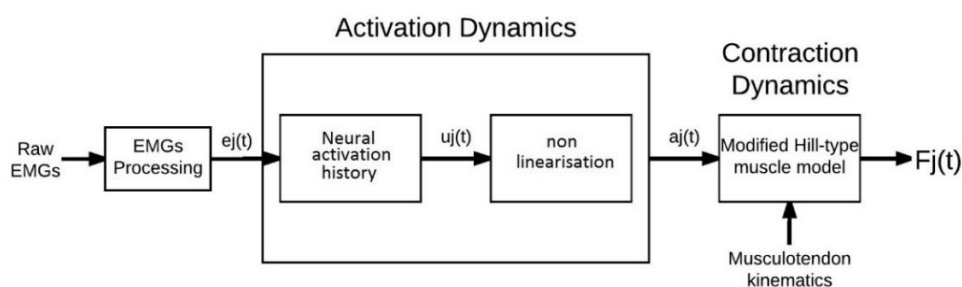


Figure 31: Flow diagram showing the relationship between EMGs, Activation Dynamics and Contraction Dynamics (Ceseraciu *et al.*, 2015)

6.1.1. Activation dynamics

Muscle excitation signals obtained from the experimental EMGs are used to derive the neural activation by modelling the muscle's twitch response (Lloyd *et al.*, 2008). Equation (13) describes the discrete form of the critically damped linear second-order differential (Milner-Brown *et al.*, 1973) system that represents the derivation of the neural activation from the muscle excitation.

$$u_j(t) = \alpha e_j(t - d) - \beta_1 u_j(t - 1) - \beta_2 u_j(t - 2) \quad (13)$$

Where $e_j(t)$ is the j -th muscle excitation at time t , $u_j(t)$ is the neural activation, α is the muscle gain coefficient, β_1 and β_2 are the recursive coefficients, and d is the

electromechanical delay. The muscle excitation signals $e(t)$ are extracted from the experimental EMG signals. The subject-specific parameters C_1 and C_2 relate to the recursive coefficients as follows:

$$\beta_1 = C_1 + C_2 \quad (14)$$

$$\beta_2 = C_1 \cdot C_2 \quad (15)$$

where:

$$|C_1| < 1 \quad (16)$$

$$|C_2| < 1 \quad (17)$$

and

$$\alpha - \beta_1 - \beta_2 = 1 \quad (18)$$

Equation (14) to equation (18) describes the constraints on the critically damped second-order differential system used to derive neural activation from muscle excitations (Buchanan et al. 2004). Neural activation can then be used to derive the muscle activation through one of two non-linear solutions. The first, introduced by Lloyd and Besier, (2003), is as follows:

$$a_j(t) = \frac{e^{A_j u_j(t)} - 1}{e^{A_j} - 1} \quad (19)$$

where $a_j(t)$ is the j -th activation of the muscle and A_j is the non-linear shape factor, which is constrained between the interval $(-3,0)$. The second model was introduced by Manal and Buchanan, (2003) with the derivation of muscle activations from neural activations as a piecewise parametric function:

$$a_j(t) = a_j^{act} \ln(\beta_j^{act} u_j(t) + 1), \quad 0 \leq u_j(t) \leq u_0 \quad (20)$$

$$a_j(t) = m_j u_j(t) + c_j, \quad u_0 \leq u_j(t) \leq 1 \quad (21)$$

for each muscle j , the parameters introduced in equation (20) and (21) are only dependant on the shape factor A_j constrained in the interval $(0,0.12]$.

6.1.2. Contraction dynamics

The muscle activation calculated above in Activation dynamics, combined with the musculotendon kinematics act as inputs to a modified Hill-type muscle model, which consist of active and passive force generating components in series. The

active component is the muscle fibres, and the passive component is the tendon. The following formula, therefore, represents the force produced by the musculotendon unit:

$$F^{mt} = F^t = F^{max} [f_a(\tilde{l}_m) \cdot f_v(\tilde{v}_m) \cdot a + f_p(\tilde{l}_m) + d_m \cdot \tilde{v}_m] \cdot \cos \varphi \quad (22)$$

where F^t is the tendon force, a is the muscle activation calculated above, d_m is the muscle mapping element, and φ is the pennation angle of the fibres. The pennation angle is the angle at which the muscle fibres are slanted relative to the tendon fibres.

The force in equation (22) is dependent on three primary factors: $f_a(\tilde{l}_m)$ which expresses the active force at different fibre lengths. $f_v(\tilde{v}_m)$, which accounts for the force contribution of the fibres contraction velocity and $f_p(\tilde{l}_m)$, which represents the passive force-length relation or the fibres response to strain. These three relationships are represented in Figure 32. The force in Figure 32 is normalised by the maximum isometric muscle force (F^{max}). The muscle fibre length is normalised by the optimal fibre length (L_m^0), and the muscle fibre velocity is normalised by the maximum muscle contraction velocity (v^{max}). The optimal fibre length decreases as the activation increases (Huijing, 1996) which is shown in Figure 32 by the different levels of activation.

Equation (23) shows the pennation angle, φ , as a function of the instantaneous fibre length l_m :

$$\varphi = \sin^{-1} \left(\frac{L_m^0 \sin \varphi_0}{l_m} \right) \quad (23)$$

where φ_0 is the pennation angle of the fibres at their optimal length. The estimation of the fibre length is influenced by the tendon element as follows:

$$l_m = \frac{l_{mt} - l_t}{\cos \varphi} \quad (24)$$

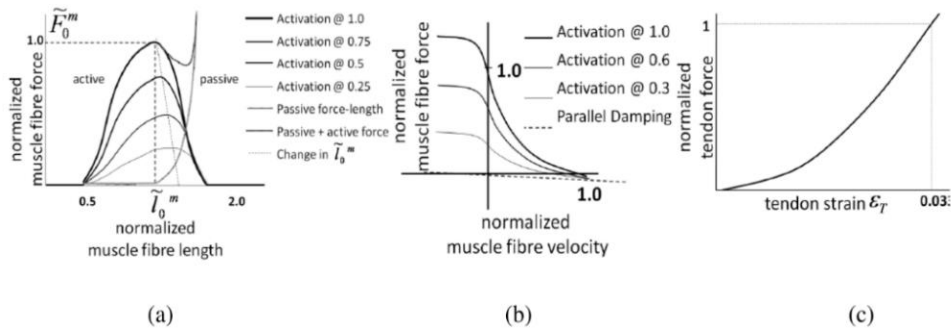


Figure 32: Active and passive force-length curves (Thelen. 2003)

Three different tendon models can be used in CEINMS to estimate muscle-tendon unit forces. The integration elastic tendon (IET) model forward integrates the muscle fibre velocity to calculate the muscle fibre length. The initial value for the fibre velocity, v^m , is estimated through an optimisation routine which distributes the velocity contribution between the fibres and the tendon. The velocity is then integrated using a Runga-Kutta-Fehlberg to calculate the instantaneous fibre length, l_m . With the fibre length, the tendon length, l_t , can be calculated using equation (24) after which the tendon strain can be calculated as follows:

$$\epsilon = \frac{l_t - l_{ts}}{l_t} \quad (25)$$

where l_{ts} is the tendon slack length. The tendon force F^t is then calculated using the force strain relationship of the tendon shown in Figure 32 (c). The tendon force and the known activation can then be used to calculate the active and passive elements of the force, which can in turn be used to calculate the fibre velocity, v^m , by inverting the force velocity function, $f_v(\tilde{v}_m)$, shown in Figure 32 (b). The fibre velocity value is then used as the initial value in the next integration step. This method relies on the numerical integration of the stiff MTU equations which minimises the robustness of the solution.

A different tendon model, which does not rely on forward integration is the equilibrium elastic tendon (EET) model. This model uses a Van Wijngaarden-Dekker-Brent optimisation routine to find the root of the following equation:

$$F^{mt}(\tilde{l}_m) = F^t(\tilde{l}_m) \quad (26)$$

where $F^t(\tilde{l}_m)$ is calculated from the tendon force-strain relation by manipulating equation (23), (24) and (25) to express tendon strain, ϵ , as a function of the fibre length, \tilde{l}_m . Subsequently $F^{mt}(\tilde{l}_m)$ is obtained from equation (22) by calculating the fibre velocity, \tilde{v}_m , as the derivative of the fibre length, \tilde{l}_m . This method is more robust and guarantees a solution of the fibre length. The final tendon model, the stiff tendon (ST), simplifies the tendon to reduce computation time. The tendon is modelled as an element of infinite stiffness with the tendon length set equal to the slack length.

6.2. Calibration and Execution

The calibration process aims to determine the subject-specific characteristics of a set of parameters for each musculotendon unit described above in the Neuromusculoskeletal models. This model will match the subject's musculotendon physiology, activation and contraction dynamics allowing for more accurate force calculations.

Parameters change non-linearly between subjects. Therefore an optimisation algorithm is used to adjust the parameters so that close tracking of the experimental joint moments and EMG excitations is achieved. The algorithm minimises an objective function ultimately outputting calibrated parameters as shown in Figure 33. The calibrated parameters, along with the inputs (outputs from CEINMS) and the proper setup and configuration files are input into the execution procedure to produce the results shown in Figure 34.

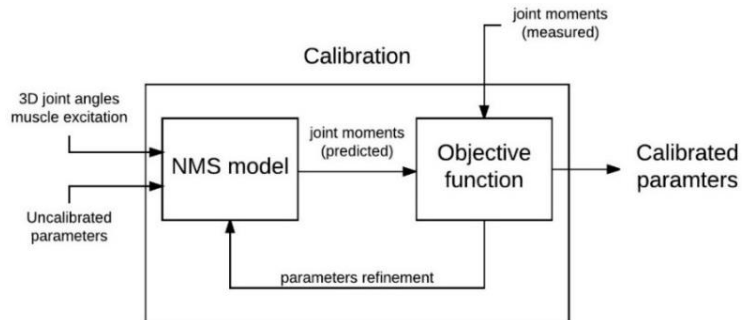


Figure 33: Flow diagram of the calibration procedure

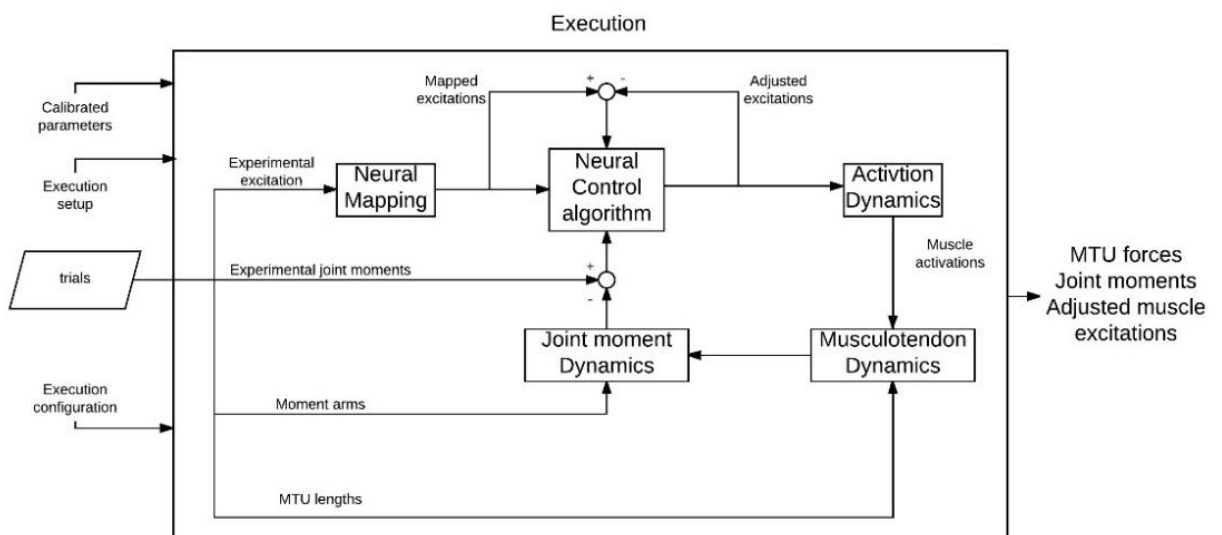


Figure 34: Flow diagram of execution procedure

During calibration, the parameters are required to remain within a prescribed range that maintains realistic physiological characteristics. These parameters are set in an initial prescribed subject file and are listed and described in Table 17.

Table 17: Musculotendon Default values and changes

Parameter	Default Value	Calibration change
C_1	-0.75	Subject specific, remain across MTUs
C_2	-0.75	Subject-specific, remain across MTUs
A_j	0.5	Subject-specific, remain across MTUs
L_m^o	Per muscle	Subject-specific, remain for the right and left leg of each MTU
φ_o	0	Subject-specific, remain for the right and left leg of each MTU
l_{ts}	Per muscle	Subject-specific values for each MTU
v_m	10	Remains as default value
F_m^o	Per muscle	Subject-specific values for each MTU

6.2.1. Calibration optimisation algorithm

The optimisation algorithm used in the CEINMS calibration procedure is simulated annealing formulated by Goffe *et al.* (1994) and Corana *et al.* (1987). The detailed outline of the generic algorithm is provided in Appendix C. Simulated Annealing. The objective function that is minimised in the algorithm is as follows (Pizzolato *et al.*, 2015):

$$f_{cal} = \sum_t^{N_{trials}} \sum_d^{N_{DOFs}} E_{t,d} \quad (27)$$

$$E_{t,d} = \frac{1}{N_r} \sum_r^{N_{rows}} \left(\frac{(\overline{M_{t,d,r}} - M_{t,d,r})^2}{var(\overline{M_{t,d}})} + p_r \right) \quad (28)$$

$$p_r = \sum_j^{N_{MTUs}} P(r,j) \quad (29)$$

$$P(r,j) = 100(\tilde{l}_{mr,j} - 1)^2, \text{ if } |\tilde{l}_{mr,j} - 1| > 0.5 \quad (30)$$

where $M_{t,d,r}$ represents the predicted joint moments and $\overline{M_{t,d,r}}$ represents the experimental joint moments. The sum of the squared differences are normalised by the trial variance and the number of data points for each t th trial, as shown in equation (28). This is done to reduce the length and magnitude differences between trials (Pizzolato *et al.*, 2015). The penalty function, $P(r,j)$, shown in

equation (30) discourages non-physiological solutions by maintaining the values of the muscle fibre length, $\tilde{l}_{mr,j}$, within in operative range.

6.2.2. Running Calibration and Execution

A tool to automatically run the CEINMS software with no user intervention was created to satisfy the objective of extending the automated modelling pipeline. The tool was able to cycle through the subject results output by OpenSim, and if the required input data to CEINMS was available, create the necessary settings file and run both calibration and execution. This required the uniform file, and file directory naming conventions to be used throughout OpenSim. Figure 35 contains a flow diagram detailing the required input data and settings files to both the calibration and execution steps of CEINMS. Figure 133 to Figure 135 in Appendix G.3. CEINMS contain detailed flow diagrams of CEINMS.

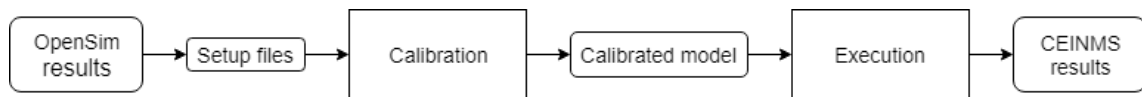


Figure 35: Calibrated EMG Informed Neuromusculoskeletal modelling flow diagram

❖ Calibration setup

The setup file required to run the Calibration procedure contains the paths to three files, one containing the details of the generic subject, one containing the excitation generators, and one detailing the calibration configuration, as shown in Figure 35. The setup file also details the output path of the calibrated file that will be produced by the Calibration step.

❖ Uncalibrated Subject

The generic subject file is the uncalibrated file before it has undergone any parameter adjustment. It lists all the muscles in the model, with their parameters. It also lists the DOF that each muscle contributes to. It also details the MTU curves shown in Figure 32. The tool automatically loads the generic subject file, and links it to the relevant subject-specific OpenSim files after which it pulls the relevant parameters from the OpenSim file; namely the optimal fibre length, the pennation angle at the optimal length, the tendon slack length and the maximum isometric force. The rest of the parameters are left in their default state, as listed in Table 17.

❖ Excitation generators

The excitation generators file contains the excitations mapping for each muscle in the neuromusculoskeletal (NMS) model. In this case, there was a one to one

mapping, so the file essentially mapped the EMG input signals to the relevant muscles. This is a generic file that can be used for every subject without the need for editing.

❖ Calibration configuration

The calibration configuration file contains all the details required to run the procedure. This includes the description of the optimisation algorithm. For this project, these values were unchanged from their default value shown at the end of Annealing. The NMS model is detailed regarding operation mode, tendon model and excitation to activation relationship. These settings remained the same across all of the subject calibrations and were set as follows: the open loop EMG driven mode was chosen, the equilibrium elastic tendon model was used, and an exponential excitation to activation relation was chosen.

The configuration file then contains the steps detailing the calibration tasks. The DOF considered for calibration are listed, which in this case were left and right ankle and left and right knee. The target function to minimise was set as the torque error. MTU parameter ranges are detailed for some of the parameters. The range for the constraints parameters c_1 and c_2 are set as $[-0.95 - 0.05]$. The shape factor range is set as $[-2.999 - 0.001]$. Finally the tendon slack length and the optimal fibre length are limited to $[0.95 - 1.05]$. Muscles are also grouped if they contain the same parameters.

To calibrate the subject-specific NMS model, a set of calibration trials need to be listed for the optimisation algorithm to track. These calibration sets should be separate to those used in the execution step. As described in the Experimental procedure the subjects performed walking trials until three successful trials were completed on each leg. Therefore, the trials that were performed with the non-symptomatic leg striking force plate one were used to adjust the parameters for the calibrated subject file used to execute the symptomatic leg trials. The trials with symptomatic leg striking force plate one were then used to calibrate the subject parameters used in the calibrated file finally used in the execution of the non-symptomatic leg trials. The trial numbers are detailed below in Table 18. The trials highlighted in grey are the symptomatic leg trials.

Table 18: Trials used for Calibration and Execution of CEINMS

Subject	Session	Right Leg Walk	Left Leg Walk
AKP 03	1	1,3,5	2,4,6
	4	3,5	1,2,4
AKP 16	1	1,2,4	3,5,6
	4	1,3,6	4,5
AKP 17	1	1,2,3	4,5,6
	4	3,4,7	2,5,6
AKP 29	1	1,2,3	4,5,6
	4	1,3,5	2,4,6
AKP 30	1	1,2,3	4,5,6
	4	1,2,3	4,5,6

The final detail in the configuration file is the data descriptions (described below) for the trial set used for that calibration procedure. The trials used for calibration are listed by the user for every subject and session before the automated tool is run so that it can run interrupted. These settings and input files can be seen in context in the flow diagrams shown in Figure 133 to Figure 135 of Appendix G.3. CEINMS.

❖ Data description

The OpenSim results which act as inputs to CEINMS are the joint moments from ID, the joint moment arms and muscle lengths and the experimental EMGs extracted during the Data Processing step. These inputs and their path are detailed for each trial in the data description settings file that is automatically created by linking the associated trial names across OpenSim outputs required for CEINMS.

❖ Calibrated subject

The calibrated subject file is the adjusted version of the generic subject file. It is the product of the calibration procedure. This calibrated file becomes the input into the execution procedure.

❖ Execution setup

The setup file for execution contains the paths to four files, one containing the path to the calibrated subject file, one containing the path to the input data file for the trial being executed, one to the excitation generators file which is the same file used in calibration, and finally the execution configuration file. The settings file also contains the directory for the results output by execution.

❖ Execution configuration

The execution configuration file is similar to the one used in the calibration procedure. In this case, the parameter set is excluded because these parameters have now been set. The configuration file only details the NMS details. These details remain the same from the calibration procedure, that is the operation mode remains as an open loop, the tendon model remains the equilibrium elastic model, and the excitation to activation relation is set to exponential.

6.3. EMG processing

While the EMG processing takes place during the Data processing step of the pre-processing, this report places particular emphasis on the processing of EMGs due to its impact on the results of the muscle force estimates. The purpose of EMG processing is to express the raw EMG signal, which is measured in volts, as a representation of the muscle activation expressed as a number between zero and one. The raw signal is also smoothed and filtered to remove noise and signal elements that are not related to the muscle activity.

Processing raw EMGs involves a number of steps which perform different functions. Firstly, the DC offset is removed to centre the data around zero, after which the data are high-pass filtered, full wave rectified, low-pass filtered and then normalised against either maximum voluntary contraction trials, or in trial maximums. During this study, EMG signals were processed at different frequencies to investigate the influence on the muscle activation signal, and ultimately on the muscle force.

6.3.1. Processing techniques in literature

There are a number of techniques for processing raw EMGs in literature, and there is no consensus on the cut-off frequencies for low and high-pass filtering. The user manual for the Calibrated EMG Informed Neuromusculoskeletal modelling software (CEINMS), the software used to estimate muscle forces, recommends filtering the raw EMG signals by first high-pass filtering them using a zero-lag fourth-order recursive Butterworth filter with a cut-off frequency of 30 Hz. Then full-wave rectifying and finally using a Butterworth filter with a low-pass filter at a 6 Hz cut-off frequency.

Besier *et al.* (2009), when using EMGs to calculate knee muscle forces during walking and running in PFP and pain-free subjects, used the same procedure with normalisation using MVCs after low-pass filtering. A similar procedure was followed for Son *et al.* (2010), who used EMG's to estimate muscle forces in real time without three-dimensional motion capture, using a high-pass filter with a cut-off frequency of 20 Hz, full wave rectification, low-pass filtering at a cut-off of 5 Hz and finally

normalisation using MVCs. Schwartz *et al.* (2008), who used surface EMGs to investigate the effect of walking speed on gait, rectified the signal, then filtered with a zero-lag finite impulse response filter at a cut-off frequency of 3 Hz. The resultant signal was then normalised by the peak signal that occurred during the trials.

Buchanan *et al.* (2004) provide an overview of the processing of raw EMGs as part of their paper describing the estimation of muscle forces and joint moments from measurements of neural command. A high-pass filter with a frequency of between 5 and 30 Hz is advised, using a filter that has zero-phase delay properties (a fourth order Butterworth filter is recommended). The resultant signal can then be rectified. It is then recommended that the rectified signal be normalised. The order of EMG processing described in Buchanan *et al.* (2004) differs from the studies above, with the normalisation of the rectified signal proposed before low-pass filtering. Normalisation is advised using MVCs recorded for each muscle separately, however obtaining true maximal values is difficult to achieve. Finally, a low-pass filter with frequencies between 3 and 10 Hz is advised.

Normalisation of EMG data is also a critical step in the determining realistic muscle activation signals (Lehman and McGill, 1999; Devaprakash *et al.*, 2016; Moanton *et al.*, 2015). This is due to the difficulty in obtaining true maximum EMG values. Moanton *et al.* (2015) reported on the effects of normalisation using two different methods. Maximum EMG values were obtained from both MVC trials as well as from the maximum value obtained from a set of collected walking trials. Surface EMG electrodes were used to record the muscle activity of the left leg, and motion data was captured for ten walking trials. OpenSim and CEINMS were then used to calculate muscle forces, and the influence of the two normalisation methods was compared. The results showed a significant difference between the muscle forces calculated using the two different methods. Due to a smaller maximum obtained from the walking trials, a higher muscle activation level is achieved relative to the MVC trials. Moanton *et al.* (2015) suggest that using in trial maximums can lead to unreliable results.

6.3.2. Processing method

The experimental data received from the lab is processed during the Data processing step of the pre-processor. The recommended (Moanton *et al.*, 2015) setting used for EMG processing is as follows: DC offset removal, a band-pass filter between 30 and 300 Hz using a zero-lag second order Butterworth filter, full wave rectification, low-pass filter with a cut-off frequency of 6 Hz and finally normalisation. This step was updated with the band-pass replaced with a high-pass and the raw EMGs processed at a number of cut-off frequencies, for both the high-pass and low-pass filter, to investigate their effect on the resultant muscle excitation signal. The EMG processing procedure is shown in Figure 36.

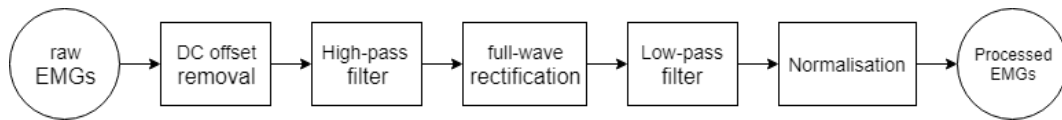


Figure 36: EMG processing flow diagram

The frequencies used were taken from the proposed frequency ranges found in Buchanan *et al.* (2004). The data was normalised from the in trial maximum for each muscle across all the trials in a particular session. The analysis was performed for two subjects, AKP 29 and AKP 30. Table 19 shows the cut-off frequencies of the low-pass and high-pass second order zero-lag Butterworth filters.

Table 19: EMG cut-off frequencies

High-pass cut-off frequency (Hz)	Low-pass cut off frequency (Hz)
10	3
10	6
20	3
20	6
20	10
30	3
30	6
30	10
40	3
40	6
40	10

In addition to the analysis at different frequencies, an analysis of different normalisation techniques was also performed. EMGs, high-pass filtered at 30 Hz and low-pass filtered at 6 Hz, were compared. For each subject, EMGs were normalised by the Walking Trial Maximum (WTM) and then compared to normalisation against a combination of in trial maximums and Maximum Voluntary Contractions (MVC).

6.3.3. Results of EMG processing

The results of the EMG processing are presented. The muscle forces and EMGs for the unaffected leg (right) of subject AKP 29 are shown in this chapter, with the remaining results for the affected leg of session one, and the results of both legs for session one and four in Appendix D.1. EMG processing results, alongside all of the processing results for subject AKP 30. The EMG processing was only performed for subject AKP 30 and AKP 29, due to the computational cost of calibrating a subject-specific model for the resultant EMG of each processing technique.

Figure 37 to Figure 39 in this chapter and Figure 95 to Figure 103 in Appendix D.1. EMG processing results are laid out such that the five muscles displayed on the left of the figure represent the muscles which contribute predominantly to knee flexion-extension, while the three muscles displayed on the right of the figure contribute predominantly to ankle dorsiflexion – plantarflexion. Figure 37 shows the resultant muscle forces and EMGs for EMGs high-pass filtered at 30 Hz and low-pass filtered at 3 Hz, 6 Hz and 10 Hz. It is important to note that the y-axis of the figures is not uniform.

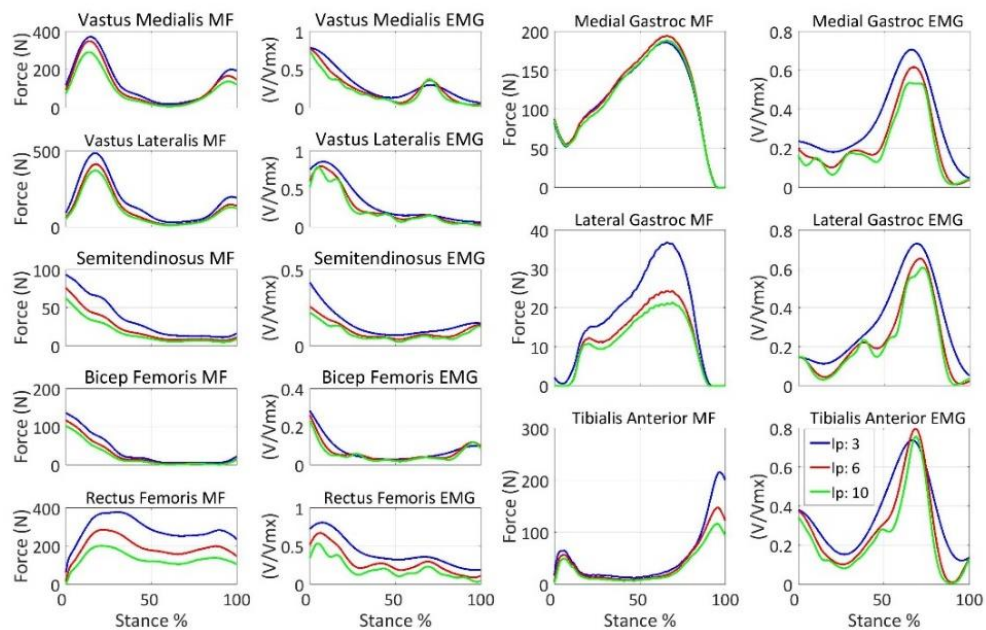


Figure 37: Muscle forces and EMGs of AKP 29 filtered at a high-pass cut-off of 30 Hz for the unaffected leg (right) during session one

Figure 37 shows higher levels of muscle forces when using EMG's low-passed at 3 Hz. This corresponds to higher EMG levels when filtering at 3 Hz. The calibration in CEINMS tunes the model parameters to minimise the error between the external and predicted joint moments. Therefore, muscle forces multiplied by their moment arms will result in similar joint moments. Consequently, it is necessary to look at the resultant muscle forces in their agonist-antagonist groups, rather than purely their relationship to their own EMG. Figure 38 shows the same data as Figure 37, with the high-pass filter cut-off frequency changed to 40 Hz.

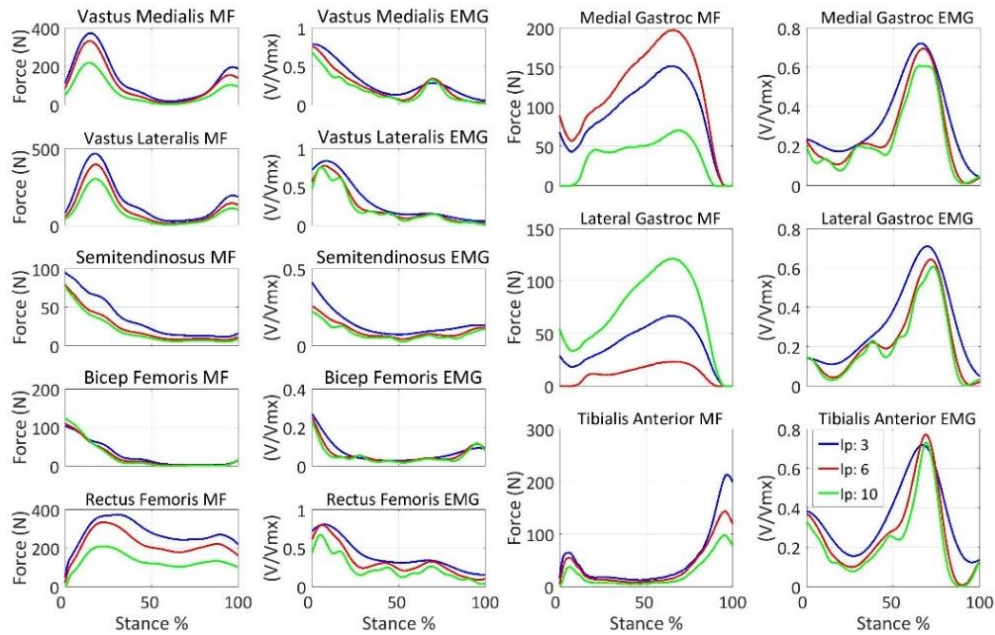


Figure 38: Muscle forces and EMGs of AKP 29 filtered at a high-pass cut-off of 40 Hz for the unaffected leg (right) of session one

The most significant difference seen in Figure 38 is the change in the medial and lateral gastrocnemius muscle forces across different low-pass cut-off frequencies. Particularly when comparing the 6 Hz and 10 Hz cut-off lines (red and green respectively). The 6 Hz cut-off shows a sizeable lateral gastrocnemius force and a relatively smaller medial gastrocnemius force, while the 10 Hz cut-off line shows the opposite, a larger medial gastrocnemius force and relatively smaller lateral gastrocnemius force. The muscles need to be considered in relation to each other rather than purely in relation to their own EMG. The sum of the gastrocnemius remains approximately constant across the different filtering frequencies.

This sensitivity of the medial and lateral gastrocnemius muscle force calculation is observed across most of the EMG processing results. There is no particular trend that one cut-off frequency, or cut-off frequency pair that is more susceptible to this sensitivity than another, and it only occurs in the gastrocnemius muscles. There is currently no definitive answer as to why this is occurring. One hypothesis is that the calibration is finding a different set of parameters to be better than another for muscle excitations filtered differently. It may also be the sensitivity of the optimiser. Figure 39 shows the same data as Figure 38, in this case, all filtered at a low-pass frequency of 6 Hz, and high-pass frequencies of 10 Hz (blue), 20 Hz (red), 30 Hz (green) and 40 Hz (blue).

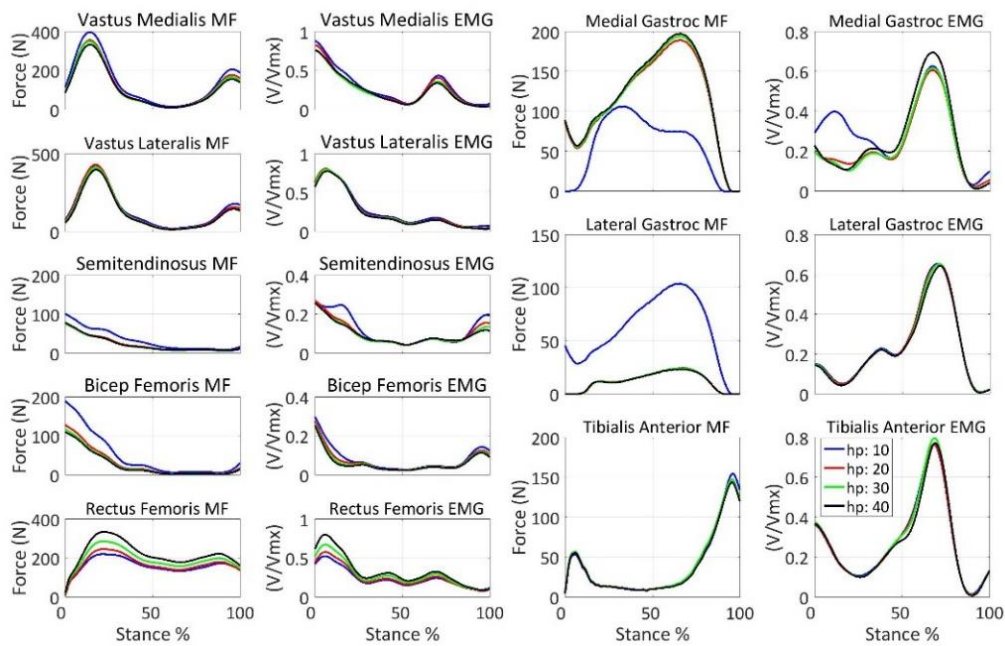


Figure 39: Muscle forces and EMGs of AKP 29 filtered at a low-pass cut-off of 6 Hz for the unaffected leg (right) of session one

The sensitivity of the gastrocnemius muscles is observed again. In this case, the high-pass cut-off frequency of 10 Hz introduces a peak in the EMG in stance phase of the medial gastrocnemius which translates to a change in the muscle force. This change in EMG in early stance phase is also observed in Figure 97 and Figure 100 in D.1. EMG processing results although less severe and consequently having a lesser effect on the resultant muscle force. The first two figures in this subchapter compare the different low-pass frequencies. Despite the higher frequency components visible in the signals low-passed at a higher frequency, these components do not translate to higher frequency components in the muscle forces. The shape of the muscle forces is consistent between processing techniques, with only a change in force levels, rather than a change in shape. Similarly for the comparison of high-pass frequencies where, with the exception of the high-pass frequency of 10 Hz, the shapes of the both the EMGs and the Muscle forces are very similar.

Figure 40 shows the mean normalised EMG for every muscle at which EMGs were acquired. For each different processing technique, all the recorded EMG values during the session were averaged (discarding zero values) and then normalised against the maximum value. This figure indicates the mean normalised EMG level. This figure shows that the mean EMG level is primarily dependant on the low-pass cut-off frequency. As seen in the figure the 3 Hz (black) low-passed data are consistently higher followed by the 6 Hz (red) and the 10 Hz (blue) data. For each low-pass grouping, there appears to be no consistent relationship between the

mean level and the high-pass cut-off frequency. The trend seen in Figure 40 is consistent with what is seen on all the EMG processing results, where the lower low-pass cut-off frequency resultant muscle force is higher.

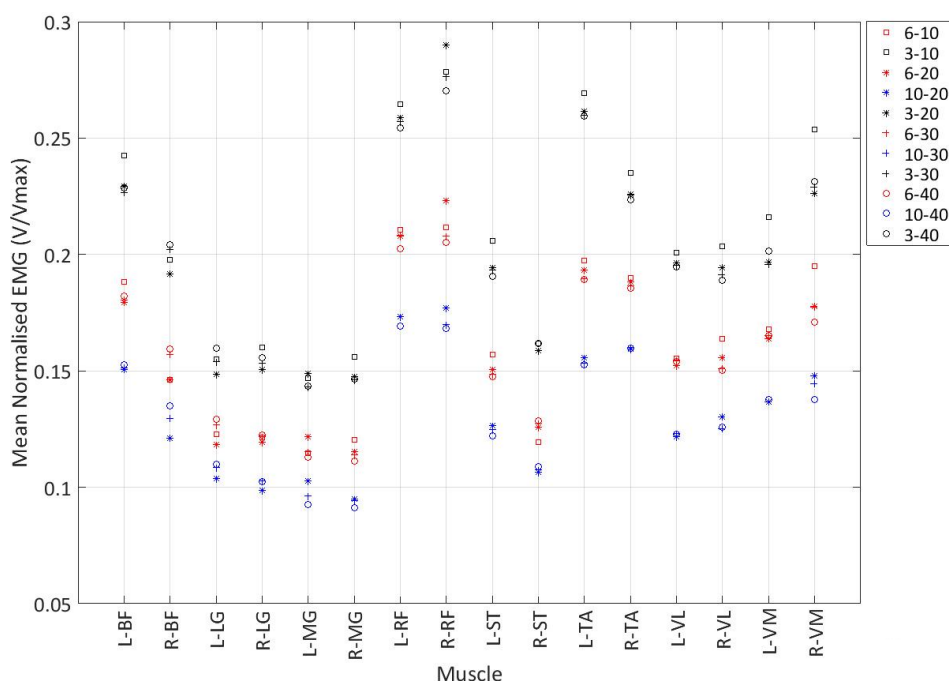


Figure 40: Mean EMG at each frequency normalised by the maximum at the frequency

Subjects AKP 03, 16, 17 and 29 were used to compare normalisation techniques, with subject AKP 30 omitted due to unsuitable MVC recordings. Figure 41 shows the results of subject AKP 17, with the results of the remaining subjects in Appendix D.2. EMG normalisation results. It is important to note that the MVC values include the walking trial maximums, this is required in the case of the walking trial maximum EMG value being larger than the MVC value. If the MVC values were used alone, the normalised EMG for a number of muscles would peak at values higher than one.

The blue shaded region indicates the change in the muscle force between the MVC vs WTM trials for session one, with the blue line indicating the muscle force calculated using the WTM normalised EMG and the green line representing the muscle force calculated using the MVC normalised EMG trials. Similarly, for session four, the red shaded region indicates the change in muscle force level with the red line showing the muscle force calculated using the WTM normalised EMG and the black line showing the muscle force calculated using the MVC normalised EMG.

The results again show the sensitivity of the optimiser when calculating the medial and lateral gastrocnemius muscle force. The significant change in gastrocnemius

force seen for every subject, except for subject AKP 16, cannot be attributed to the change in normalisation technique but rather due to the optimiser's sensitivity. There are, however, other significant changes seen in other muscles for which the change in normalisation is responsible. Figure 41 shows a significant change in the muscles contributing to knee flexion-extension for both sessions and on both legs.

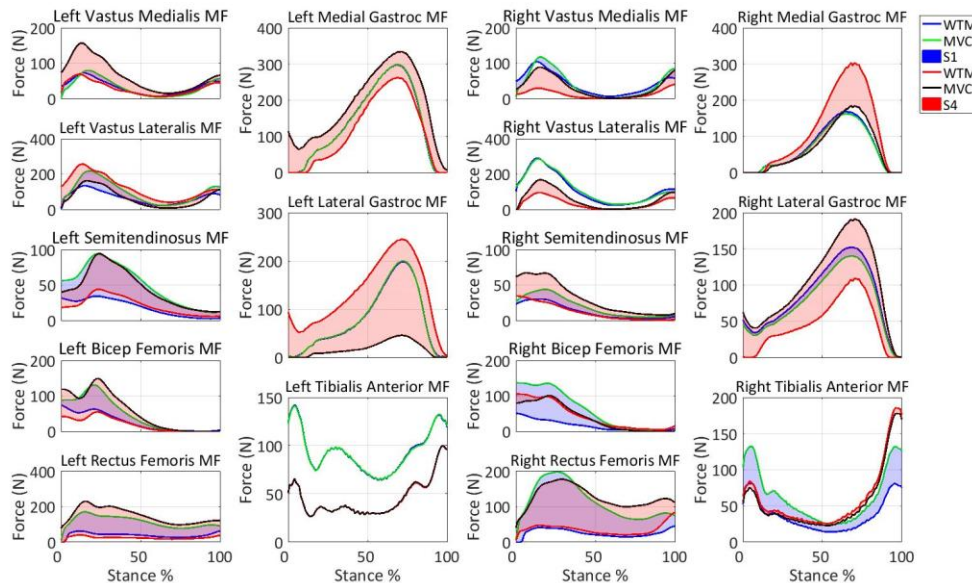


Figure 41: Muscle forces for AKP 17 using EMGs normalised using MVC vs WTM

When examining the change in muscle forces, it is necessary to consider the combined contributions of the muscles. The MVC muscle forces for the fourth session on the left leg, in Figure 41, show an increase in the vastus medialis, semitendinosus, bicep femoris and rectus femoris force and a reduction in the vastus lateralis force. When analysed together, the increase in contribution for the flexion muscles is matched by the increase in force for the extension muscles. The same pattern is found across the subjects, sessions and legs.

Figure 42 compares the maximum in trial EMG and the MVC (MVCs combined with WTM) EMG values used to normalise the EMG data. This figure provides insight into which muscles showed the most substantial difference in normalisation values, as well as which maximum values typically occurred during walking. The figure also provides insight into the different EMG levels across different subjects. If the MVC value is equal to the WTM value the maximum value across both methods occurred during the trials. It is clear from Figure 42 that this occurred most commonly for the gastrocnemius, in which the maximum value came from the trials for every subject except for subject AKP 16 for the left gastrocnemius. Most of the remaining muscles typically see a higher activation level during the MVC with the exception of the tibialis anterior in which subject AKP 29 and AKP 03 had maximum excitations during walking for both legs, and subject AKP 16 and AKP 17 had greater excitations

during the MVC trial for their left and right tibialis anterior, with the opposing leg maximum reached during the trial.

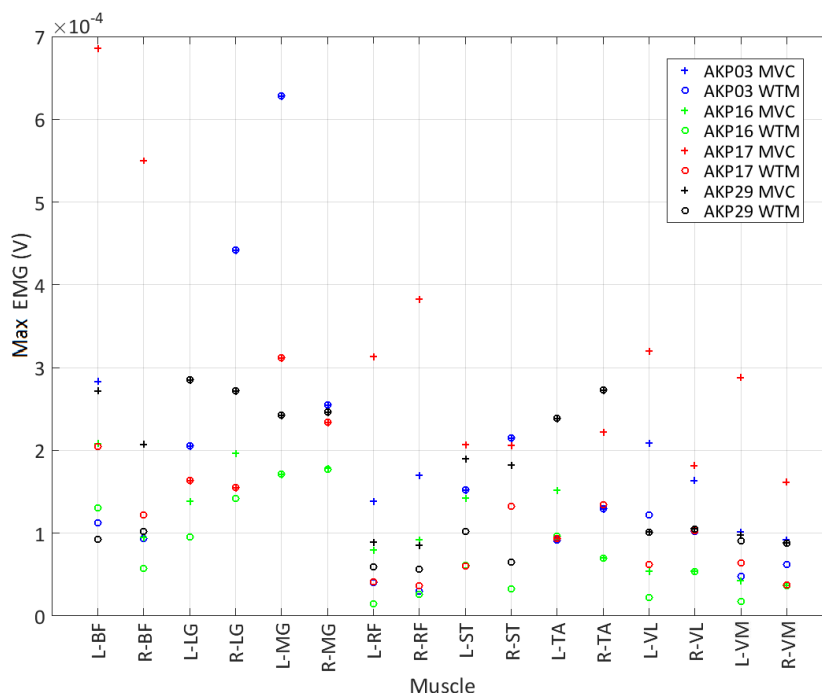


Figure 42: MVC vs WTM normalisation values for session one

The changes in EMG normalisation levels do not linearly reflect the change in the muscle force values. With subject AKP 17 as an example, the significantly increased level in normalisation for the vastus medialis and lateralis are not reflected in the change in muscle forces in Figure 41. Table 20 shows the H and P value for the data normalised using different techniques.

Table 20: Test decision value H, and P value for the muscle forces normalisation data for session one

Muscle	AKP 03		AKP 16		AKP 17		AKP 29	
	(H) [P]		(H) [P]		(H) [P]		(H) [P]	
	Left	Right	Left	Right	Left	Right	Left	Right
VM	(1)	(1)	(1)	(1)	(1)	(1)	[0.170]	[0.634]
VL	(1)	(1)	(1)	[0.572]	(1)	(1)	(1)	(1)
SEM	(1)	(1)	(1)	(1)	(1)	(1)	(1)	(1)
BF	(1)	(1)	(1)	(1)	(1)	(1)	(1)	(1)
RF	(1)	(1)	(1)	(1)	(1)	(1)	(1)	(1)
MG	(1)	(1)	(1)	(1)	(1)	[0.423]	(1)	(1)
LG	(1)	(1)	(1)	(1)	(1)	(1)	(1)	(1)
TA	(1)	(1)	(1)	[0.611]	(1)	(1)	[0.611]	(1)

Table 20 shows a significant change in the muscle forces for the majority of the muscles of every subject. It is therefore evident that the normalisation technique significantly affects the outcome of the muscle forces. However, the exact causal relationships need to be further investigated.

6.4. Results of CEINMS

Using CEINMS to determine the muscle forces was a principal aim of this project. Investigations of processing techniques for both force plate and marker data, as well as EMG data, were performed. Using the results of those investigations, the final results were acquired using EMG data filtered at a low-pass frequency of 6 Hz and a high-pass frequency of 30 Hz, normalised using the walking trial maximums. The OpenSim data used was calculated from force plate and marker data both filtered using a low-pass filter with a cut-off frequency of 10 Hz.

The results showed high repeatability with an average COD, R^2 of 0.83 ± 0.2 , as shown in Table 21. Across all the subjects the vastus medialis, vastus lateralis, semitendinosus, bicep femoris, medial gastrocnemius and lateral gastrocnemius had R^2 values over 0.83, while the rectus femoris and tibialis anterior had R^2 values of 0.65 and 0.67 respectively. The rectus femoris has been shown to have poor signal quality, and a non-uniform innervation zone between subjects, and the tibialis anterior has been shown to have a non-uniform innervation zone between subjects (Rainoldi *et al.*, 2004). The remaining muscles have been shown to have a high signal quality and uniform innervation zone between subjects (Rainoldi *et al.*, 2004). This is identified as the cause of the reduced COD for the tibialis anterior and rectus femoris.

Table 21: Coefficient of determination for the muscle forces

Muscle	AKP 03 (R^2)		AKP 16 (R^2)		AKP 17 (R^2)		AKP 29 (R^2)		AKP 30 (R^2)	
	Left	Right								
VM	(0.74)	(0.99)	(0.98)	(0.97)	(0.80)	(0.98)	(0.80)	(0.77)	(0.98)	(1.00)
VL	(0.63)	(0.96)	(0.78)	(0.48)	(0.99)	(0.84)	(0.88)	(0.97)	(0.98)	(0.97)
SEM	(0.74)	(0.63)	(0.99)	(0.95)	(0.96)	(0.96)	(0.96)	(0.96)	(1.00)	(0.95)
BF	(0.32)	(0.80)	(0.98)	(0.49)	(0.97)	(0.99)	(0.99)	(0.82)	(0.99)	(0.98)
RF	(0.38)	(0.75)	(0.84)	(0.03)	(0.95)	(0.85)	(0.43)	(0.73)	(0.87)	(0.64)
MG	(0.86)	(0.87)	(0.95)	(0.83)	(0.95)	(0.96)	(0.97)	(0.99)	(0.95)	(0.96)
LG	(0.82)	(0.88)	(0.95)	(0.93)	(0.99)	(0.99)	(0.99)	(0.51)	(0.89)	(1.00)
TA	(0.78)	(0.90)	(0.24)	(0.36)	(0.67)	(0.66)	(0.69)	(0.90)	(0.88)	(0.66)

Figure 43 shows the legend for the muscle plots that follow. The dashed blue line shows the mean of session one, with the shaded area representing the difference

between the maximum and minimum muscle force for session one. The green line and green shaded area represent the same thing for session four.



Figure 43: Legend for the muscle force plots

Figure 44 shows the muscle forces for subject AKP 03 across the first and final session. Figure 45 and Figure 46 show the same thing for AKP 16 and AKP 29 respectively. Figure 116 and Figure 117 in Appendix E. Muscle force results, show the results for subject AKP 17 and AKP 30 respectively. All of the subjects show similar muscle force shapes across all the muscles. The vastus medialis and vastus lateralis typically show a peak early in stance phase, with a peak again at the end. Both gastrocnemius muscles typically have a peak at around 70% of stance phase. The tibialis anterior is characterised as having a short peak early on, after which it is typically flat till increasing again from around 80% of stance phase. These five muscles show the highest similarity between subjects.

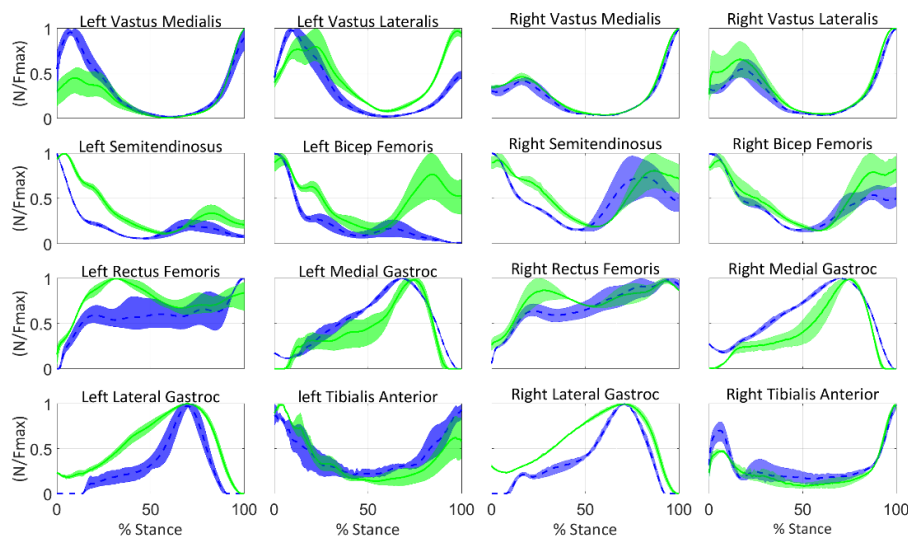


Figure 44: AKP 03 muscle forces

The rectus femoris shows a peak at around 25% of stance phase, followed by a slow decline with a smaller peak close to 90% of stance phase. This shape is less consistent across subjects, with a rising force seen in subject AKP 03 and less visible peaks around 90% for subject AKP 30. The semitendinosus and bicep femoris muscle, which form part of the hamstring typically show the same shape across a single subject, but a less consistent shape between subjects. These muscles typically decline from 0 % of stance phase with some subjects showing a small peak

of differing magnitude around 20% (AKP 16, AKP 29 and AKP 17) and subject AKP 03 showing another peak around 90%. The muscle force shapes show good agreement with muscles forces shown in the literature (Besier *et al.*, 2009; Arnold *et al.*, 2014). The vastus medialis and lateralis, as well as the medial and lateral gastrocnemius show very similar shapes to the study performed by Besier *et al.* (2009), however, the data for this study shows higher normalised levels. Only the right leg of subject AKP 16 appears to show inconsistent results. This is most likely due to a combination of the non-realistic knee moment discussed in Chapter 5.8.3, and incorrect EMGs.

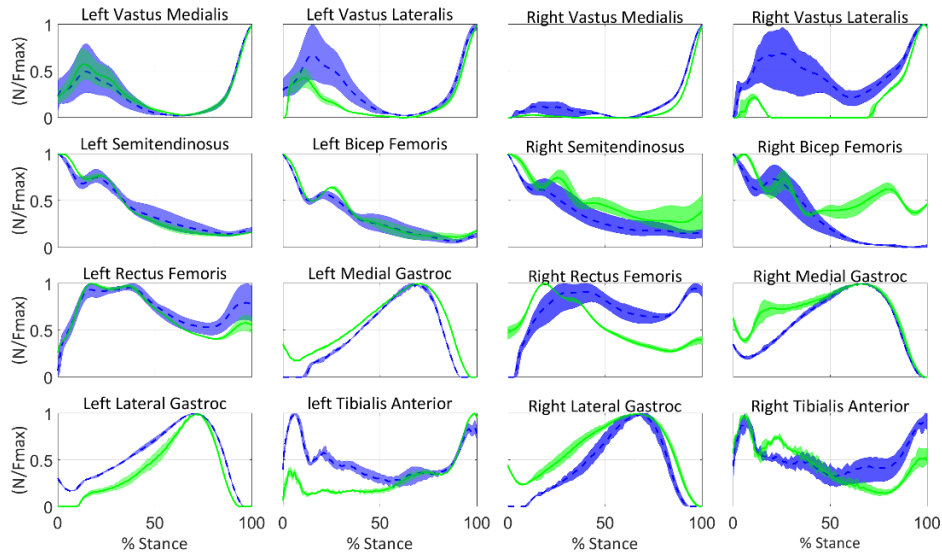


Figure 45: AKP 16 muscle forces

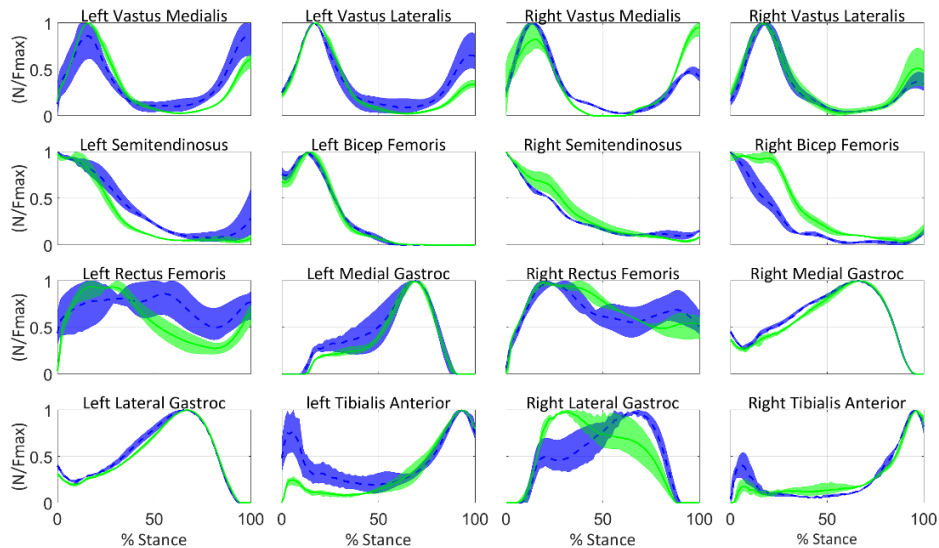


Figure 46: AKP 29 muscle forces

In order to make clinical assessments of the data, it is necessary to determine whether significant changes have taken place between sessions. Table 22 shows the results of t-test performed to compare the pre- and post-intervention muscle force results. In Table 22, if the H value is zero, the P value is given. Most of the muscles experience a significant change across between sessions ($P < 0.05$; $H = 1$). P values were greater than 0.05 for the left semitendinosus of subject AKP 16 (0.067); the left vastus lateralis and right semitendinosus of subject AKP 17 (0.469 and 0.471); the right vastus lateralis, right rectus femoris, left lateral gastrocnemius and right tibialis anterior of subject AKP 29 (0.827, 0.073, 0.54, 0.292 respectively); and the right vastus lateralis and right tibialis anterior of subject AKP 30 (0.95 and 0.258).

Table 22: Test decision value H , and P value for the muscle forces

Muscle	AKP 03		AKP 16		AKP 17		AKP 29		AKP 30	
	(H) [P]		(H) [P]		(H) [P]		(H) [P]		(H) [P]	
	Left	Right	Left	Right	Left	Right	Left	Right	Left	Right
VM	(1)	(1)	(1)	(1)	(1)	(1)	(1)	(1)	(1)	(1)
VL	(1)	(1)	(1)	(1)	[0.469]	(1)	(1)	[0.827]	(1)	[0.95]
SEM	(1)	(1)	[0.067]	(1)	(1)	[0.471]	(1)	(1)	(1)	(1)
BF	(1)	(1)	(1)	(1)	(1)	(1)	(1)	(1)	(1)	(1)
RF	(1)	(1)	(1)	(1)	(1)	(1)	(1)	[0.073]	(1)	(1)
MG	(1)	(1)	(1)	(1)	(1)	(1)	(1)	(1)	(1)	(1)
LG	(1)	(1)	(1)	(1)	(1)	(1)	[0.54]	(1)	(1)	(1)
TA	(1)	(1)	(1)	(1)	(1)	(1)	(1)	[0.292]	(1)	[0.258]

Despite the statistically significant changes in most of the muscles forces across sessions, it is not yet possible to determine how much of this change is due to experimental and modelling errors, and how much of it is due to physiological changes in the subject due to physiotherapy. With intra-subject comparisons being made, as in this project, it is important that there is a full understanding of the extent of the errors. More research is required to quantify the changes due to modelling and experimental errors. Particularly errors that arise due to long periods between testing dates.

7. Conclusion

This project aims to establish a computational platform that can be used to determine joint kinematics, dynamics and muscle forces from experimental data obtained from a motion analysis. It forms part of a more extensive prospective study on anterior knee pain. The aim of the parent study is to assess the effect of a subject tailored physiotherapeutic intervention on patellofemoral pain risk factors and clinical outcomes during functional movement. The developed computational pipeline is semi-automated and reduces the need for user intervention. Algorithms used in the pipeline were evaluated, particularly the effect of parameter settings on the results of the pipeline using the data collected in this study. Critical points in the computational pipeline were not only identified, but their effect on the output was assessed.

7.1. Outcomes of the study

Four objectives were formulated through which the study aim could be achieved.

Objective 1: Measure joint geometry, kinematic and kinetic drivers of the musculoskeletal model during over-ground gait. The Central Analytical Facilities (CAF) Neuromechanics Unit was used to obtain experimental data for 30 subjects with anterior knee pain. Each subject performed gait trials (described in Chapter 3. Experimental procedure) in which ground reaction forces, muscle activity and kinematics were recorded. Ground reaction forces were measured using three force plates struck in succession during the trial. The muscle activity is recorded using wireless electromyography (EMG) attached to eight muscles on both the right and left leg. The subject's kinematics was recorded using an eight-camera infrared system that recorded the three-dimensional position of an array of reflective markers attached to the subject at bony landmarks and at positions to record segment movements on the lower limbs and torso.

During the experimental phase of this project, the Neuromechanics Unit was still in its infancy with strict protocols and quality controls still being worked out. Consequently, some subject's trials were discarded due to recording errors which left subjects with too few trials to make significant comparisons between sessions. Of the trials that were successfully recorded there were some cases where EMGs had been placed on the incorrect muscle without appropriate pictures from which to determine the placement. Muscles in which the EMG electrodes were obviously swapped the signals could be swapped back. However there were cases where the exact swapping could not be determined, and those particular subjects' EMG could not be used. In addition, the acquisition technique for the EMGs changed during the study and consequently required altered pre-processing techniques.

Ultimately these problems were solved, and the data for 16 subjects were received, with five subjects having the required number of trials (three) on their symptomatic leg for both the first and final session. This data, received in C3D format, contained all the required information to be applied to the modelling pipeline created during this project.

Objective 2: Develop an automated modelling pipeline in OpenSim (Simtk-confluence.stanford.edu, 2017) to determine kinematics, joint moments, joint moment arms and muscle lengths. The kinematic and force plate data received from the motion lab was used in an OpenSim computational modelling pipeline which included an OpenSim pre-processing plugin. Through the presented OpenSim pipeline it was possible to generate the required **outputs** from the **inputs** which enabled the subject-specific kinematics, dynamics and initial muscle parameters to be determined. This technique proved to be robust since it required little user intervention and produced flags where intervention was required.

The pre-processing tool could automatically extract the force plate, EMG and kinematic data, as well as information about the subject and session. The extracted force plate, marker and EMG data were then processed and placed in the appropriate files (walk.mot, walk.trc and emg.mot respectively) to be used in OpenSim. A static analysis was then performed to process the static trial which is placed in a separate file (cal.trc) to be used during the scaling process in OpenSim. This information was placed in a pre-determined and strict file system.

Batch OpenSim Processing Scripts (BOPS) (BOPS Simtk.org, 2017), an online OpenSim project was updated and modified to create the automated computational pipeline. The OpenSim pipeline was automated and was able to run through the full OpenSim pipeline with no user intervention. To achieve this level of automation, some scaling accuracy was sacrificed. The scaling results reported on in Chapter 5.8.1 describe the scaling errors. The study results show that through the applied process of automation, there were adverse effects on scaling accuracy. This was however deemed negligible since, for all but one subject, the errors remained below the recommended maximum levels. Based on the findings of this study, the automated process is recommended since the benefits of saving on intervention time outweigh the drawbacks of scaling errors which had little influence on the outputs downstream.

In order to automate the pipeline, it is necessary to pinpoint the points at which errors typically occur. The pipeline can then be set up in such a way that these errors can be minimised, and quality controls can be implemented to flag particular points. Scaling was the point at which the most errors occur. Scaling errors are typically misplaced markers; these cause exaggerated scaling factors. The hip markers used to scale the pelvis, were the most commonly misplaced markers used for segment scaling. A mismatch in scaling factors could be determined by comparing the scaling

factors for different segments of the same subjects. If the scaling problems were not identified during the scaling process, they were typically identified during the Residual Reduction Algorithm. Uncharacteristic large residual forces were typically due to kinematic errors often caused by incorrect scaling factors forcing the model to move non-realistically. The residual forces acted as an additional flag to return to scaling and reassess the marker position.

Inverse Kinematics (IK) showed comparable results to that seen in the literature (Barton *et al.*, 2009; Nadeau *et al.*, 1997). The IK results also showed high repeatability across sessions measured using the coefficient of determination ($R^2 = 0.93 \pm 0.11$), particularly for the knee. The joints in which the coefficient of determination was low, showed similar shaped but a constant offset. This offset is explained by a change in marker placement. The hip and ankle are particularly susceptible to this problem because of the short distance between the markers used to calculate their angle. The Inverse Dynamics results similarly showed high repeatability between sessions on average ($R^2 = 0.93 \pm 0.05$). It is expected that there is some change between knee moments and knee angles between sessions due to the interventions, however it difficult to quantify how much of the change is due to the intervention and how much is due to experimental end modelling errors. The repeatability of the IK and ID falls within the range seen in literature (Besier *et al.*, 2003; Kadaba *et al.*, 1989).

Residual Reduction Algorithm (RRA) was used to create an adjusted subject-specific model and kinematics that was more dynamically consistent with the kinematics and GRF. All of the residual forces calculated by RRA were within the recommended bounds. The F_y residuals were consistently higher than the rest of the results due to the y-direction having the largest forces, and so the largest errors.

This study showed that ID and RRA could be negatively impacted by improper force plate and marker post-processing algorithms. The force plate and marker data was filtered at five different frequency combinations. Previous literature (Roewer *et al.*, 2012; Bisseling *et al.*, 2006; Bezodis *et al.* 2012) all found visible artefacts in the knee moment for high impact activities when filtering marker and force plate data at different frequencies. This study found that the same artefact is also visible knee moments during gait. The results displayed in Chapter 5.8.5 show a significant difference between the knee moments determined from force plate and marker data filtered at the same frequency compared to the same data filtered at different frequencies. The most significant result is when comparing the force plate and marker data filtered at 15 - 15 Hz compared to the data filtered at 15 - 10 Hz. Despite being filtered at a lower filtering frequency, the data filtered using 15 - Hz cut-off has consistently had a more substantial spike at impact compared to the data filtered at the same frequency.

The pipeline incorporated CMC which enabled the generation of the required outputs which were extracted using the Analysis tool to generate the inputs for CEINMS.

Objective 3: Extend the modelling pipeline to apply the OpenSim results to the Calibrated EMG informed Neuromusculoskeletal Software to estimate muscle forces. The results of the OpenSim analysis, as well as the EMG data, was used in CEINMS; an EMG informed suite that uses an optimisation process to create subject-specific muscle parameters, which is then used to determine muscle forces.

An automated modelling pipeline was created from scratch that created all the necessary setup and configuration files, provided the necessary input data was available and ran the full CEINMS pipeline to determine muscle forces. The muscle forces determined using CEINMS showed comparable results to those found in the literature (Besier *et al.*, 2009; Arnold *et al.*, 2013). Most of the muscles showed high repeatability measured using the coefficient of determination. In particular, the vastus medialis, vastus lateralis, semitendinosus, bicep femoris, medial gastrocnemius and lateral gastrocnemius all had coefficients of determination higher than 0.8, while the rectus femoris and tibialis anterior had coefficients of determination of 0.65 and 0.67 respectively.

A significant change in most of the muscle forces was observed across sessions for all of the subjects. All of the subjects had 12 or more muscles with a significant change across sessions ($P < 0.05$). Despite the statistically significant changes in most of the muscles forces across sessions, more research is required to determine the extent to which modelling and experimental errors account for the change.

Objective 4: Extract electromyography (EMG) results, and determine appropriate filtering to use in muscle force prediction. The raw EMG data obtained from the experimental testing requires significant processing to be usable (Burden *et al.*, 2003). In this project, the EMG data are used as an input to CEINMS, a newly created tool that uses EMGs to inform a neuromusculoskeletal model. Although the effects of EMG filtering on the EMG results have been widely published (Buchanan *et al.*, 2004; Devaprakash *et al.*, 2016) the influence of EMG filtering changes on CEINMS results has not been reported.

The EMGs recorded during this study were filtered at 11 different low-pass and high-pass cut-off frequency combinations which were then used to recalibrate the subject-specific model with the same OpenSim data in the calibration step of CEINMS. The results of this analysis are shown in Chapter 6.3.3.

Changing the low-pass frequencies while holding the high-pass frequencies constant affected the magnitude of the muscle force, however, the introduction of higher frequency components in the EMG did not affect the shape of the muscle

force. Changing the high-pass frequency while maintaining a constant low-pass frequency showed less of an effect on the EMG values and consequently less of an effect on the muscle forces with the exception of the high-pass cut-off of 10 Hz.

A comparison of maximum voluntary contraction trials against walking trial maximums for use in normalisation and their influence on muscle forces were also investigated. Significant changes were observed in the muscle forces across the two techniques for the majority of the muscles for every subject. The exact causal relationship between changes in EMG and optimiser output need to be further investigated with the muscle contribution looked at in the context of their synergistic contributions and an in-depth understanding of the optimiser.

A sensitivity of the optimiser was observed for both the lateral and medial gastrocnemius muscles. Substantial changes in both muscles were observed across different frequencies with the sum of the two muscles remaining approximately constant across frequencies. The muscles responsible for each joint moment used in CEINMS are prescribed in the subject file. The two gastrocnemius muscles are the only two biarticulate muscles, crossing both the knee joint and the ankle joint. It is hypothesised that the optimiser is particularly sensitive to such muscles. No significant relationship between the cut-off frequency, muscle configuration and muscle force could be determined from the data. Future work is required to expand on this.

7.2. Future work

Future projects will benefit from improved protocols and quality controls during testing. More trials should also be obtained during the experiments to account for lost trials due to error and to make more significant comparisons. Protocols, like taking detailed pictures of markers and EMG electrodes with electrodes numbers, would allow errors to be rectified in processing. A dynamometer would improve the maximum EMG values determined during maximum voluntary contraction trials.

Scaling was identified as a critical point in the pipeline. Improved scaling techniques, such as scaling the X, Y and Z dimension of the pelvis separately, would create more accurate models, and reduce errors throughout the pipeline. This would require the modification of the OpenSim scaling code. New scaling techniques (Valente *et al.*, 2017) would also create a more accurately scaled model. Newly created full-body models (Rajagopal *et al.*, 2016) that include the arms (which would require arm markers) and patella would provide additional dynamic consistency and would allow for more accurate kinematic and dynamic results at the knee joint.

This project had a first attempt at identifying and quantifying critical steps in the modelling pipeline. This is however only a first step, and the results show that a more in-depth investigation into the modelling pipeline is warranted. In addition, the experimental protocol and its effect on modelling outcomes also need to be considered, since any model is highly dependent on the experimental data from which initial and boundary conditions are derived. A more in-depth look at the scaling and processing techniques would create a better understanding of these influences.

Finally, the computational tool that was created could be improved to make it adaptable across projects. Currently, the tool is specific to this project and is set up to receive data in the form created by the lab. This project established a data management protocol which is robust and which could be applied to other projects. Improved automated quality checks and controls could also be implemented to further reduce user input.

7.3. Contributions to the field

The contributions to the field made during this project are three-fold. The most significant contribution of this study to the field was the computational pipeline that was created. Newly acquired data could be inputted into the pipeline with few changes, and results could be determined. The pipeline also allows for easy modification of processing techniques, which allows for fast investigations of the influence of modelling changes. With some modification, the tool can also be adaptable to different projects, and different types of input data.

The project contributed to the existing information on computational studies of patellofemoral pain. The project also provided insight into the processing techniques of kinematic and EMG data. The processing of force plate and marker data was investigated and the influence on the resultant knee moment was reported, residual forces were also used as a novel method for investigation non-real characteristics between forces and markers. Different high and low-pass cut-off frequencies were used to filter EMGs, and their influence on the CEINMS results was reported for the first time in this study.

References

Anderson, F.C., John, C. T., Guendelman, E., Arnold, A.S. and Delp, S.L., 2006. SimTrack: Software for rapidly generating muscle-actuated simulations of long-duration movement.

Anderson, F.C. Pandy, M.G., 2001. Dynamic optimization of human walking. *Journal of biomechanical engineering*, 123(5), pp.381-390.

Arnold, E.M., Hamner, S.R., Seth, A., Millard, M. and Delp, S.L., 2013. How muscle fiber lengths and velocities affect muscle force generation as humans walk and run at different speeds. *Journal of Experimental Biology*, 216(11), pp.2150-2160.

Barre, A. and Armand, S., 2014. Biomechanical ToolKit: Open-source framework to visualize and process biomechanical data. *Computer methods and programs in biomedicine*, 114(1), pp.80-87.

Barton, C.J., Levinger, P., Menz, H.B. and Webster, K.E., 2009. Kinematic gait characteristics associated with patellofemoral pain syndrome: a systematic review. *Gait & posture*, 30(4), pp.405-416.

Basmajian, J.V. and De Luca, C.J., 1985. *Muscles alive: their functions revealed by electromyography*. Williams & Wilkins.

Besier, T.F., Fredericson, M., Gold, G.E., Beaupré, G.S. and Delp, S.L., 2009. Knee muscle forces during walking and running in patellofemoral pain patients and pain-free controls. *Journal of biomechanics*, 42(7), pp.898-905.

Besier, T.F., Sturnieks, D.L., Alderson, J.A. and Lloyd, D.G., 2003. Repeatability of gait data using a functional hip joint centre and a mean helical knee axis. *Journal of biomechanics*, 36(8), pp.1159-1168.

Bezodis, N.E., Salo, A.I. and Trewartha, G., 2013. Excessive fluctuations in knee joint moments during early stance in sprinting are caused by digital filtering procedures. *Gait & posture*, 38(4), pp.653-657.

Bisseling, R.W. and Hof, A.L., 2006. Handling of impact forces in inverse dynamics. *Journal of biomechanics*, 39(13), pp.2438-2444.

Bland, J.M. and Altman, D.G., 1999. Measuring agreement in method comparison studies. *Statistical methods in medical research*, 8(2), pp.135-160.

Boling, M., Padua, D., Marshall, S., Guskiewicz, K., Pyne, S. and Beutler, A., 2010. Gender differences in the incidence and prevalence of patellofemoral pain syndrome. *Scandinavian journal of medicine & science in sports*, 20(5), pp.725-730.

Buchanan, T.S., Lloyd, D.G., Manal, K. and Besier, T.F., 2004. Neuromusculoskeletal modeling: estimation of muscle forces and joint moments and movements from measurements of neural command. *Journal of applied biomechanics*, 20(4), pp.367-395.

Burden, A.M., Trew, M. and Baltzopoulos, V., 2003. Normalisation of gait EMGs: a re-examination. *Journal of Electromyography and Kinesiology*, 13(6), pp.519-532.

C3d.org. (2017). C3D file format and documentation. [online] Available at: <https://www.c3d.org/overview.html> [Accessed 6 Oct. 2017].

Cappozzo, A., Della Croce, U., Leardini, A. and Chiari, L., 2005. Human movement analysis using stereophotogrammetry: Part 1: theoretical background. *Gait & posture*, 21(2), pp.186-196.

Ceseracciu, E., Reggiani, M., 2015. CEINMS User Guide Documentation. *Release 0.9.0*. REHABILITATION ENGINEERING GROUP.

Clancy, E.A., Morin, E.L. and Merletti, R., 2002. Sampling, noise-reduction and amplitude estimation issues in surface electromyography. *Journal of Electromyography and Kinesiology*, 12(1), pp.1-16.

Clauser, C.E., McConville, J.T. and Young, J.W., 1969. Weight, volume, and center of mass of segments of the human body. ANTIOCH COLL YELLOW SPRINGS OH.

Clinical Gate. (2017). Ankle and Foot. [online] Available at: <https://clinicalgate.com/ankle-and-foot/> [Accessed 6 Feb. 2017].

Corana, A., Marchesi, M., Martini, C. and Ridella, S., 1987. Minimizing multimodal functions of continuous variables with the "simulated annealing" algorithm. Corrigenda for this article is available here. *ACM Transactions on Mathematical Software (TOMS)*, 13(3), pp.262-280.

Davis, R.B., Ounpuu, S., Tyburski, D. and Gage, J.R., 1991. A gait analysis data collection and reduction technique. *Human movement science*, 10(5), pp.575-587.

De Jongh, B., 2016. Computational modelling techniques to determine patellofemoral joint reaction forces (Masters dissertation, Stellenbosch: Stellenbosch University).

Della Croce, U., Leardini, A., Chiari, L. and Cappozzo, A., 2005. Human movement analysis using stereophotogrammetry: Part 4: assessment of anatomical landmark misplacement and its effects on joint kinematics. *Gait & posture*, 21(2), pp.226-237.

Delp, S.L., Anderson, F.C., Arnold, A.S., Loan, P., Habib, A., John, C.T., Guendelman, E. and Thelen, D.G., 2007. OpenSim: open-source software to create and analyze dynamic simulations of movement. *IEEE transactions on biomedical engineering*, 54(11), pp.1940-1950.

Delp, S.L., Loan, J.P., Hoy, M.G., Zajac, F.E., Topp, E.L. and Rosen, J.M., 1990. An interactive graphics-based model of the lower extremity to study orthopaedic surgical procedures. *IEEE Transactions on Biomedical engineering*, 37(8), pp.757-767.

Devaprakash, D., Weir, G.J., Dunne, J.J., Alderson, J.A. and Donnelly, C.J., 2016. The influence of digital filter type, amplitude normalisation method, and co-contraction algorithm on clinically relevant surface electromyography data during clinical movement assessments. *Journal of Electromyography and Kinesiology*, 31, pp.126-135.

Emedicine.medscape.com. (2017). Motor Unit Recruitment in EMG: Definition of Motor Unit Recruitment and Overview, Order of Recruitment, Assessment of Recruitment at Low Level of Muscle Contraction. [online] Available at: <https://emedicine.medscape.com/article/1141359-overview> [Accessed 7 Nov. 2017].

Farrohkhi, S., Keyak, J. & Powers, C., 2011. Individuals with patellofemoral pain exhibit greater patellofemoral joint stress: a finite element analysis study. *Osteoarthritis and Cartilage*, Issue 19, pp. 287-294.

Goffe, W.L., Ferrier, G.D. and Rogers, J., 1994. Global optimization of statistical functions with simulated annealing. *Journal of econometrics*, 60(1-2), pp.65-99.

Harrington, M.E., Zavatsky, A.B., Lawson, S.E.M., Yuan, Z. and Theologis, T.N., 2007. Prediction of the hip joint centre in adults, children, and patients with cerebral palsy based on magnetic resonance imaging. *Journal of biomechanics*, 40(3), pp.595-602.

Hettrich, C. M. & Lietchi, D., 2015. OrthoInfo: Patellofemoral Pain Syndrome. [Online] Available at: <http://orthoinfo.aaos.org/topic.cfm?topic=A00680> [Accessed 21 June 2016].

Huijing, P.A., 1996. Important experimental factors for skeletal muscle modelling: non-linear changes of muscle length force characteristics as a function of degree of activity. *European journal of morphology*, 34(1), pp.47-54.

- Inman, V.T., 1976. The joints of the ankle. Williams & Wilkins, Baltimore.
- Kadaba, M.P., Ramakrishnan, H.K., Wootten, M.E., Gainey, J., Gorton, G. and Cochran, G.V.B., 1989. Repeatability of kinematic, kinetic, and electromyographic data in normal adult gait. *Journal of Orthopaedic Research*, 7(6), pp.849-860.
- Kainz, H., Hoang, H., Stockton, C., Boyd, R.R., Lloyd, D.G. and Carty, C.P., 2017. Accuracy and reliability of marker based approaches to scale the pelvis, thigh and shank segments in musculoskeletal models. *Journal of Applied Biomechanics*, pp.1-21.
- Kirk, A.G., O'Brien, J.F. and Forsyth, D.A., 2005, June. Skeletal parameter estimation from optical motion capture data. In *Computer Vision and Pattern Recognition, 2005. CVPR 2005. IEEE Computer Society Conference on (Vol. 2, pp. 782-788)*. IEEE.
- Klijn, J.A.J. and Kloprogge, M.J.G.M., 1974. Movement artefact suppressor during ECG monitoring. *Cardiovascular research*, 8(1), pp.149-152.
- Knudson, D., 2012. *Fundamentals of biomechanics*. New York: Springer.
- Kristianslund, E., Krosshaug, T. and Van den Bogert, A.J., 2012. Effect of low-pass filtering on joint moments from inverse dynamics: implications for injury prevention. *Journal of biomechanics*, 45(4), pp.666-671.
- Kuo, A.D., 1998. A least-squares estimation approach to improving the precision of inverse dynamics computations. *Journal of biomechanical engineering*, 120(1), pp.148-159.
- Leardini, A., Chiari, L., Della Croce, U. and Cappozzo, A., 2005. Human movement analysis using stereophotogrammetry: Part 3. Soft tissue artifact assessment and compensation. *Gait & posture*, 21(2), pp.212-225.
- Lehman, G.J. and McGill, S.M., 1999. The importance of normalization in the interpretation of surface electromyography: a proof of principle. *Journal of manipulative and physiological therapeutics*, 22(7), pp.444-446.
- Lembeck, B., Mueller, O., Reize, P. and Wuelker, N., 2005. Pelvic tilt makes acetabular cup navigation inaccurate. *Acta orthopaedica*, 76(4), pp.517-523
- Lewis, F.L., Abdallah, C.T. and Dawson, D.M., 1993. *Control of robot manipulators (Vol. 236)*. New York: Macmillan.
- Lin, Y.C., Dorn, T.W., Schache, A.G. and Pandy, M.G., 2012. Comparison of different methods for estimating muscle forces in human movement. *Proceedings of the Institution of Mechanical Engineers, Part H: Journal of Engineering in Medicine*, 226(2), pp.103-112.

Lloyd, D.G. and Besier, T.F., 2003. An EMG-driven musculoskeletal model to estimate muscle forces and knee joint moments in vivo. *Journal of biomechanics*, 36(6), pp.765-776.

Lloyd, D.G., Besier, T.F., Winby, C.R. and Buchanan, T.S., 2008. Neuromusculoskeletal modelling and simulation of tissue load in the lower extremities. *Handbook of Biomechanics and Human Movement Science*. New York: Routledge, pp.3-17.

Logan, C., 2005. Hip joint anatomy. [Online] Available at: <http://www.ideafit.com/fitness-library/hip-joint-anatomy> [Accessed 28 June 2016].

Lucchetti, L., Cappozzo, A., Cappello, A. and Della Croce, U., 1998. Skin movement artefact assessment and compensation in the estimation of knee-joint kinematics. *Journal of biomechanics*, 31(11), pp.977-984.

MacIntyre, N. J., Hill, R. A., Fellows, R. E. Ellis, and D. R. Wilson. "Patellofemoral joint kinematics in individuals with and without patellofemoral pain syndrome." *JBS* 88, no. 12 (2006): 2596-2605.

Manal, K. and Buchanan, T.S., 2003. A one-parameter neural activation to muscle activation model: estimating isometric joint moments from electromyograms. *Journal of biomechanics*, 36(8), pp.1197-1202.

Mantoan, A., Ceseracciu, E., Spolaor, F., Sawacha, Z. and Reggiani, M., 2015. On the effects of EMG normalisation in muscle forces estimation when using a multi-DOF EMG-driven neuromusculoskeletal model. In *15th International Symposium on Computer Simulation in Biomechanics* (p. 37).

Mantoan, A., Pizzolato, C., Sartori, M., Sawacha, Z., Cobelli, C. and Reggiani, M., 2015. MOtoNMS: A MATLAB toolbox to process motion data for neuromusculoskeletal modeling and simulation. *Source code for biology and medicine*, 10(1), p.12.

Mayo Clinic. (2015). Electromyography (EMG). [online] Available at: <https://www.mayoclinic.org/tests-procedures/emg/basics/definition/prc-20014183> [Accessed 12 Jun. 2017].

Merletti, R. and Parker, P.A. eds., 2004. *Electromyography: physiology, engineering, and non-invasive applications* (Vol. 11). John Wiley & Sons.

Milner-Brown, H.S., Stein, R.B. and Yemm, R., 1973. Changes in firing rate of human motor units during linearly changing voluntary contractions. *The Journal of physiology*, 230(2), pp.371-390.

Nadeau, Sylvie, Denis Gravel, Luc J. Hébert, A. Bertrand Arsenault, and Yves Lepage. "Gait study of patients with patellofemoral pain syndrome." *Gait & posture* 5, no. 1 (1997): 21-27.

Nisell, R., Németh, G. and Ohlsén, H., 1986. Joint forces in extension of the knee: analysis of a mechanical model. *Acta Orthopaedica Scandinavica*, 57(1), pp.41-46.

Noraxon USA. (2017). Home | Noraxon USA. [online] Available at: <https://www.noraxon.com/> [Accessed 10 Nov. 2017].

Opensim.stanford.edu. (2017). OpenSim - Home. [online] Available at: <http://opensim.stanford.edu/> [Accessed 10 Nov. 2017].

Palastanga, N., Field, D. & Soames, R., 2002. *Anatomy and human movement*. 4th ed. Oxford: Butterworth Heinemann.

Palmitier, R.A., An, K.N., Scott, S.G. and Chao, E.Y., 1991. Kinetic chain exercise in knee rehabilitation. *Sports medicine*, 11(6), pp.402-413.

Pappas, E. & Wong-Tom, W. M., 2012. Prospective Predictors of Patellofemoral Pain Syndrome: A systematic Review With Meta-analysis. *Sports Health: A Multidisciplinary Approach*, 4(2), pp. 115-120.

Parker, R. & Jelsma, J., 2010. The prevalence and functional impact of musculoskeletal conditions amongst clients of a primary health care facility in an under-resourced area of Cape Town.. *BMC Musculoskeletal Disorders*, 11(2), pp. 2-4.

Pizzolato, C., Lloyd, D.G., Sartori, M., Ceseracciu, E., Besier, T.F., Fregly, B.J. and Reggiani, M., 2015. CEINMS: A toolbox to investigate the influence of different neural control solutions on the prediction of muscle excitation and joint moments during dynamic motor tasks. *Journal of biomechanics*, 48(14), pp.3929-3936.

Rainoldi, A., Melchiorri, G. and Caruso, I., 2004. A method for positioning electrodes during surface EMG recordings in lower limb muscles. *Journal of neuroscience methods*, 134(1), pp.37-43.

Rajagopal, A., Dembia, C.L., DeMers, M.S., Delp, D.D., Hicks, J.L. and Delp, S.L., 2016. Full-body musculoskeletal model for muscle-driven simulation of human gait. *IEEE Transactions on Biomedical Engineering*, 63(10), pp.2068-2079.

Redfern, M.S., Hughes, R.E. and Chaffin, D.B., 1993. High-pass filtering to remove electrocardiographic interference from torso EMG recordings. *Clinical Biomechanics*, 8(1), pp.44-48.

Roewer, B.D., Ford, K.R., Myer, G.D. and Hewett, T.E., 2012. The 'impact' of force filtering cut-off frequency on the peak knee abduction moment during landing: artefact or 'artifiction'?. *Br J Sports Med*, pp.bjsports-2012.

Samuelparsons.co.uk. (2017). *orthopaedic Surgeon Mr Samuel Parsons Explains Knee Pain*. [online] Available at: http://www.samuelparsons.co.uk/knee_pain.html [Accessed 6 Nov. 2017].

Sartori, M., Lloyd, D.G., Besier, T.F., Fernandez, J.W. and Dario, F., 2016. Electromyography-driven modeling for simulating subject-specific movement at the neuromusculoskeletal level. *Electromyography: physiology, engineering, and non-invasive applications*. Hoboken, NJ: Wiley-IEEE Press, pp.247-272.

Schmidler, C. (2017). *Hip Anatomy, Pictures, Function, Problems & Treatment*. [online] Healthpages.org. Available at: <https://www.healthpages.org/anatomy-function/hip-structure-function-common-problems/> [Accessed 6 Feb. 2017].

Schmidler, C. (2017). *Knee Anatomy Pictures: Bones, Ligaments, Muscles, Tendons, Function*. [online] Healthpages.org. Available at: <https://www.healthpages.org/anatomy-function/knee-joint-structure-function-problems/> [Accessed 6 Feb. 2017].

Schwartz, M.H., Rozumalski, A. and Trost, J.P., 2008. The effect of walking speed on the gait of typically developing children. *Journal of biomechanics*, 41(8), pp.1639-1650.

Simtk-confluence.stanford.edu. (2017). OpenSim Documentation. [online] Available at: <https://simtk-confluence.stanford.edu/display/OpenSim/> [Accessed 12 June. 2017].

Simtk.org. (2017). SimTK: Batch OpenSim Processing Scripts (BOPS): Project Home. [online] Available at: <https://simtk.org/projects/bops> [Accessed 12 Nov. 2017].

Simtk.org. (2017). SimTK: Matlab MOTion data elaboration TOolbox for NeuroMusculoSkeletal apps (MOtoNMS): Project Home. [online] Available at: <https://simtk.org/projects/motonms> [Accessed 12 Nov. 2017].

Son, J., Hwang, S. and Kim, Y., 2010. An EMG-based muscle force monitoring system. *Journal of mechanical science and technology*, 24(10), pp.2099-2105.

Szczerbik, E. and Kalinowska, M.A.Ł.G.O.R.Z.A.T.A., 2011. The influence of knee marker placement error on evaluation of gait kinematic parameters. *Acta Bioeng Biomech Wroc Univ Technol*, 13, pp.43-46.

TeachMeAnatomy, 2016. *THE KNEE JOINT*. [Online] Available at: <http://teachmeanatomy.info/lower-limb/joints/the-knee-joint/> [Accessed 28 June 2016].

Thelen, D.G., 2003. Adjustment of muscle mechanics model parameters to simulate dynamic contractions in older adults. *Transactions-American Society of Mechanical Engineers Journal of Biomechanical Engineering*, 125(1), pp.70-77.

Thelen, D.G. and Anderson, F.C., 2006. Using computed muscle control to generate forward dynamic simulations of human walking from experimental data. *Journal of biomechanics*, 39(6), pp.1107-1115.

Thelen, D.G., Anderson, F.C. and Delp, S.L., 2003. Generating dynamic simulations of movement using computed muscle control. *Journal of biomechanics*, 36(3), pp.321-328.

Trinler, U. and Baker, R., 2017. Estimated landmark calibration of biomechanical models for inverse kinematics. *Medical Engineering & Physics*.

Valente, G., Crimi, G., Vanella, N., Schileo, E. and Taddei, F., 2017. nmsBuilder: Freeware to create subject-specific musculoskeletal models for OpenSim. *Computer Methods and Programs in Biomedicine*, 152, pp.85-92.

Van den Bogert, A.J. and De Koning, J.J., 1996, August. On optimal filtering for inverse dynamics analysis. In *Proceedings of the IXth biennial conference of the Canadian society for biomechanics* (pp. 214-215). Vancouver: Simon Fraser University.

Vaughan, C., Davis, B. & O'Conner, J., 1999. *Dynamics of Human Gait*. 2nd ed. Cape Town: Kibo publishers.

VICON. (2017). What is motion capture. [online] Available at: <https://www.vicon.com/what-is-motion-capture> [Accessed 10 June. 2017].

Webster, J.G., 1984. Reducing motion artifacts and interference in biopotential recording. *IEEE Transactions on Biomedical Engineering*, (12), pp.823-826.

Whittle, M.W., 1996. Clinical gait analysis: A review. *Human Movement Science*, 15(3), pp.369-387.

Whittle, M. W., 2007. *Gait Analysis: An introduction*. 4th ed. Oxford: Butterworth Heinemann Elsevier.

Witvrouw, E., Werner, S., Mikkelsen, C., Van Tiggelen, D., Berghe, L.V. and Cerulli, G., 2005. Clinical classification of patellofemoral pain syndrome: guidelines for non-operative treatment. *Knee Surgery, Sports Traumatology, Arthroscopy*, 13(2), pp.122-130.

Yamaguchi, G.T. and Zajac, F.E., 1989. A planar model of the knee joint to characterize the knee extensor mechanism. *Journal of biomechanics*, 22(1), pp.1-10.

Appendices

Appendix A. Marker labels

C7	7 TH Cervical vertebrae
CLAV	Clavicle
STRN	Sternum
T10	10 th Thoracic vertebrae
LASI	Left superior anterior iliac spine
RASI	Right superior anterior iliac spine
LPSI	Left posterior superior iliac spine
RPSI	Right posterior superior iliac spine
LTHI	Left thigh
RTHI	Right thigh
LKAD	Left medial knee
RKAD	Right medial knee
LKNE	Left lateral knee
RKNE	Right lateral knee
LSHI	Left shin
RSHI	Right shin
LTIB	Left tibial wand marker
RTIB	Right tibial wand marker
LANK	Left lateral ankle
RANK	Right lateral ankle
LMMA	Left medial ankle
RMMA	Right medial ankle
LTOE	Left toe
RTOE	Right toe
LHEE	Left heel
RHEE	Right heel
LHJC	Left hip joint centre
RHJC	Right hip joint centre
LKJC	Left knee joint centre
RKJC	Right knee joint centre
LAJC	Left ankle joint centre
RAJC	Right ankle joint centre

Appendix B. OpenSim results

B.1. Inverse Kinematics

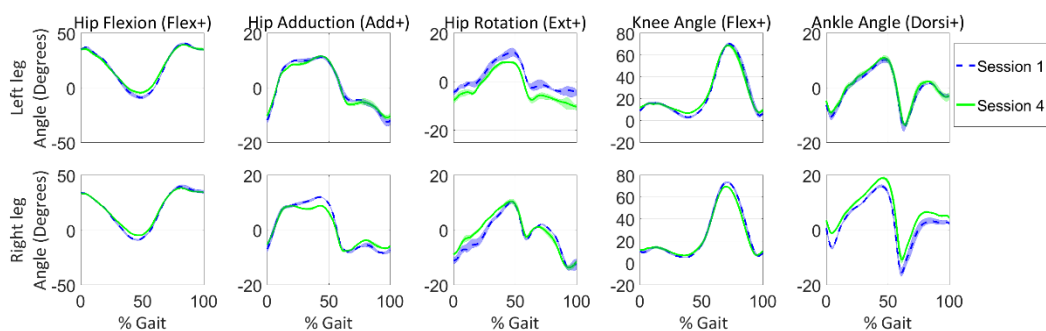


Figure 47: Session comparison of the IK for subject AKP 03

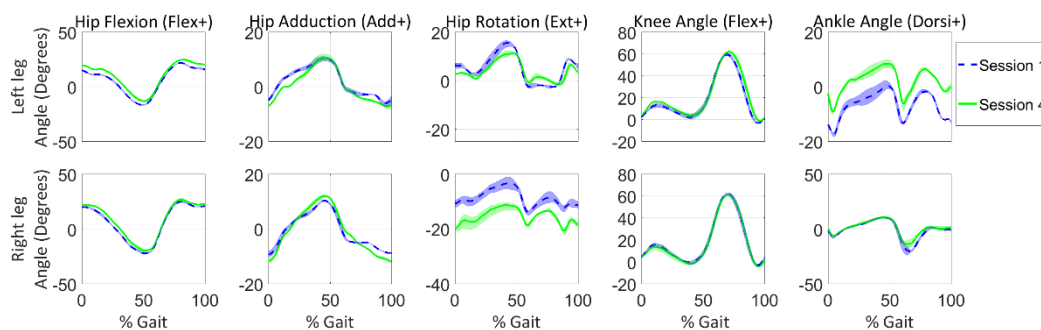


Figure 48: Session comparison of the IK for subject AKP 17

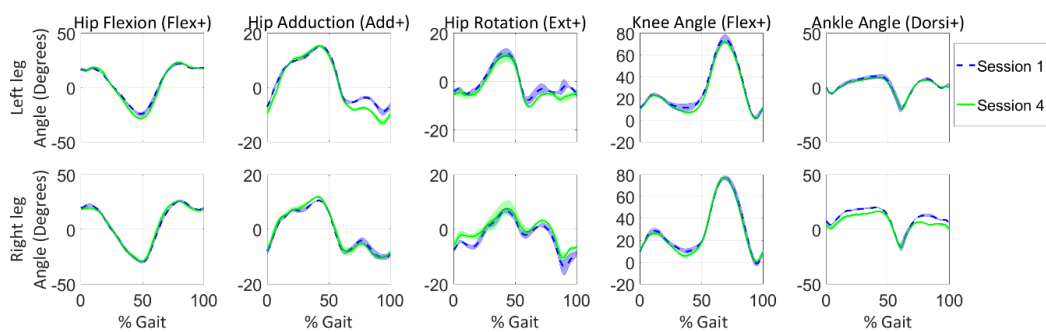


Figure 49: Session comparison of the IK for subject AKP 29

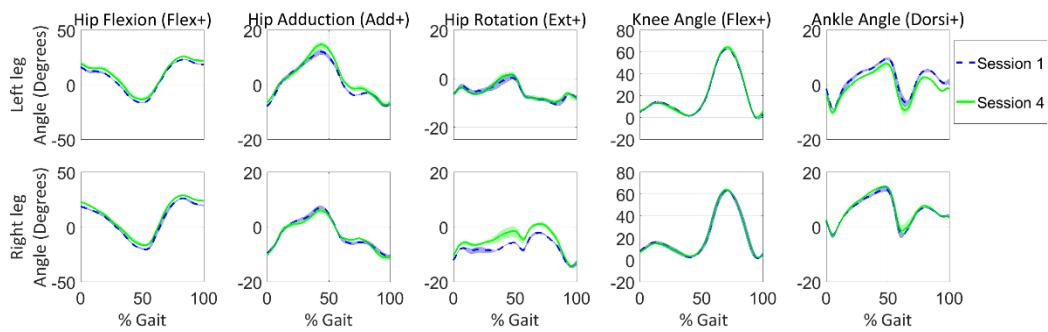


Figure 50: Session comparison of the IK for subject AKP 30

B.2. Inverse Dynamics

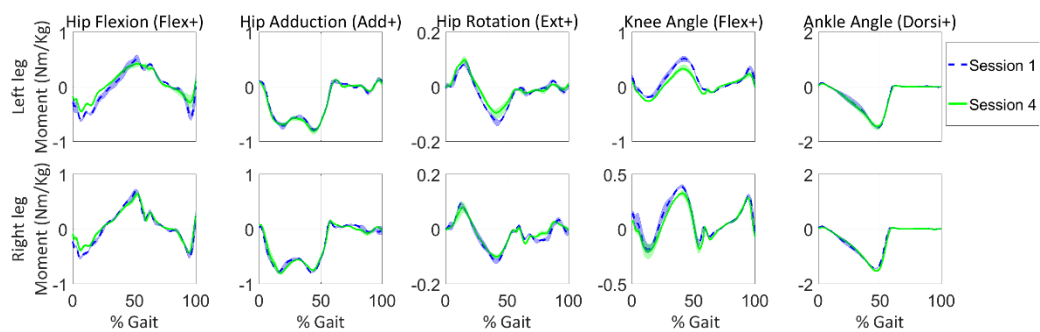


Figure 51: Session comparison of the ID for subject AKP 03

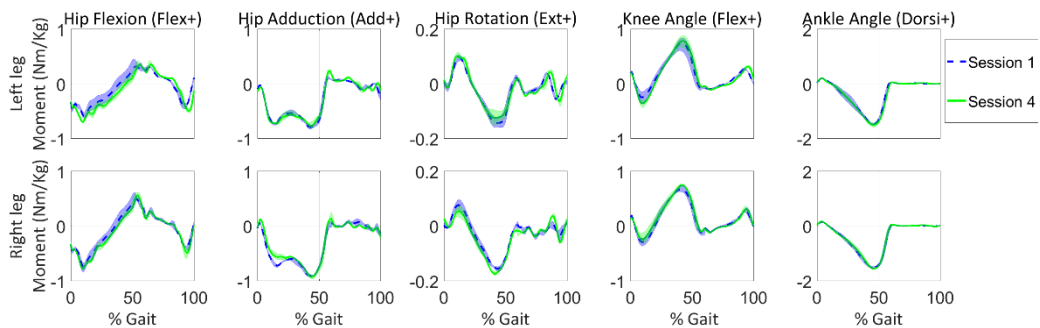


Figure 52: Session comparison of the ID for subject AKP 17

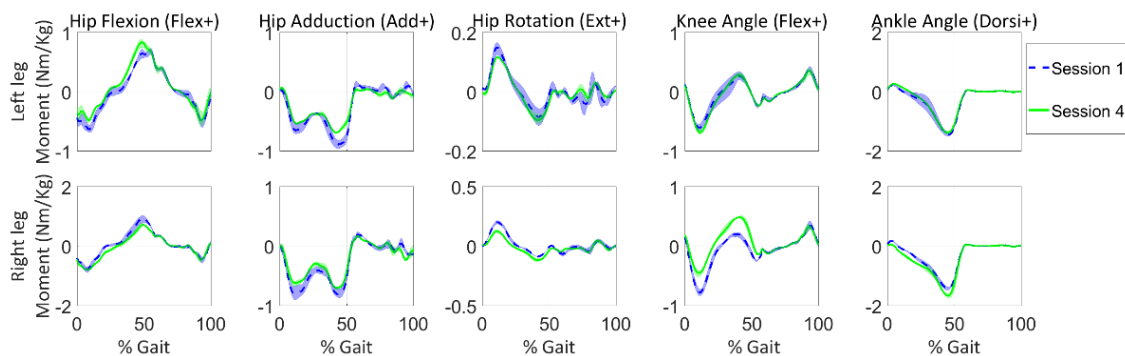


Figure 53: Session comparison of the ID for subject AKP 29

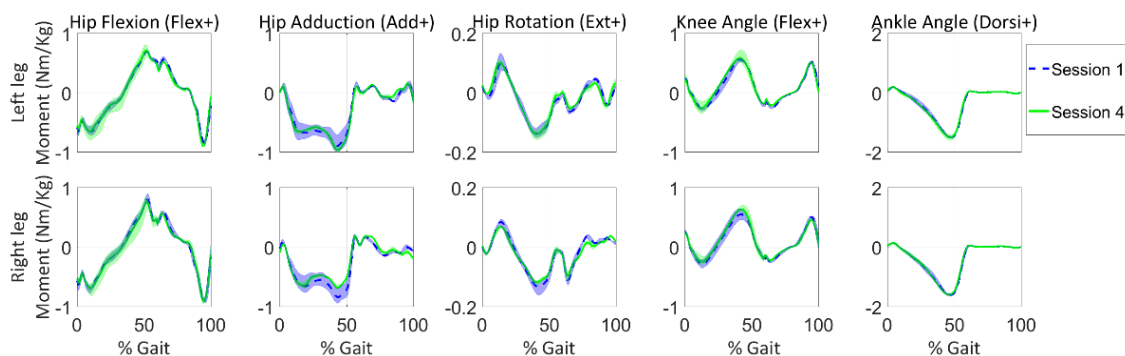


Figure 54: Session comparison of the ID for subject AKP 30

B.3. Force plate and EMG processing

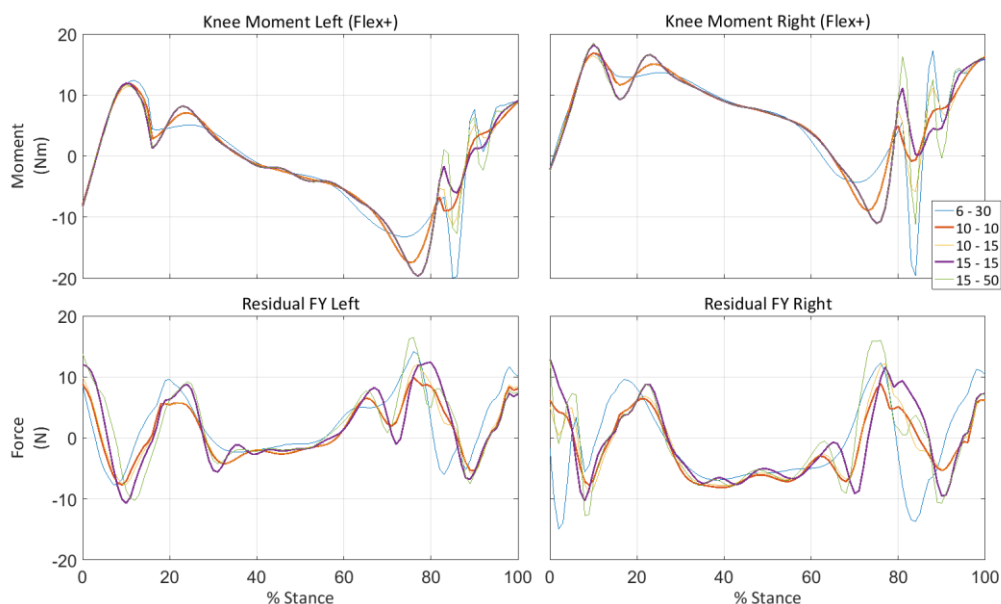


Figure 55: Knee moment and FY residual of AKP 03 session one

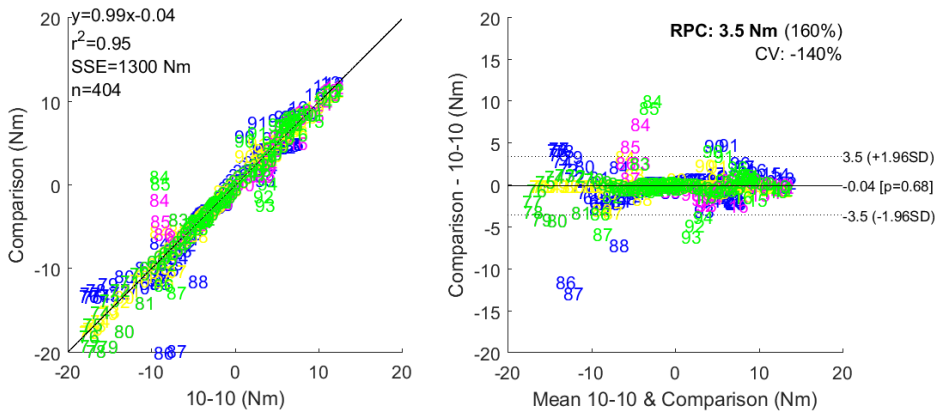


Figure 56: Bland and Altman plot Subject AKP 03 session one left leg

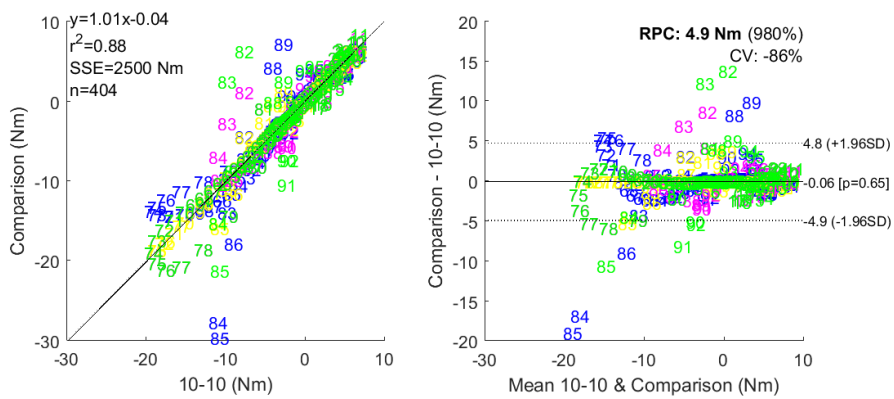


Figure 57: Bland and Altman plot Subject AKP 03 session one right leg

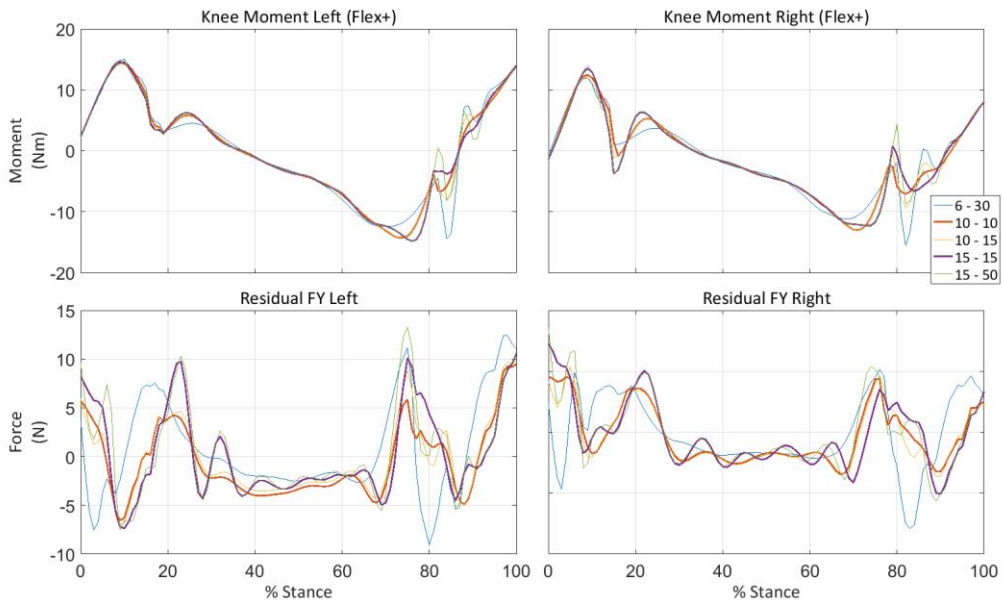


Figure 58: Knee moment and FY residual of AKP03 session four

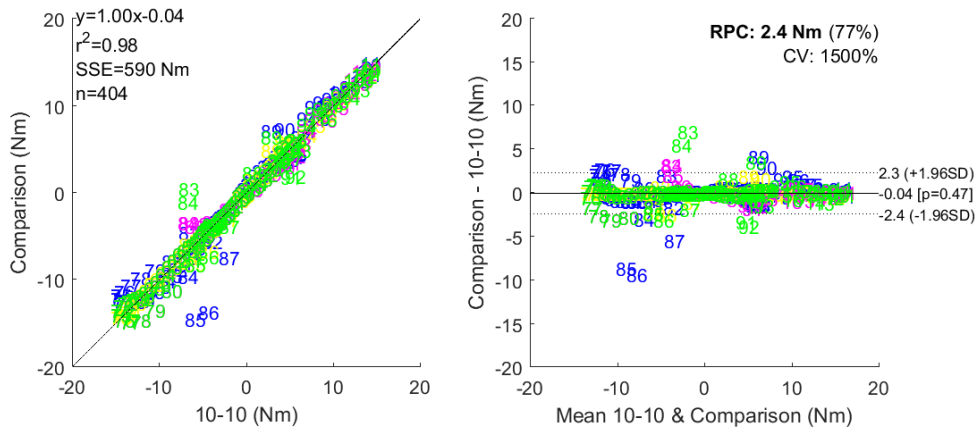


Figure 59: Bland and Altman plot Subject AKP 03 session four left leg

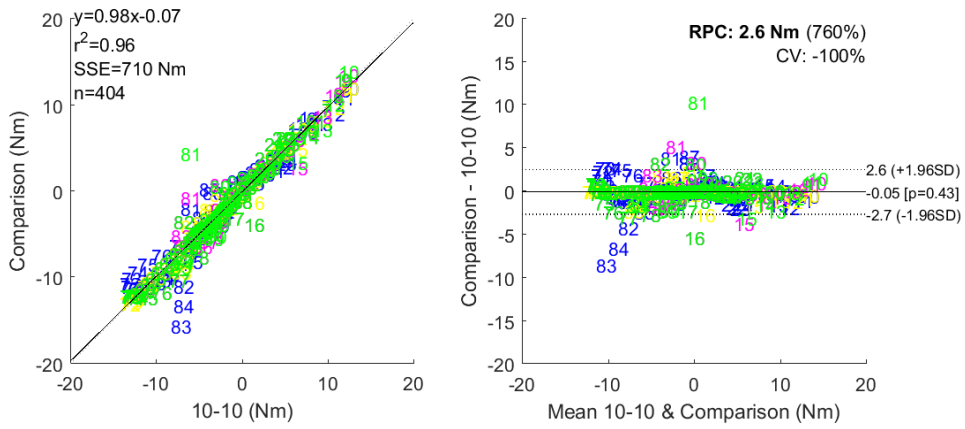


Figure 60: Bland and Altman plot Subject AKP 03 session four right leg

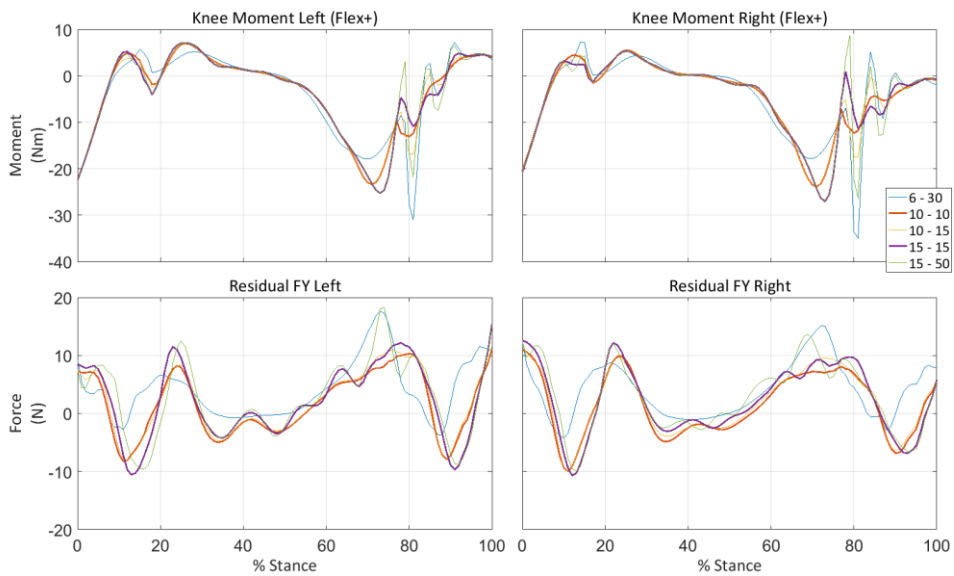


Figure 61: Knee moment and FY residual of AKP 16 session one

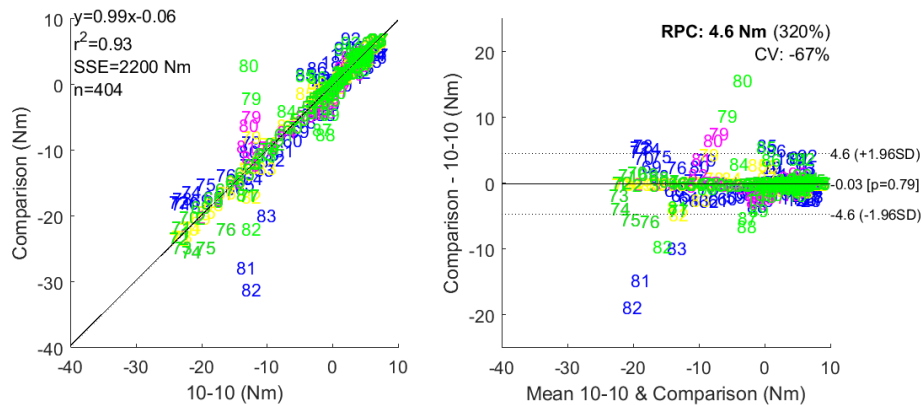


Figure 62: Bland and Altman plot Subject AKP 16 session one left leg

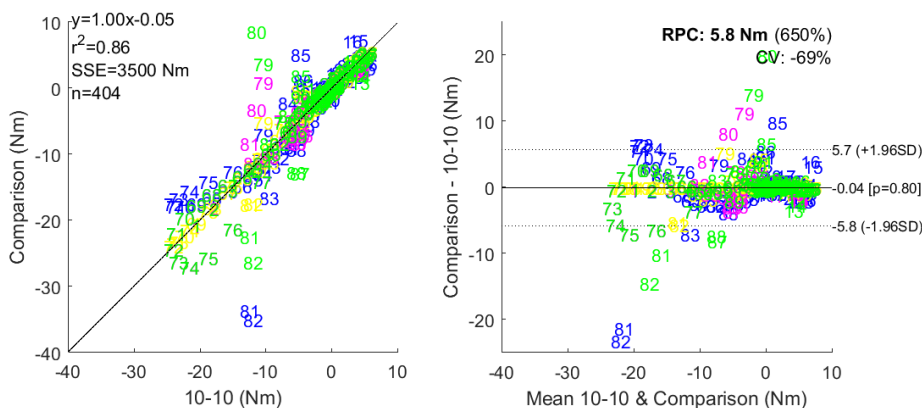


Figure 63: Bland and Altman plot Subject AKP 16 session one right leg

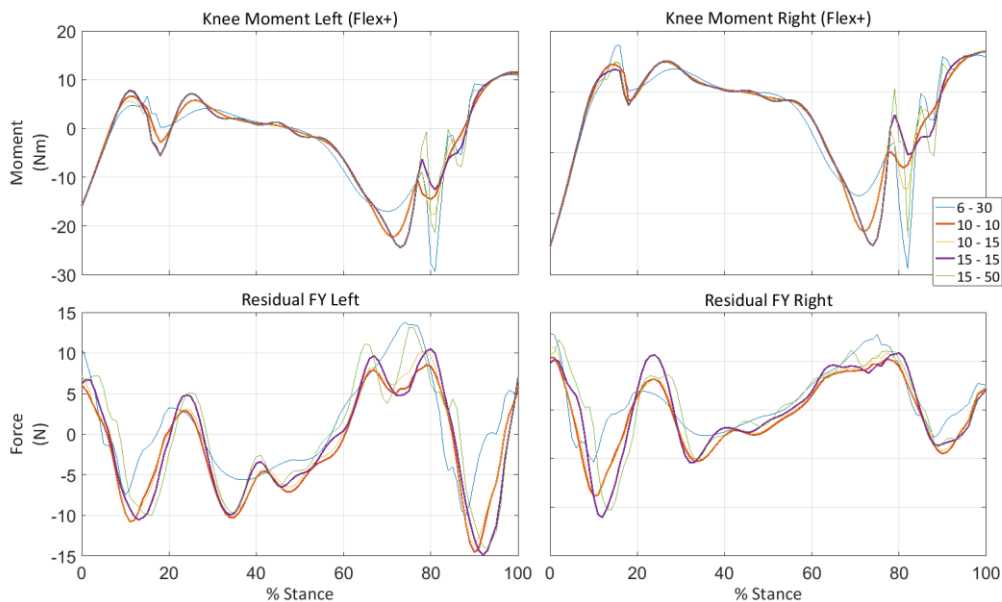


Figure 64: Knee moment and FY residual of AKP 16 session four

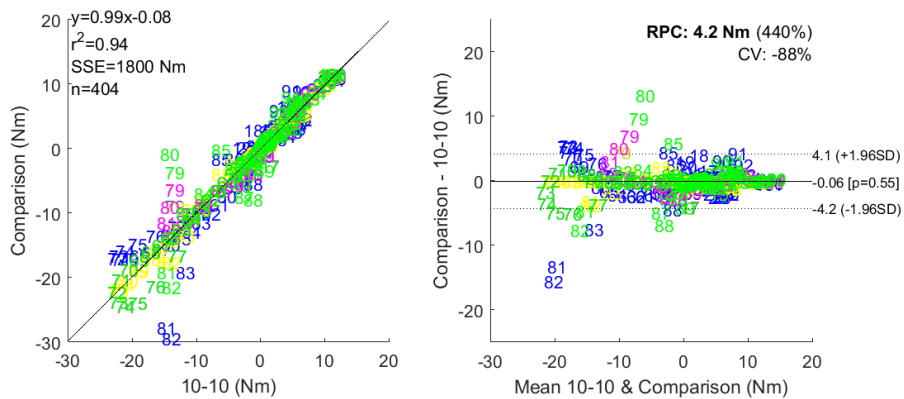


Figure 65: Bland and Altman plot Subject AKP 16 session four left leg

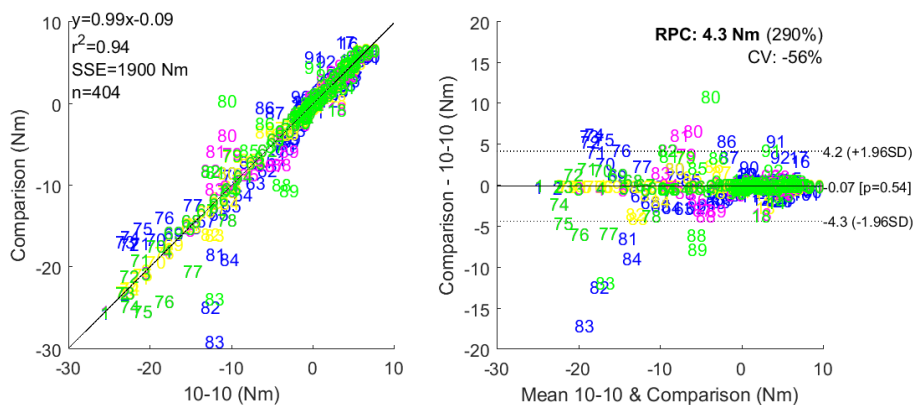


Figure 66: Bland and Altman plot Subject AKP 16 session four right leg

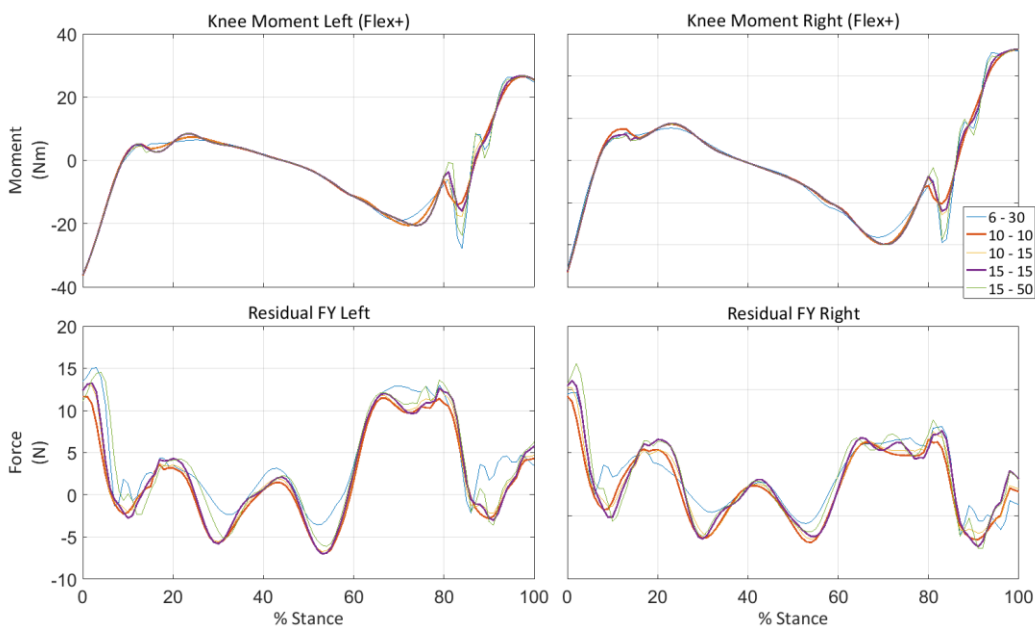


Figure 67: Knee moment and FY residual of AKP 17 session one

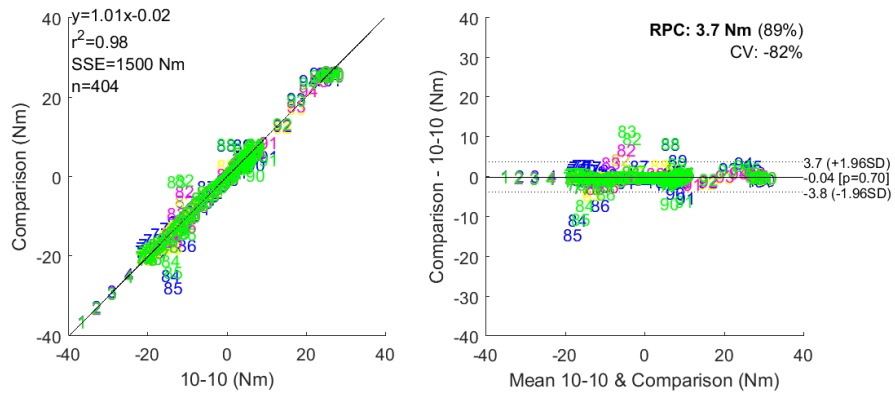


Figure 68: Bland and Altman plot Subject AKP 17 session one left leg

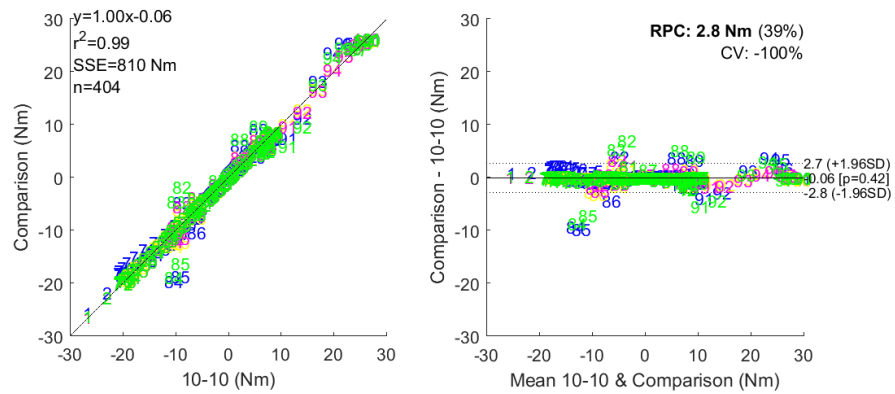


Figure 69: Bland and Altman plot Subject AKP 17 session one right leg

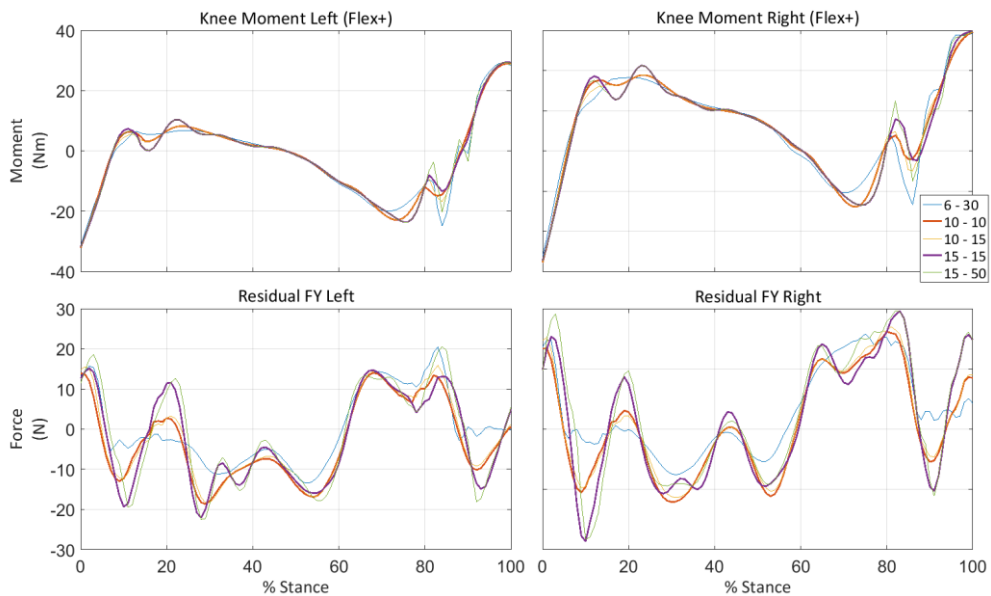


Figure 70: Knee moment and FY residual of AKP17 session four

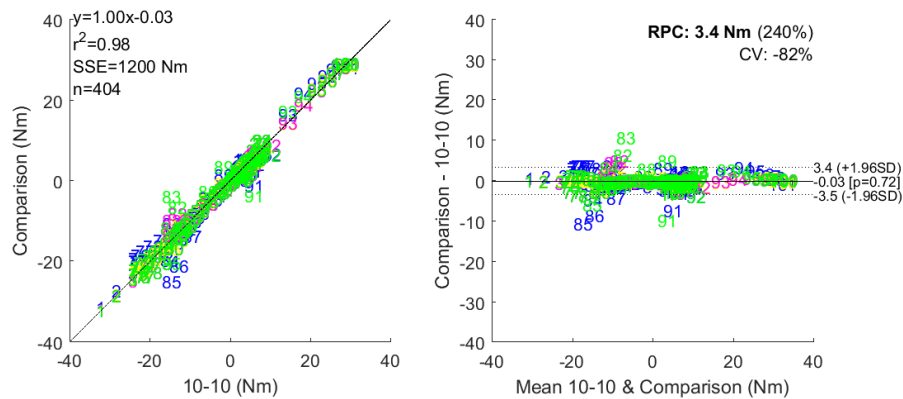


Figure 71: Bland and Altman plot Subject AKP 17 session four left leg

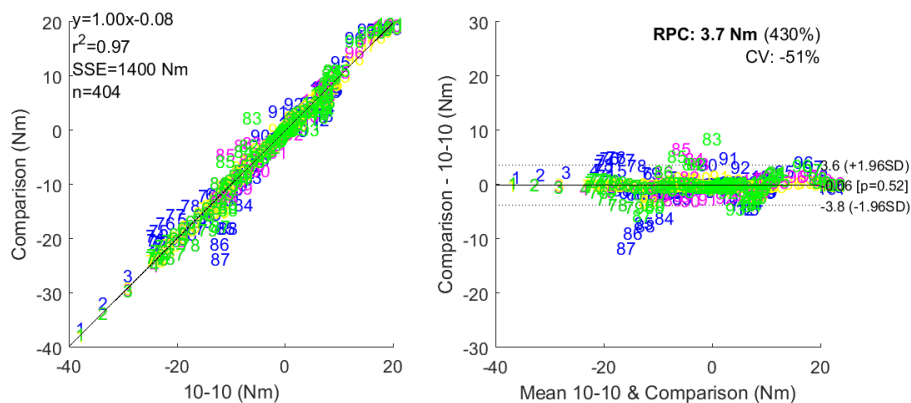


Figure 72: Bland and Altman plot Subject AKP 17 session four right leg

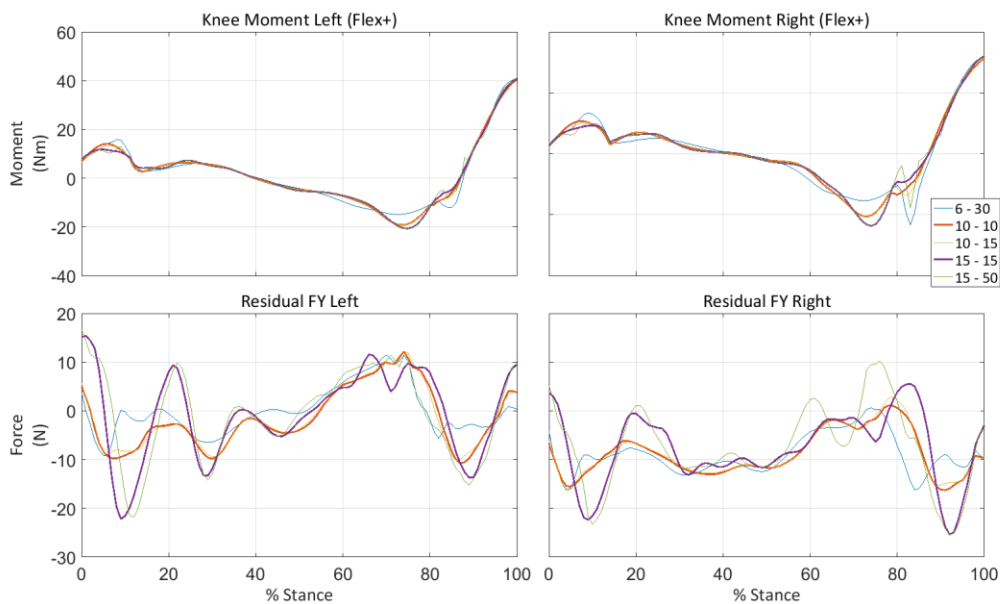


Figure 73: Knee moment and FY residual of AKP29 session one

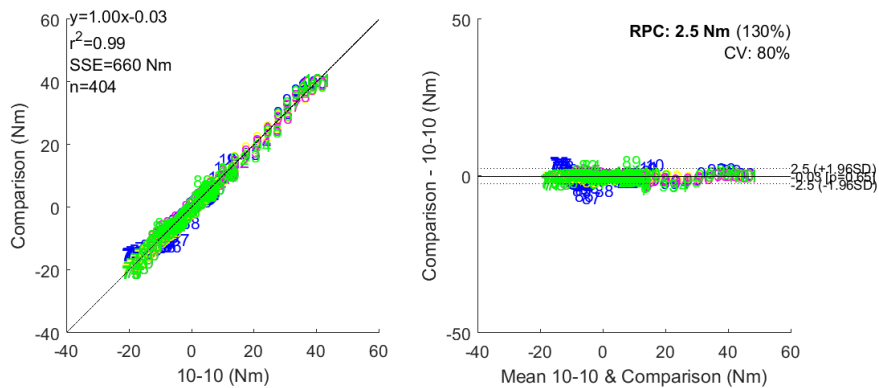


Figure 74: Bland and Altman plot Subject AKP 29 session one left leg

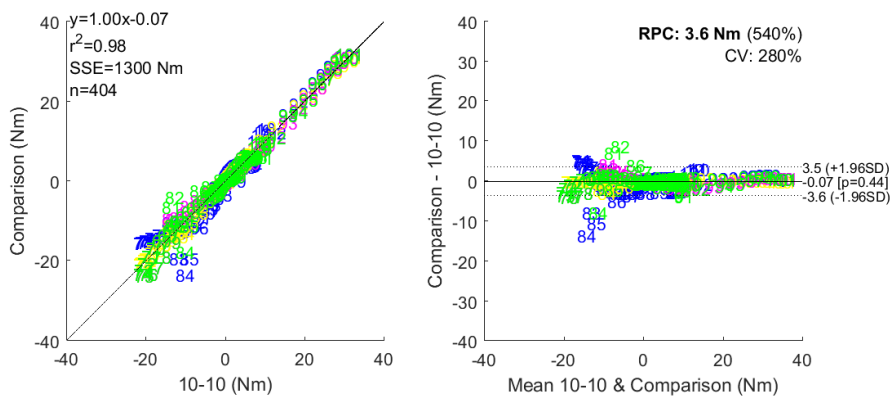


Figure 75: Bland and Altman plot Subject AKP 29 session one right leg

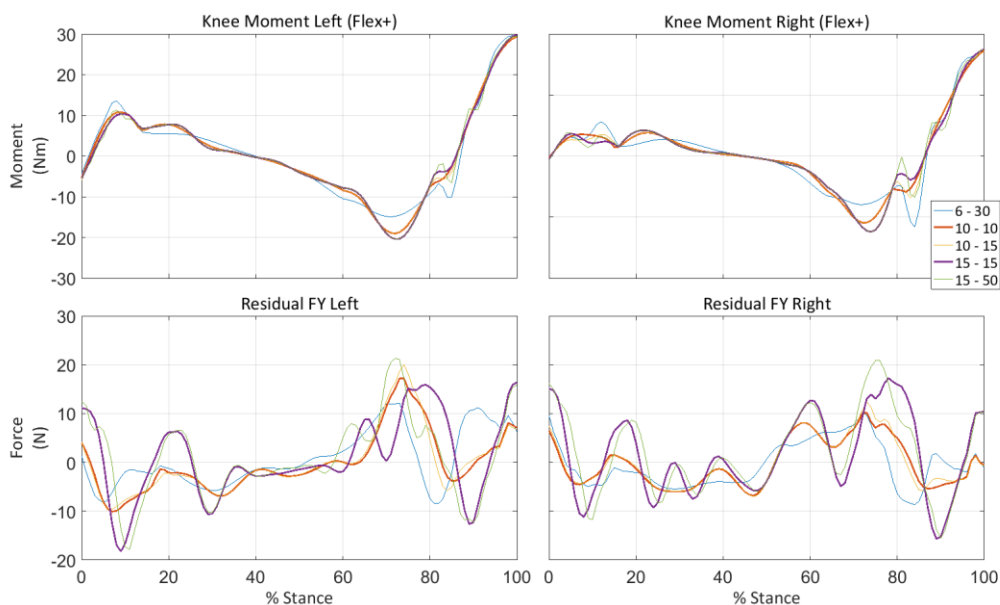


Figure 76: Knee moment and FY residual of AKP29 session four

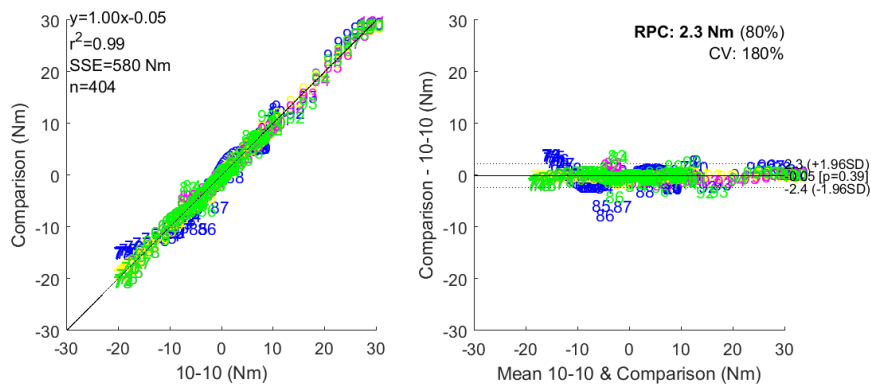


Figure 77: Bland and Altman plot Subject AKP 29 session four left leg

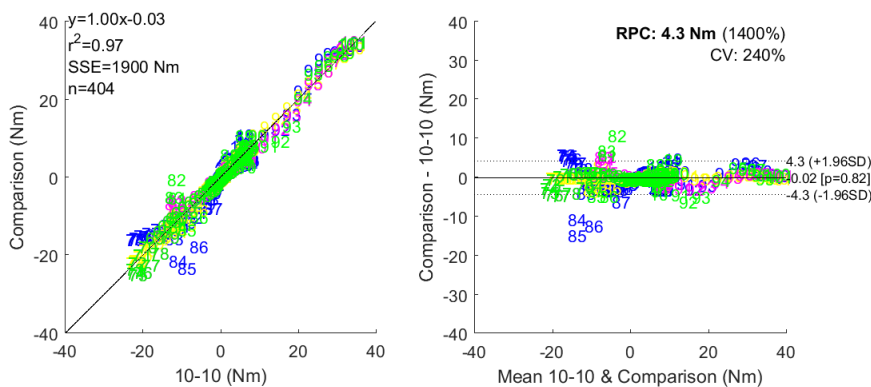


Figure 78: Bland and Altman plot Subject AKP 29 session four right leg

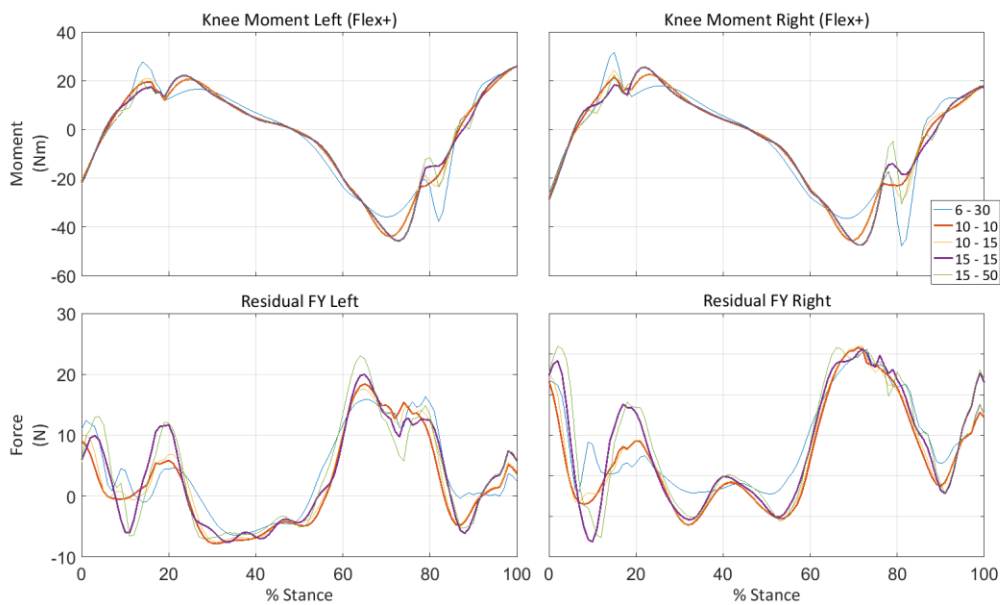


Figure 79: Knee moment and FY residual of AKP30 session one

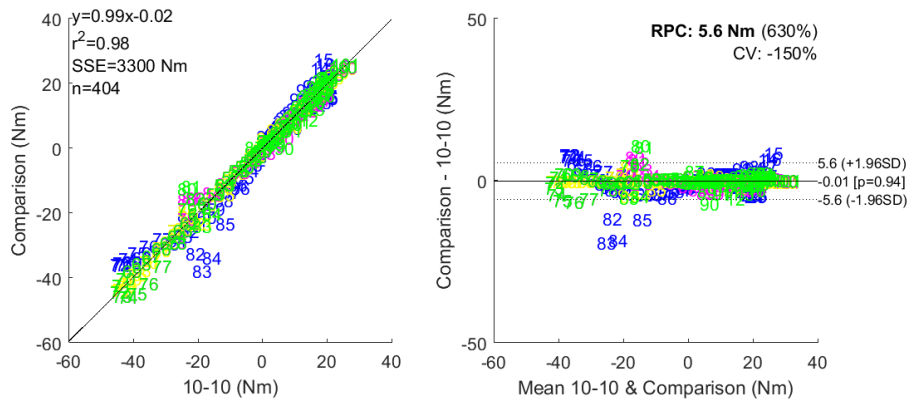


Figure 80: Bland and Altman plot Subject AKP 30 session one left leg

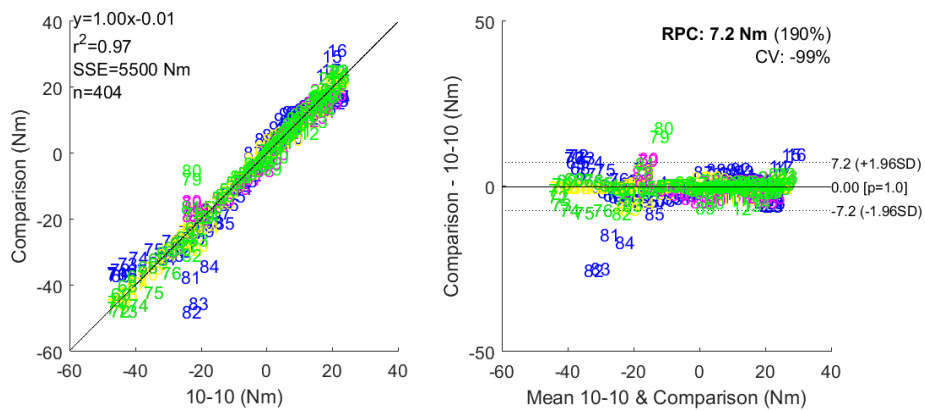


Figure 81: Bland and Altman plot Subject AKP 30 session one right leg

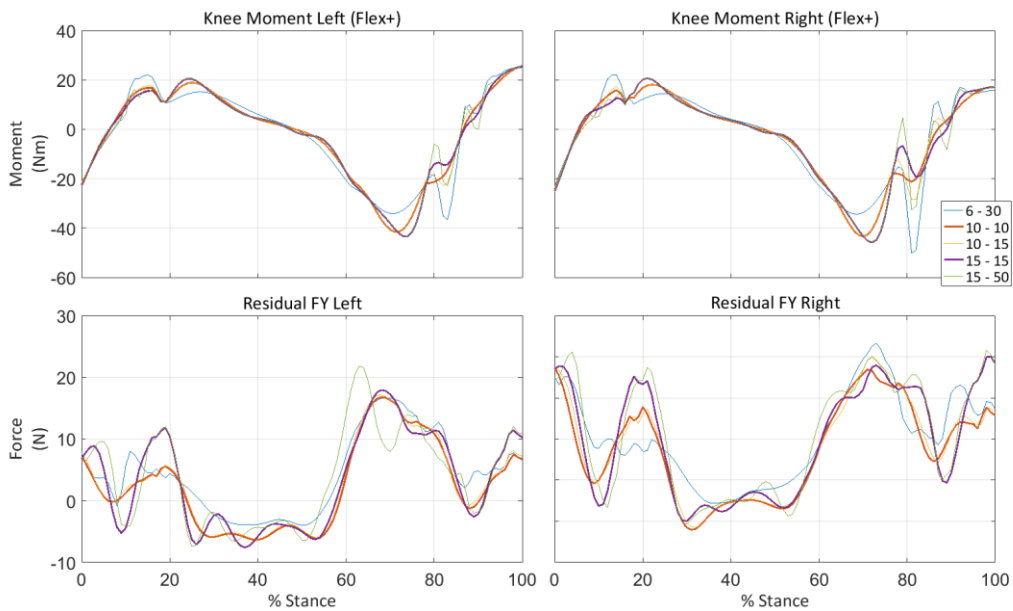


Figure 82: Knee moment and FY residual of AKP30 session four

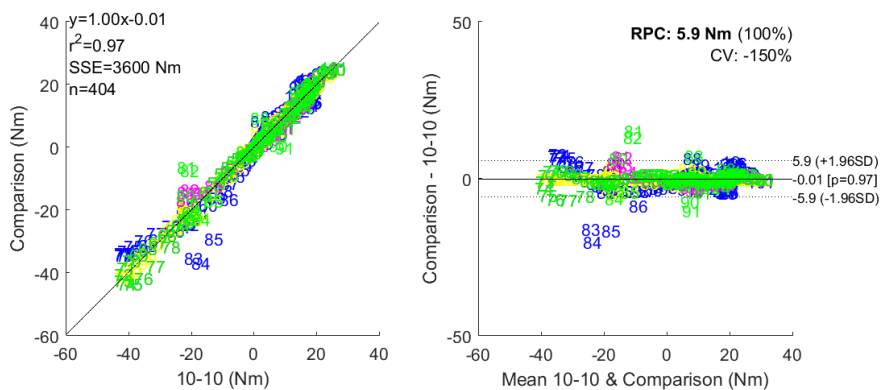


Figure 83: Bland and Altman plot Subject AKP 30 session four left leg

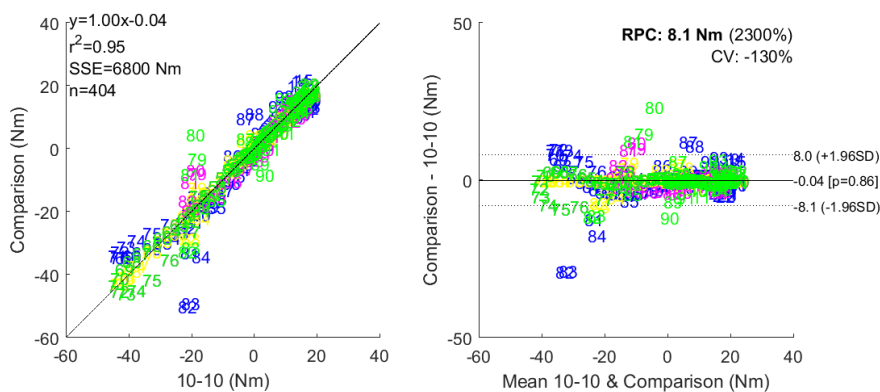


Figure 84: Bland and Altman plot Subject AKP 30 session four right leg

B.4. Kinematics comparison

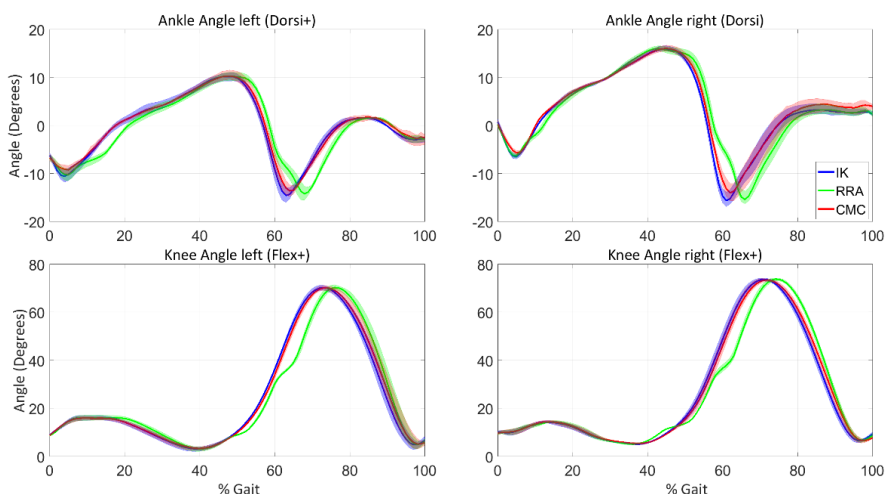


Figure 85: AKP 03 Session one kinematics comparison

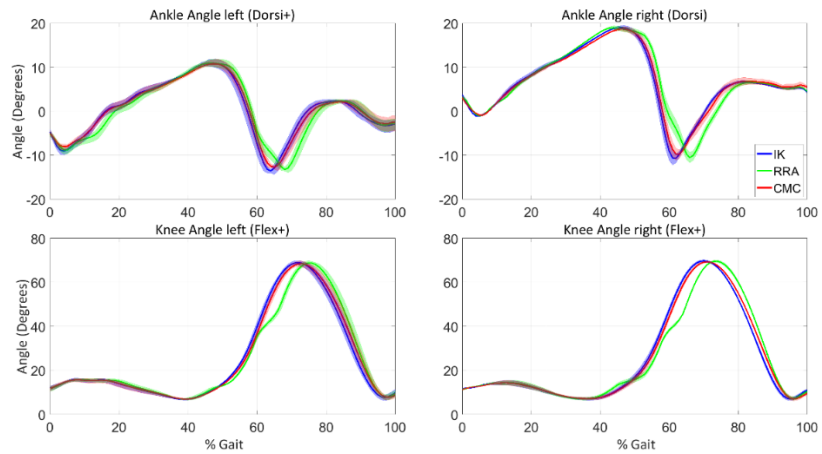


Figure 86: AKP 03 Session four kinematics comparison

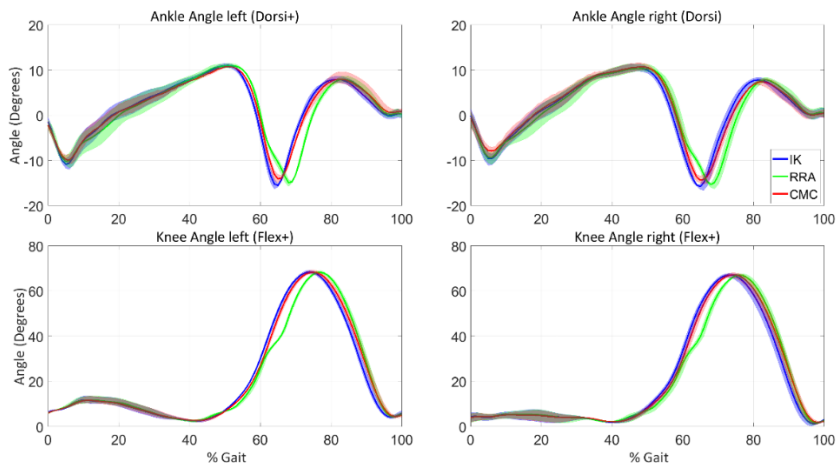


Figure 87: AKP 16 Session one kinematics comparison

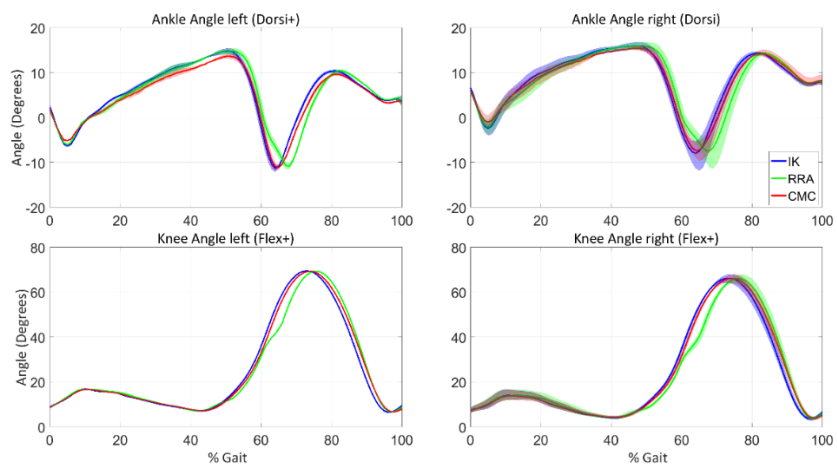


Figure 88: AKP 16 Session four kinematics comparison

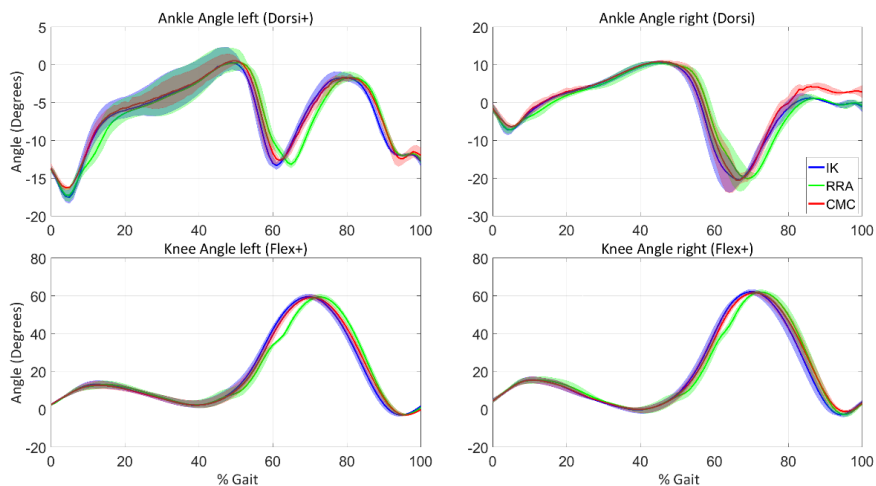


Figure 89: AKP 17 Session one kinematics comparison

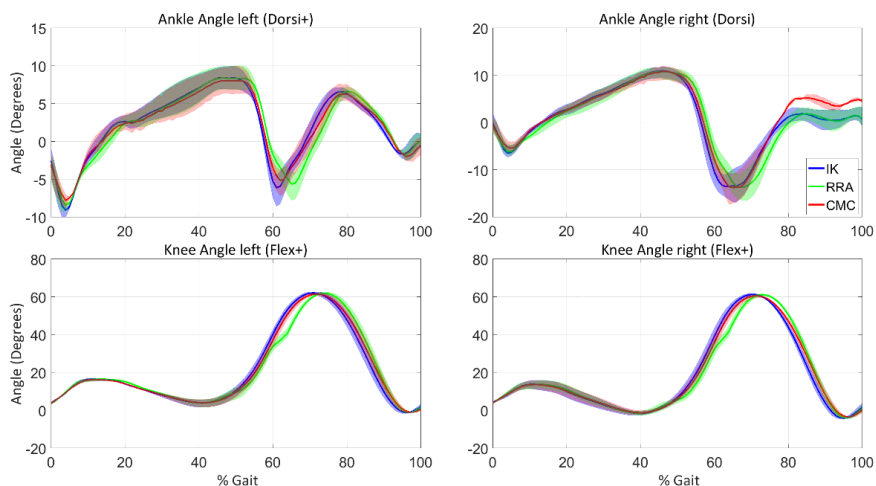


Figure 90: AKP 17 Session four kinematics comparison

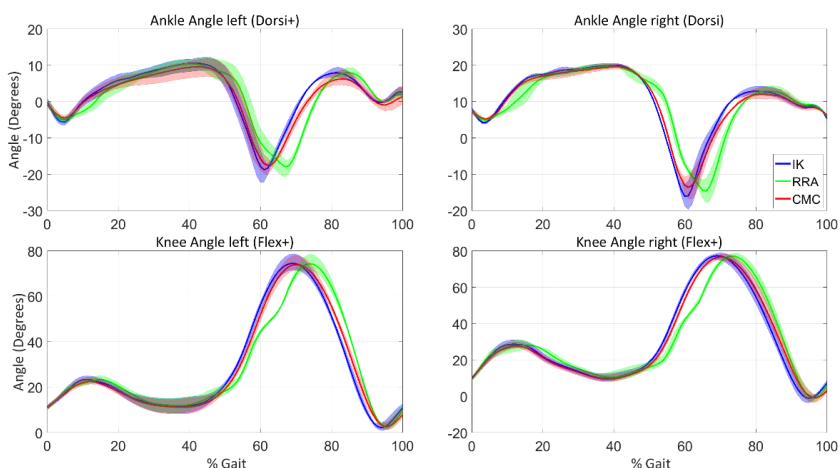


Figure 91: AKP 29 Session one kinematics comparison

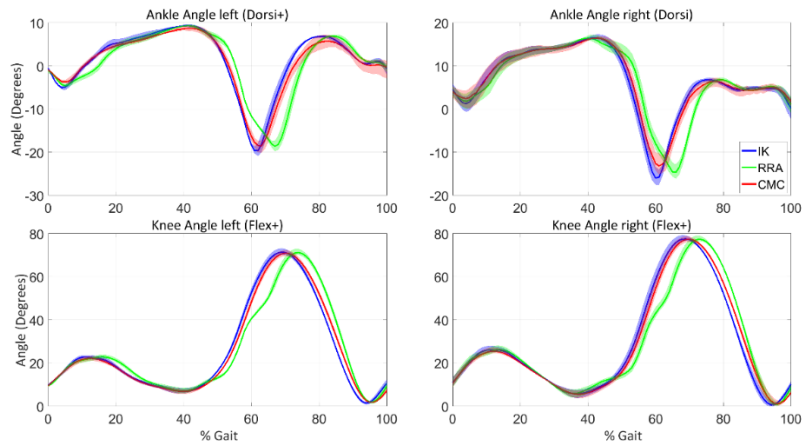


Figure 92: AKP 29 Session four kinematics comparison

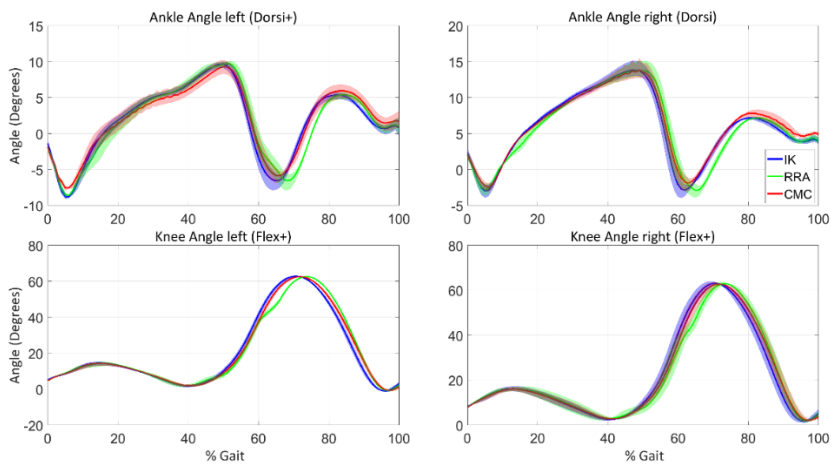


Figure 93: AKP 30 Session one kinematics comparison

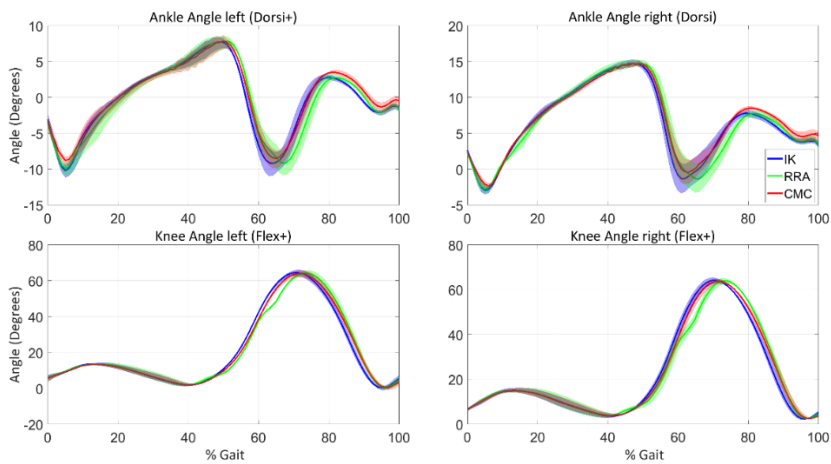


Figure 94: AKP 30 Session four kinematics comparison

Appendix C. Simulated Annealing

Step 0:

Set $x = x_0$
 Compute $f_0 = f(x)$
 Set $x_{opt} = x_0$
 Set $f_{opt} = f_0$

Step 1:

Starting from x_i , generate a random point x' along the direction h :

$$x' = x_i + r v_{m_h} e_h$$

where r is a pseudorandom number generated in the range $[-1,1]$, e_h is the vector of the h th coordinate direction and v_{m_h} is the component of the step vector V_m along the same direction.

Step 2:

Compute $f' = f(x')$
 If $f' \leq f_i$, then accept the new point:

Set $x_{i+1} = x'$,
 Set $f_{i+1} = f'$,
 Add 1 to i ,
 If $f' < f_{opt}$, then set
 $x_{opt} = x'$,
 $f_{opt} = f'$
 end If.

else if $f' > f_i$ accept or reject the point using the Metropolis criterion with the value,

$$p = \exp\left(\frac{f_i - f'}{T_k}\right),$$

In the case of acceptance,

set $x_{i+1} = x'$,
 set $f_{i+1} = f'$,
 add 1 to i
 add 1 to n_h .

Step 3:

Add 1 to h .
 If $h \leq n$, then go back to step 1,
 Else set h to 1 and add 1 to j .

Step 4:

If $j < N_s$, then go back to step 1,
 else update the step vector V_m :

For each direction u the new step vector component V'_u is:

$$v'_u = v_{m_u} \left(1 + c_u \frac{\frac{n_u - 0.6}{N_s}}{0.4} \right), \text{ if } n_u > 0.6N_s,$$

$$v'_u = \frac{v_{m_u}}{1 + c_u \frac{0.4 - n_u/N_s}{0.4}}, \text{ if } n_u < 0.4N_s,$$

$$v'_u = v_{m_u} \text{ otherwise,}$$

Set $V_{m+1} = V'$,

Set $j = 0$,

Set $n_u = 0, \quad u = 1, \dots, n$,

Add 1 to m .

Step 5:

If $m < N_T$, then go back to step 1,

Else, reduce the temperature T_k ,

$$\text{Set } T_{k+1} = r_T \cdot T_k,$$

$$\text{Set } f_k^* = f_i,$$

Add 1 to k

Set m to 0.

Step 6:

If:

$$|f_k^* - f_{k-u}^*| \leq \epsilon, \quad u = 1, \dots, N_\epsilon$$

$$f_k^* - f_{opt} \leq \epsilon$$

then stop the search,

else:

add 1 to i ,

$$\text{set } X_i = X_{opt},$$

$$\text{set } f_i = f_{opt}$$

Go to step 1

The parameters which control the simulated annealing are listed with their default values as follows:

$$N_s = 15$$

$$N_T = 5$$

$$r_T = 0.85$$

$$N_\epsilon = 4$$

$$\epsilon = 0.001$$

$$T = 200000$$

Appendix D. EMG processing

D.1. EMG processing results

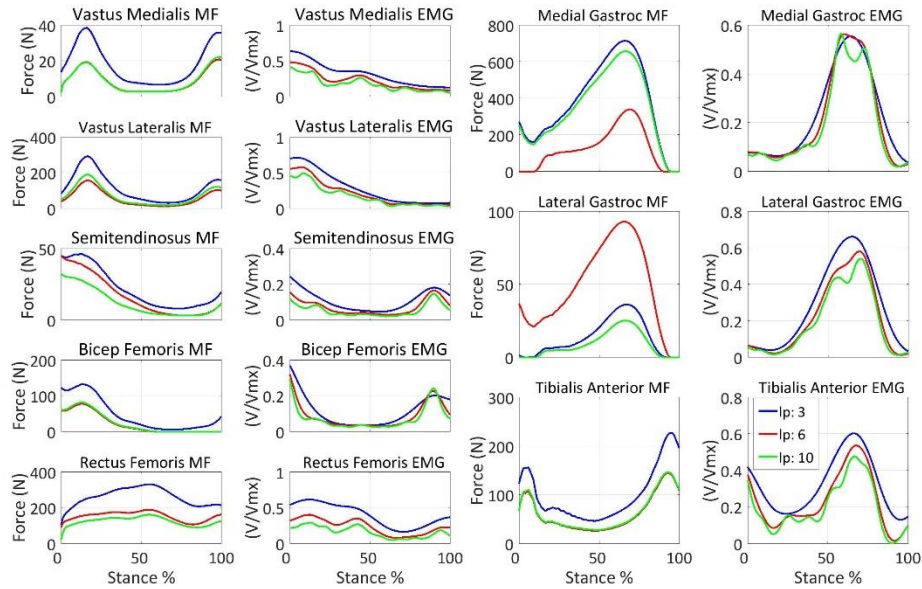


Figure 95: Muscle forces and EMGs of AKP 29 filtered at a high-pass cut-off of 30 Hz for the affected leg (left) during session one

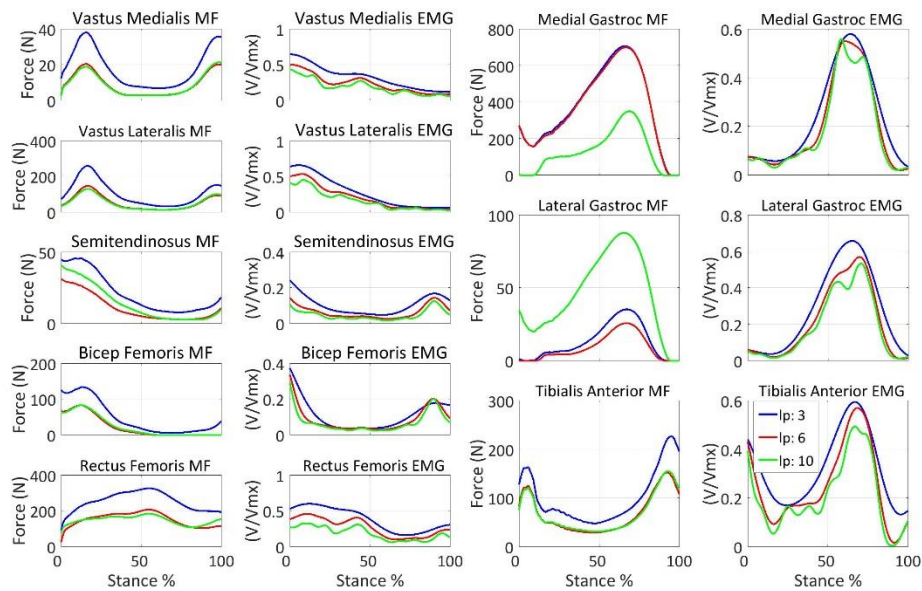


Figure 96: Muscle forces and EMGs of AKP 29 filtered at a high-pass cut-off of 40 Hz for the affected leg (left) during session one

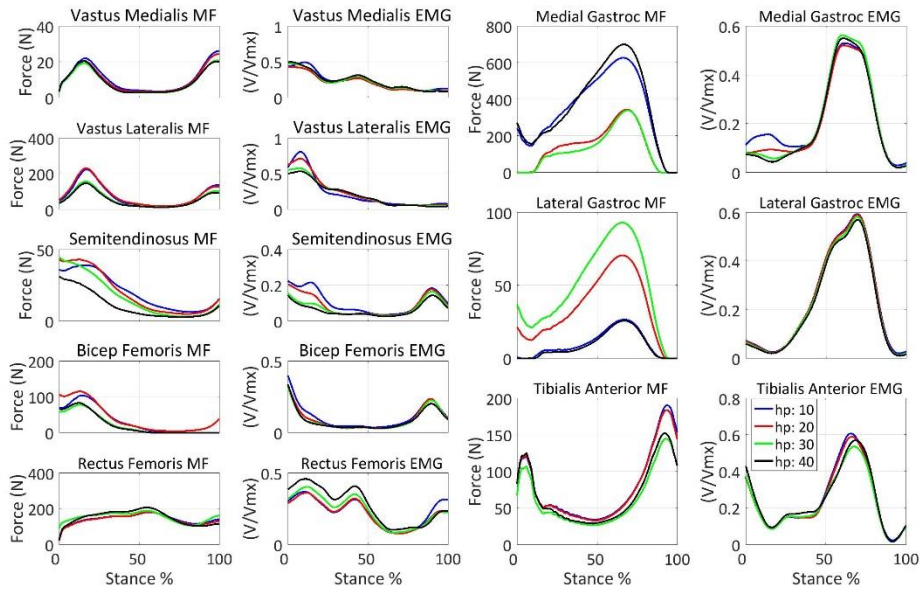


Figure 97: Muscle forces and EMGs of AKP 29 filtered at a low-pass cut-off of 6 Hz for the affected leg (left) during session one

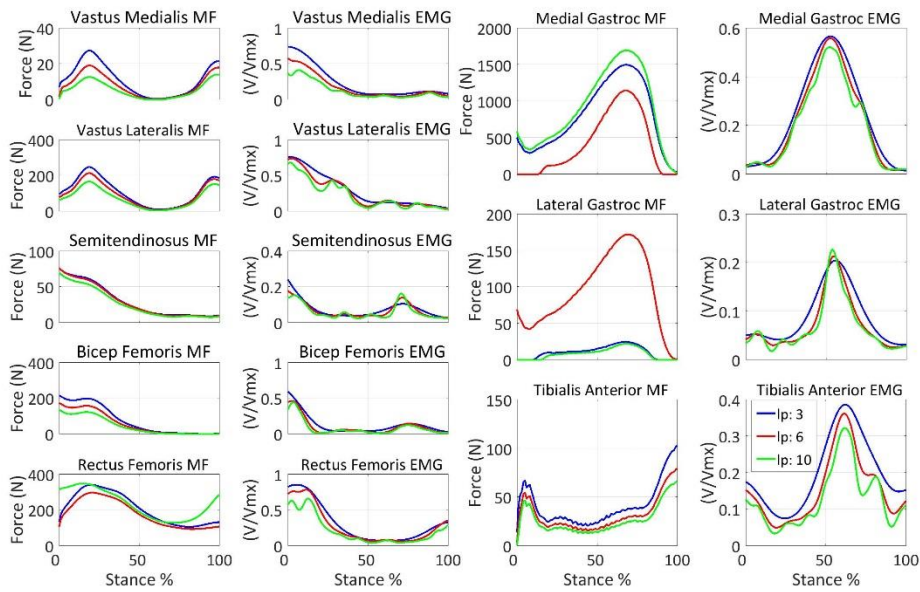


Figure 98: Muscle forces and EMGs of AKP 30 filtered at a high-pass cut-off of 30 Hz for the affected leg (left) during session one

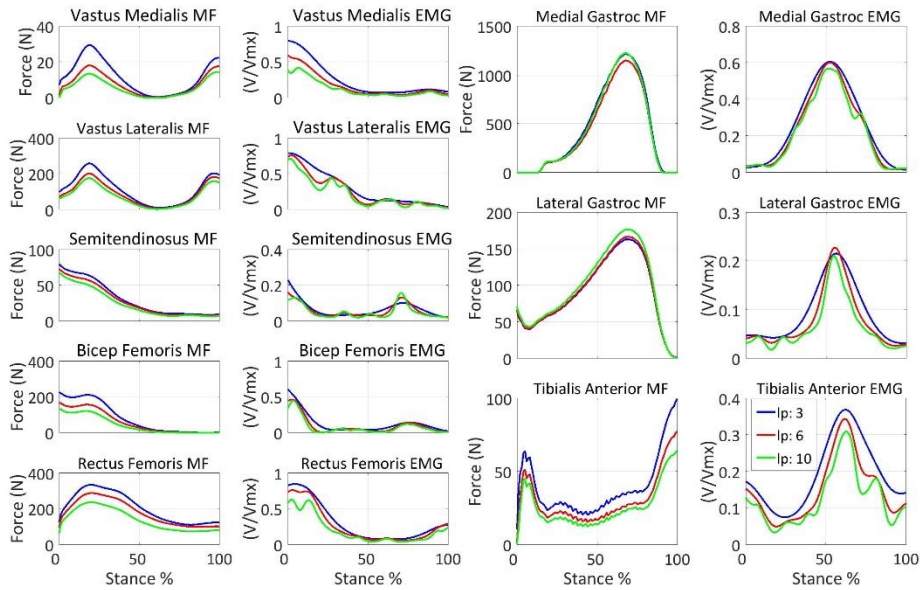


Figure 99: Muscle forces and EMGs of AKP 30 filtered at a high-pass cut-off of 40 Hz for the affected leg (left) during session one

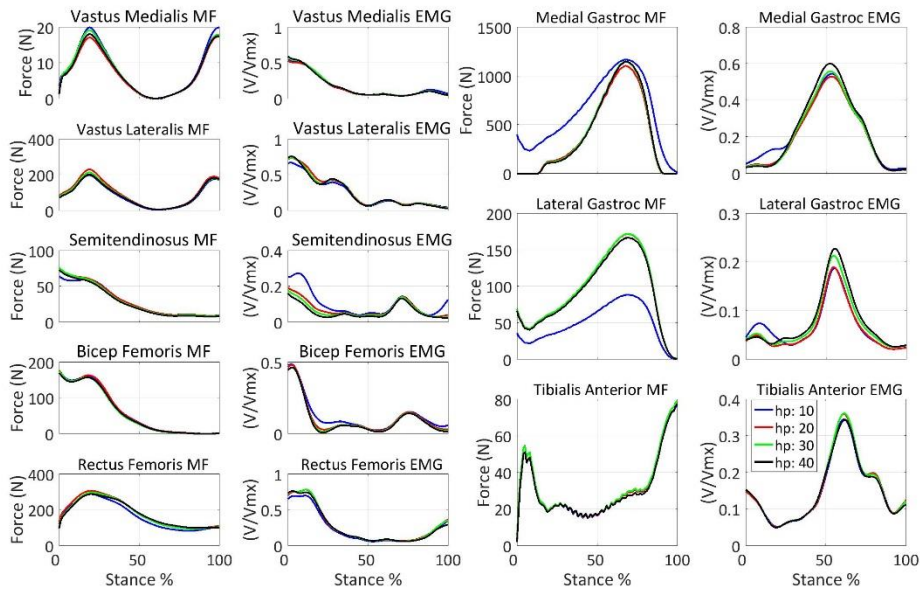


Figure 100: Muscle forces and EMGs of AKP 30 filtered at a low-pass cut-off of 6 Hz for the affected leg (left) during session one

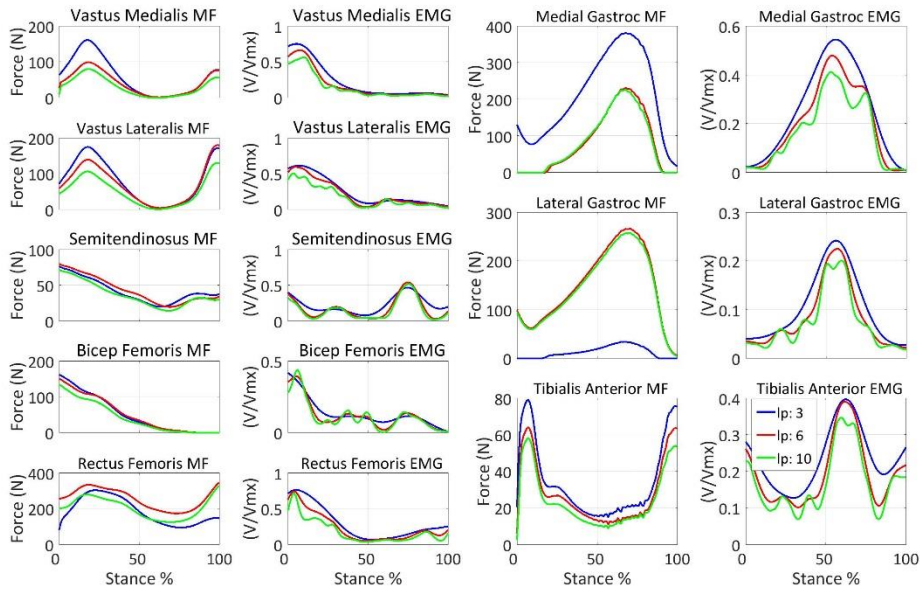


Figure 101: Muscle forces and EMGs of AKP 30 filtered at a high-pass cut-off of 30 Hz for the unaffected leg (right) during session one

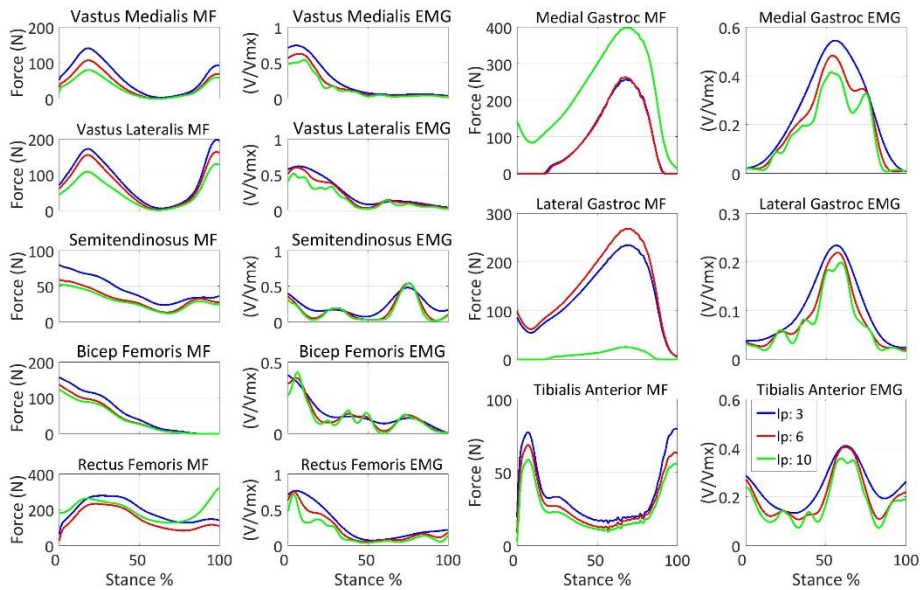


Figure 102: Muscle forces and EMGs of AKP 30 filtered at a high-pass cut-off of 40 Hz for the unaffected leg (right) during session one

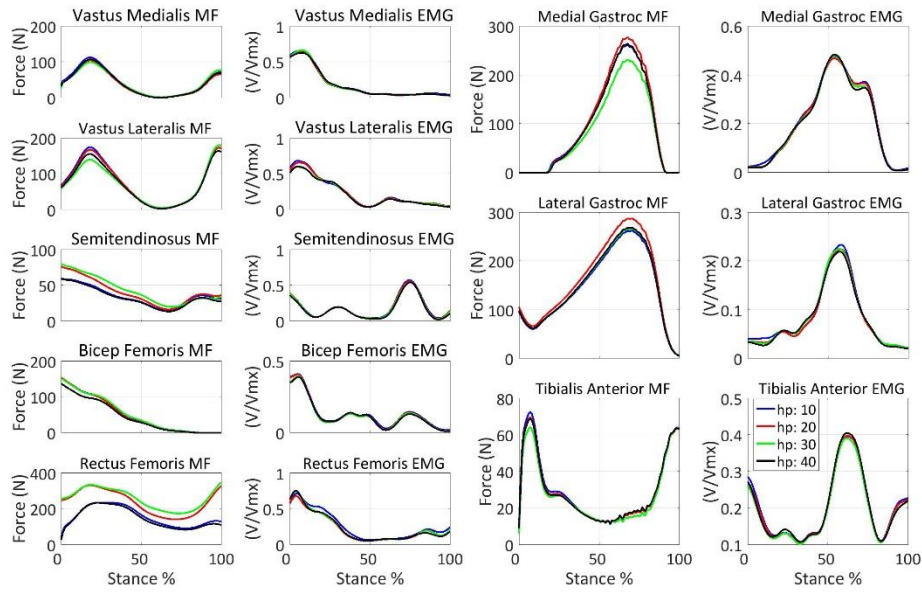


Figure 103: Muscle forces and EMGs of AKP 30 filtered at a low-pass cut-off of 6 Hz for the unaffected leg (right) during session one

D.2. EMG normalisation results

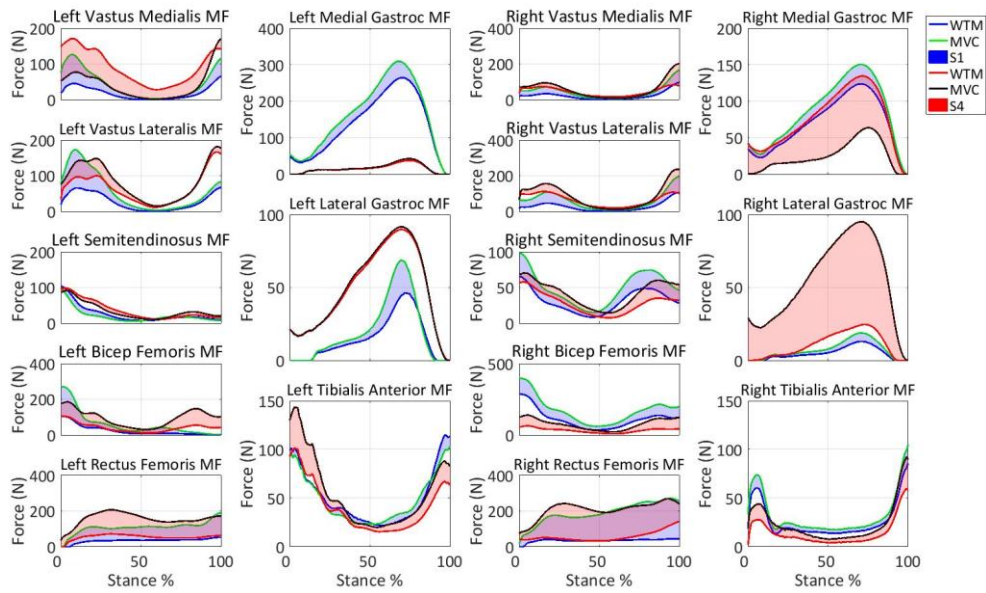


Figure 104: AKP 03 WTM vs MVC normalisation

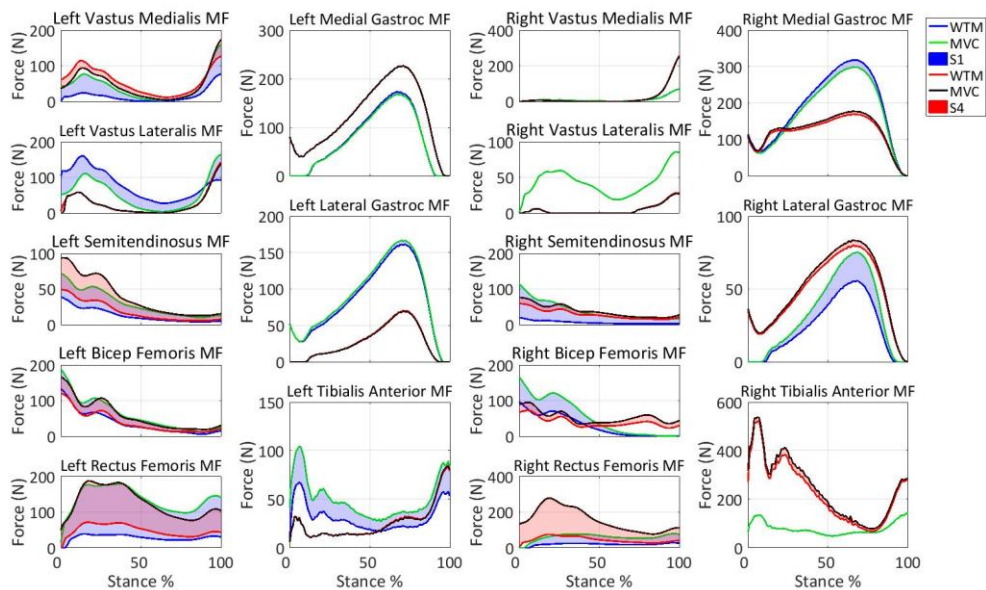


Figure 105: AKP 16 WTM vs MVC normalisation

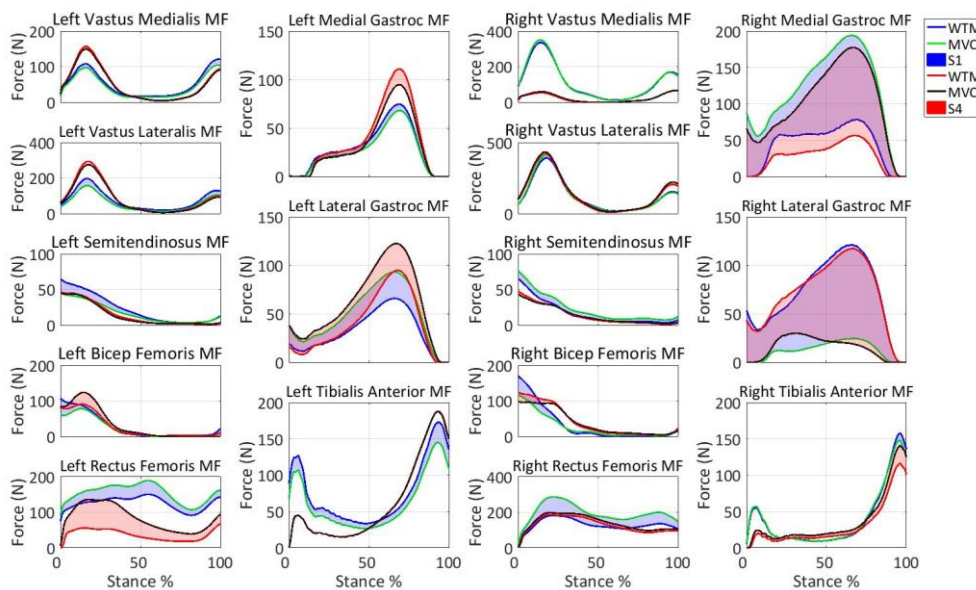


Figure 106: Muscle forces for AKP 29 using EMGs normalised using MVC vs WTM

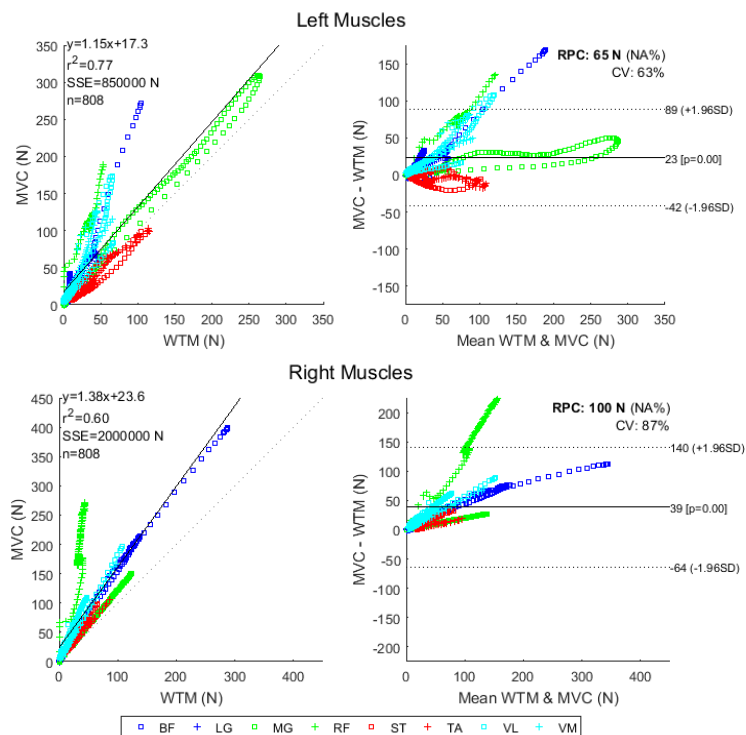


Figure 107: BA plot for AKP 03 session one normalisation muscle forces

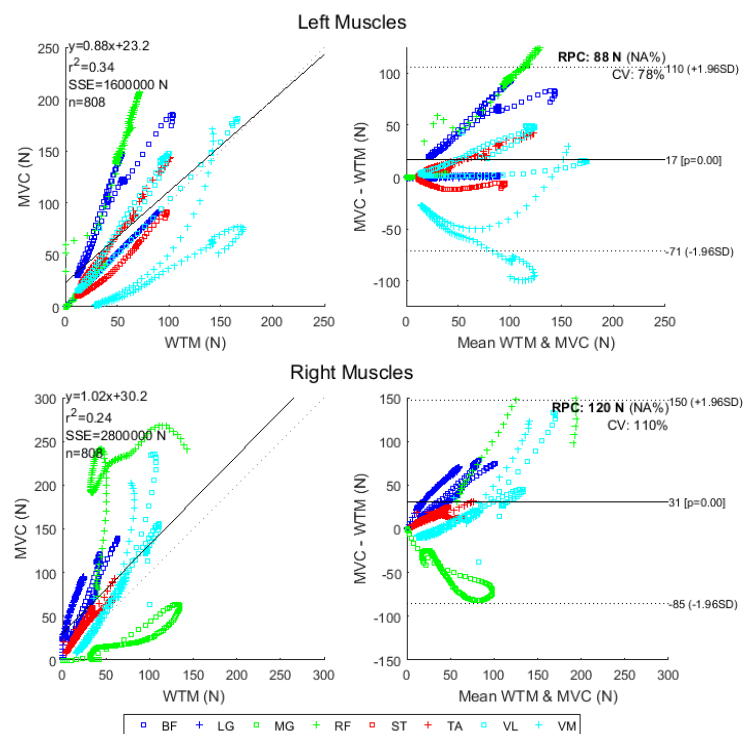


Figure 108: BA plot for AKP 03 session four normalisation muscle forces

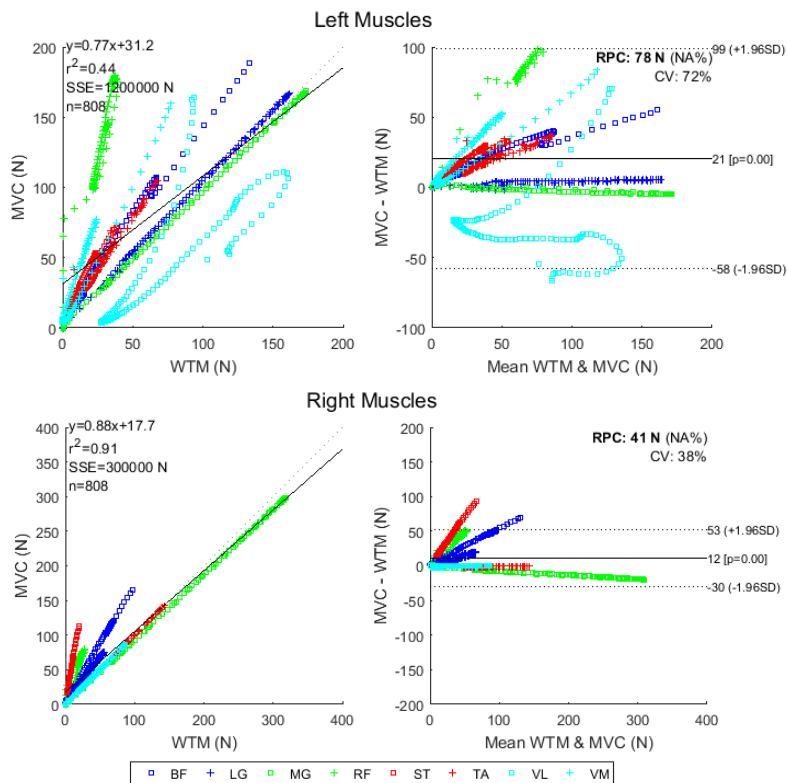


Figure 109: BA plot for AKP 16 session one normalisation muscle forces

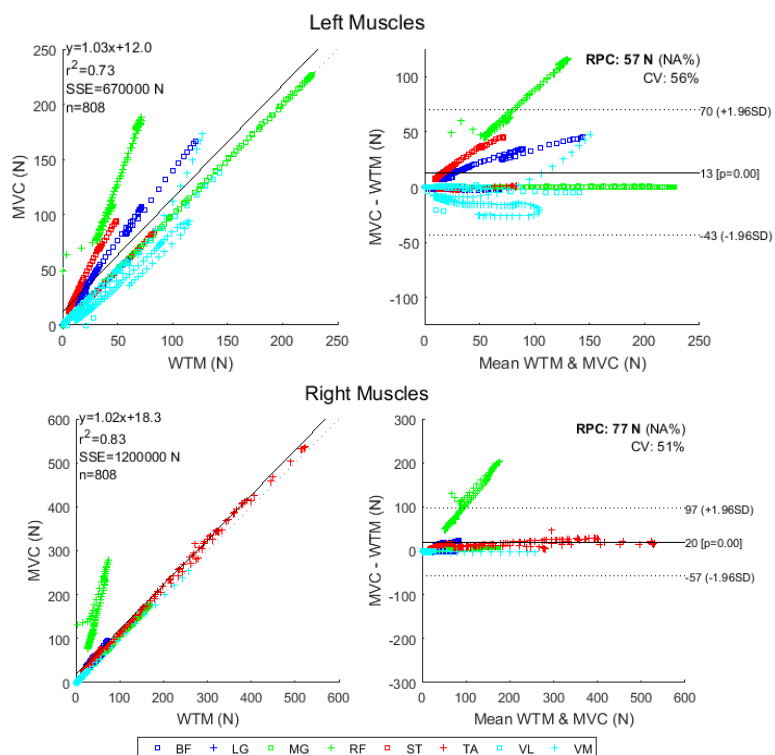


Figure 110: BA plot for AKP 16 session four normalisation muscle forces

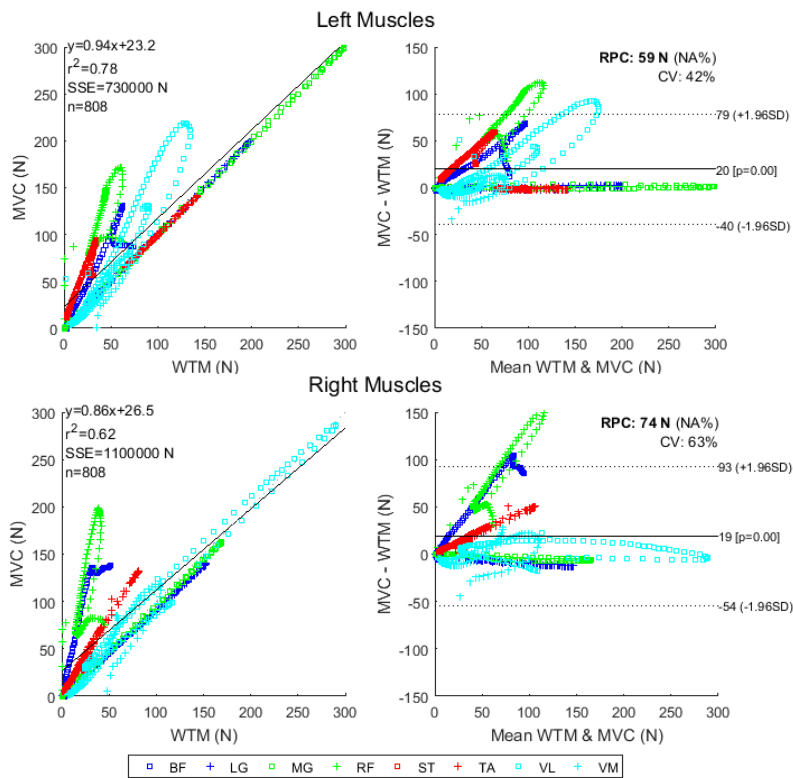


Figure 111: BA plot for AKP 17 session one normalisation muscle forces

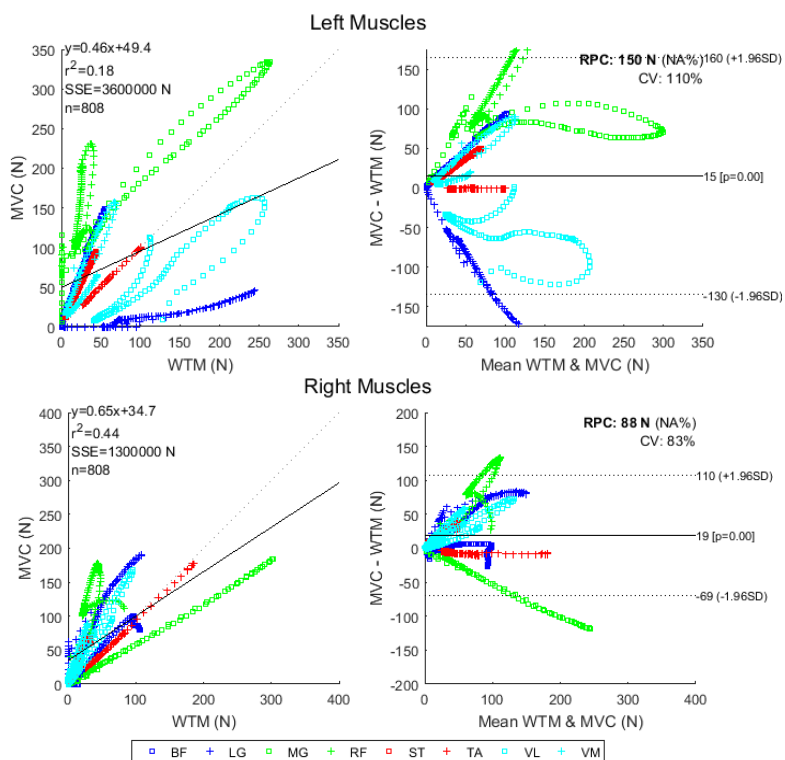


Figure 112: BA plot for AKP 17 session four normalisation muscle forces

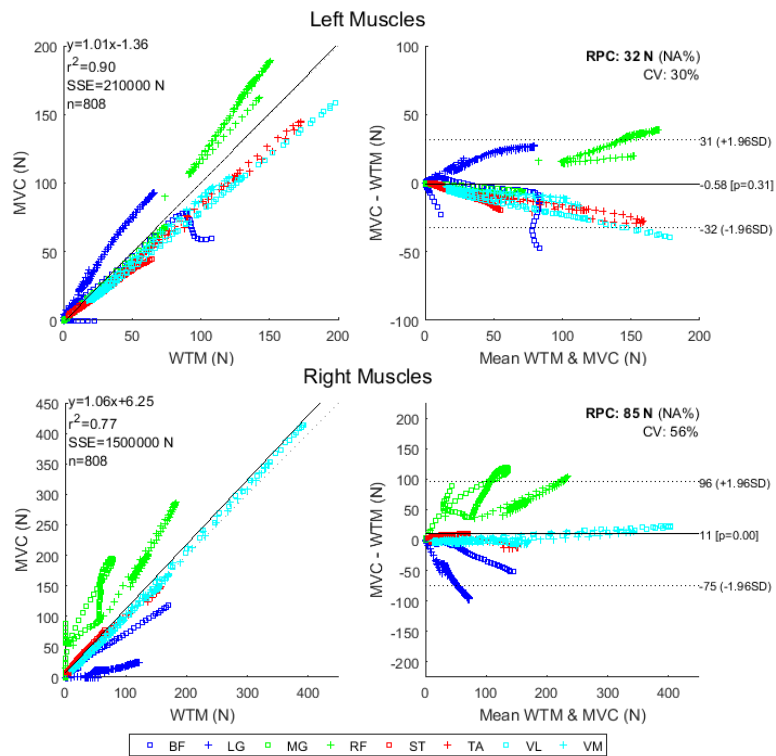


Figure 113: BA plot for AKP 29 session one normalisation muscle forces

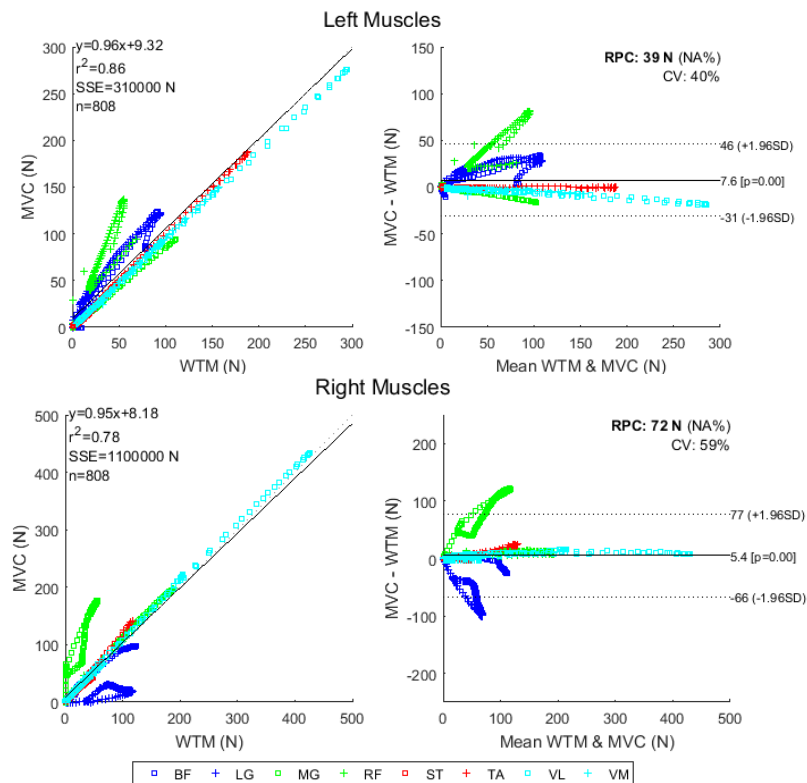


Figure 114: BA plot for AKP 29 session four normalisation muscle forces

Appendix E. Muscle force results



Figure 115: Legend for the muscle force plots

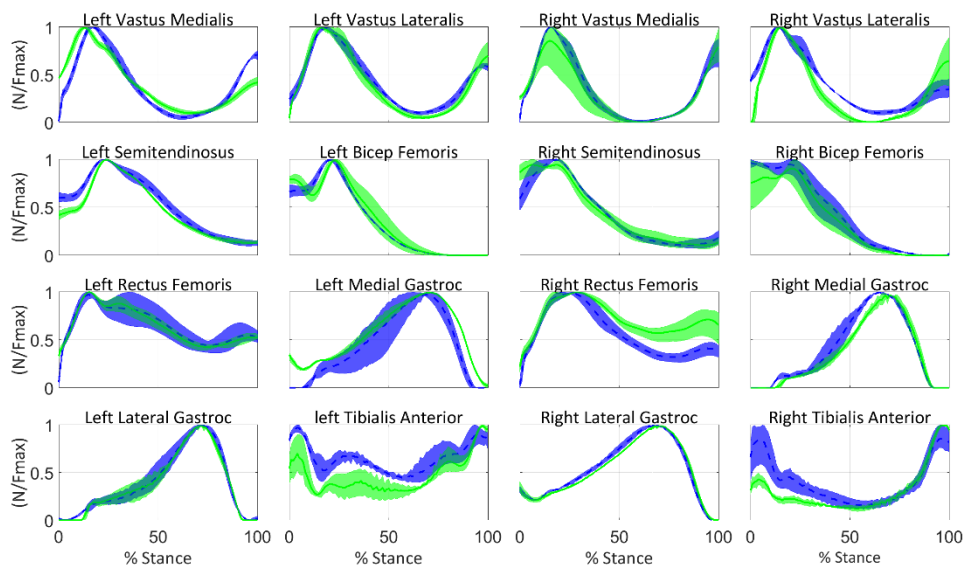


Figure 116: AKP 17 muscle forces

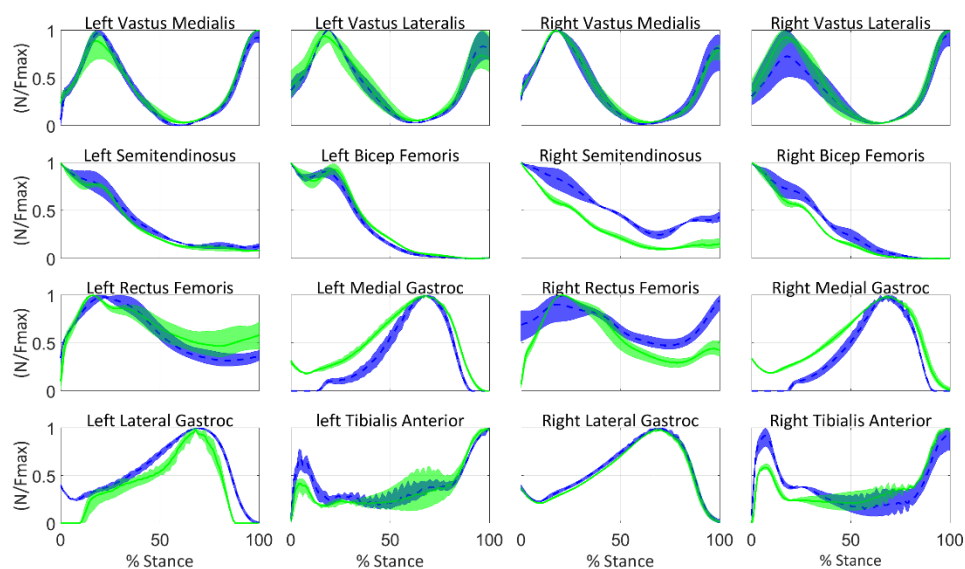


Figure 117: AKP 30 muscle forces

Appendix F. Folder layout

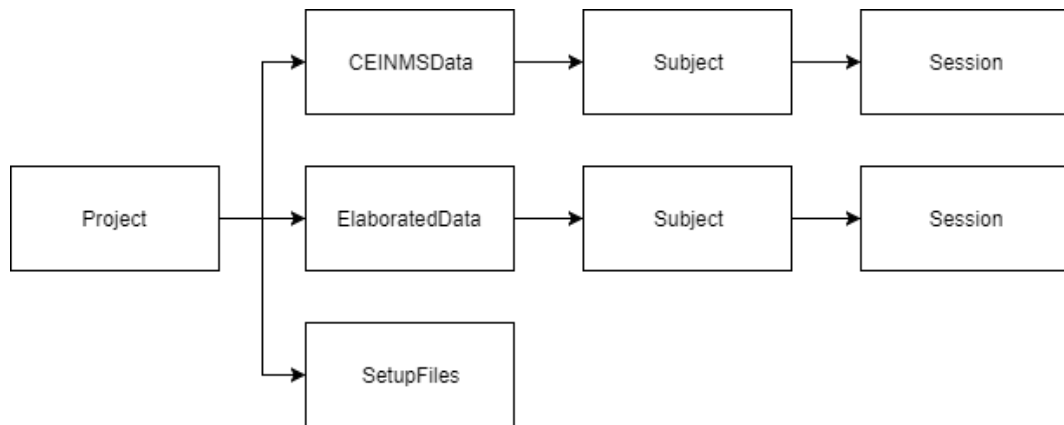


Figure 118: Outer project folder

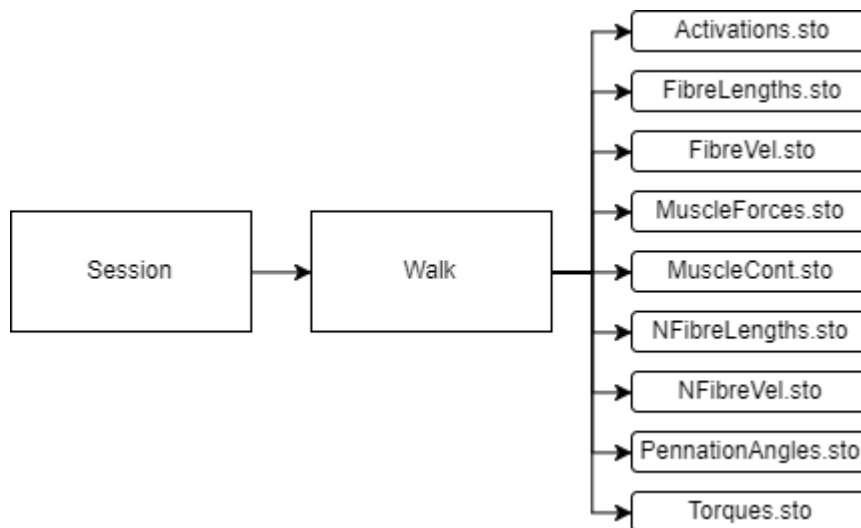


Figure 119: Session folder layout within CEINMS Data folder

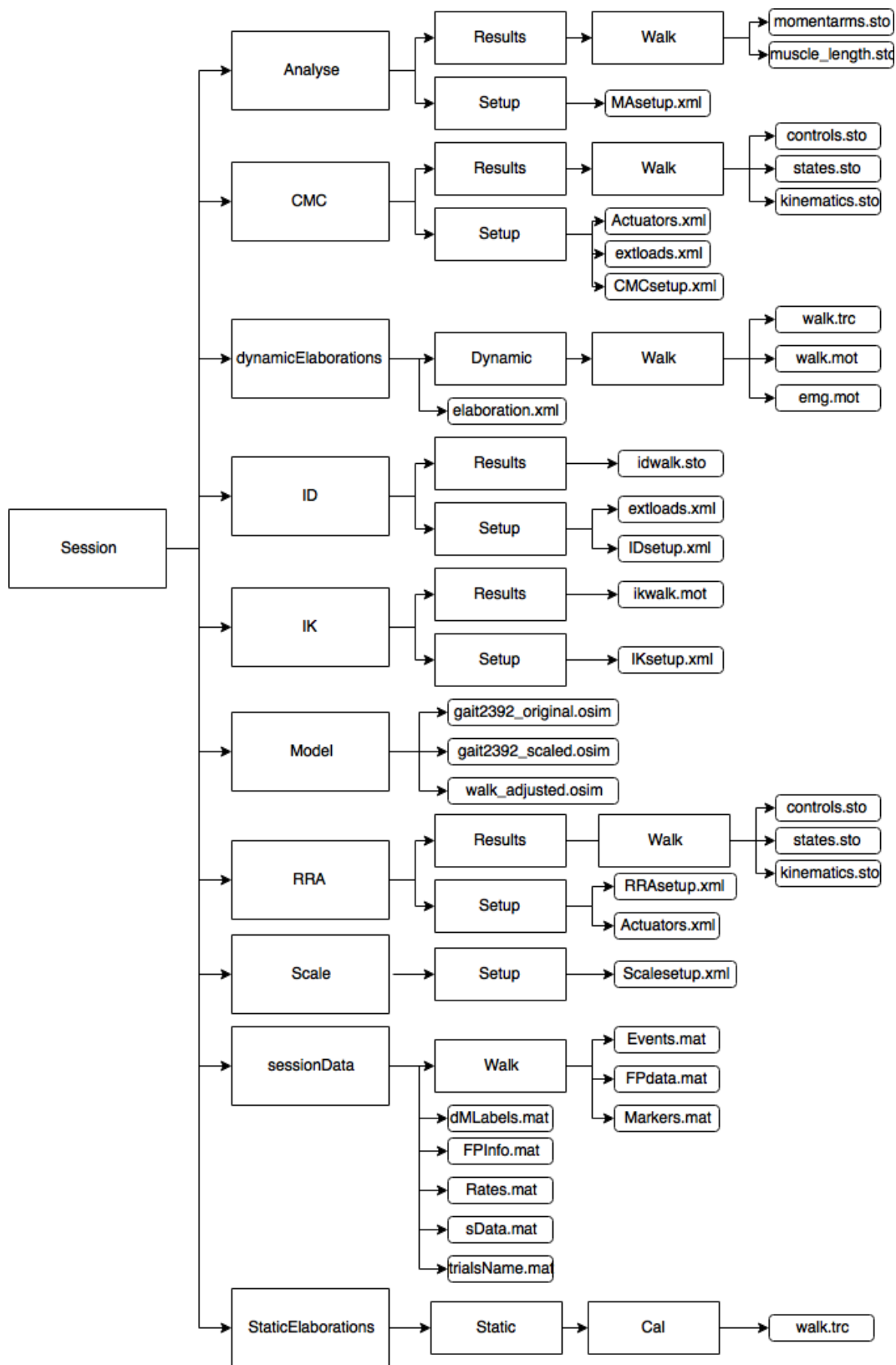


Figure 120: Session folder layout within Elaborated Data

Appendix G. Computational pipeline diagrams

G.1. MOtoNMS

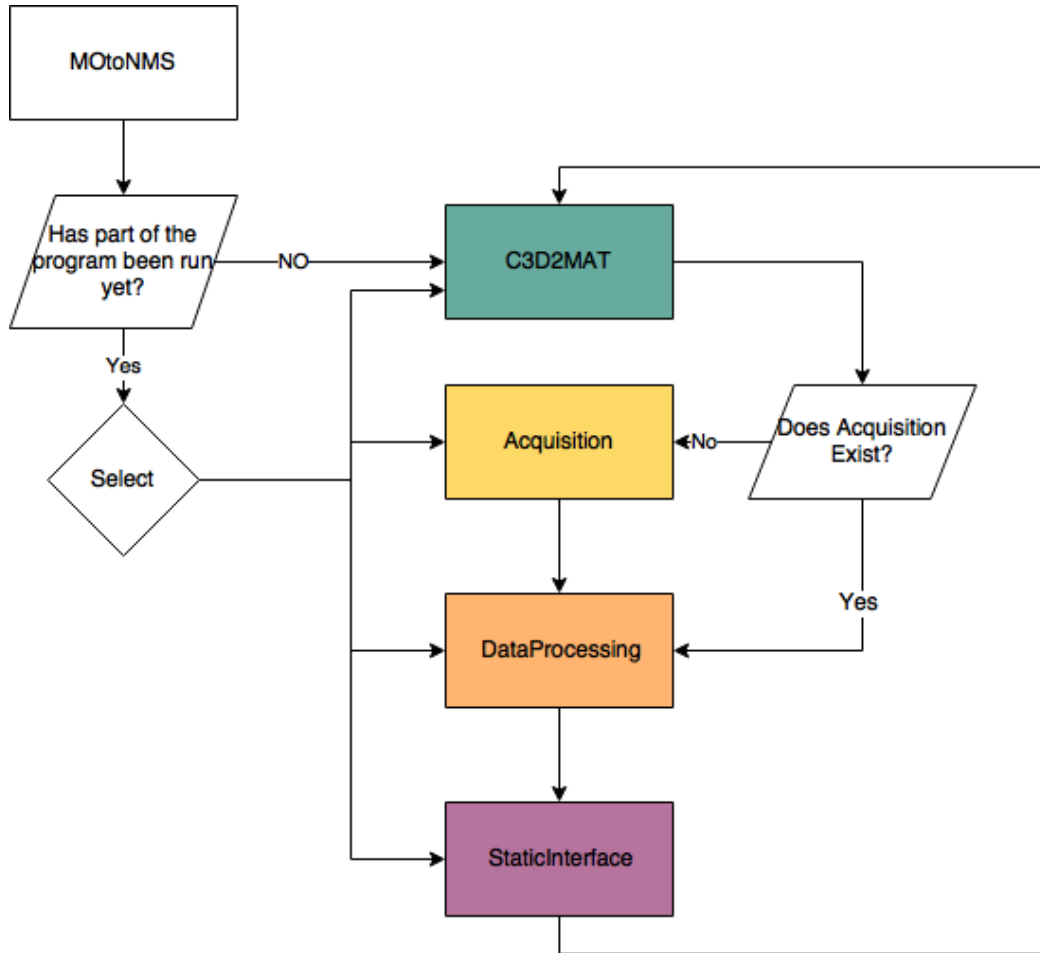


Figure 121: MO to NMS outer code flow diagram

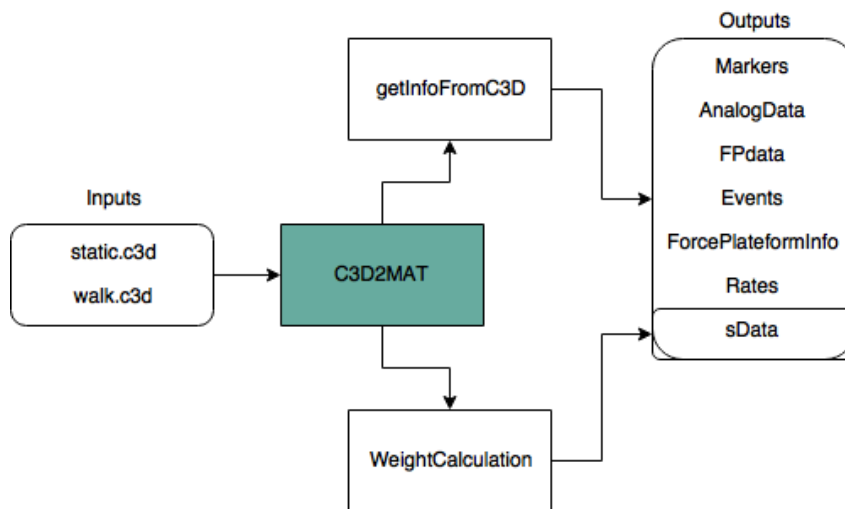


Figure 122: C3D2MAT flow diagram

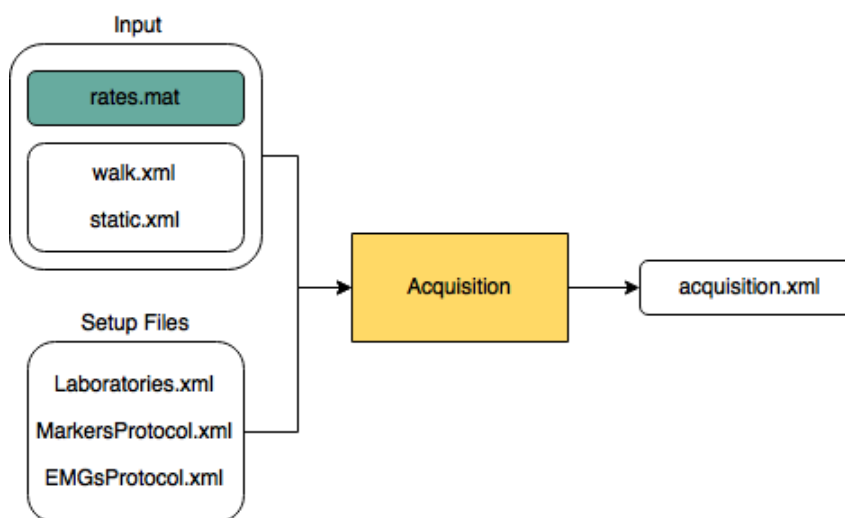


Figure 123: Acquisition flow diagram

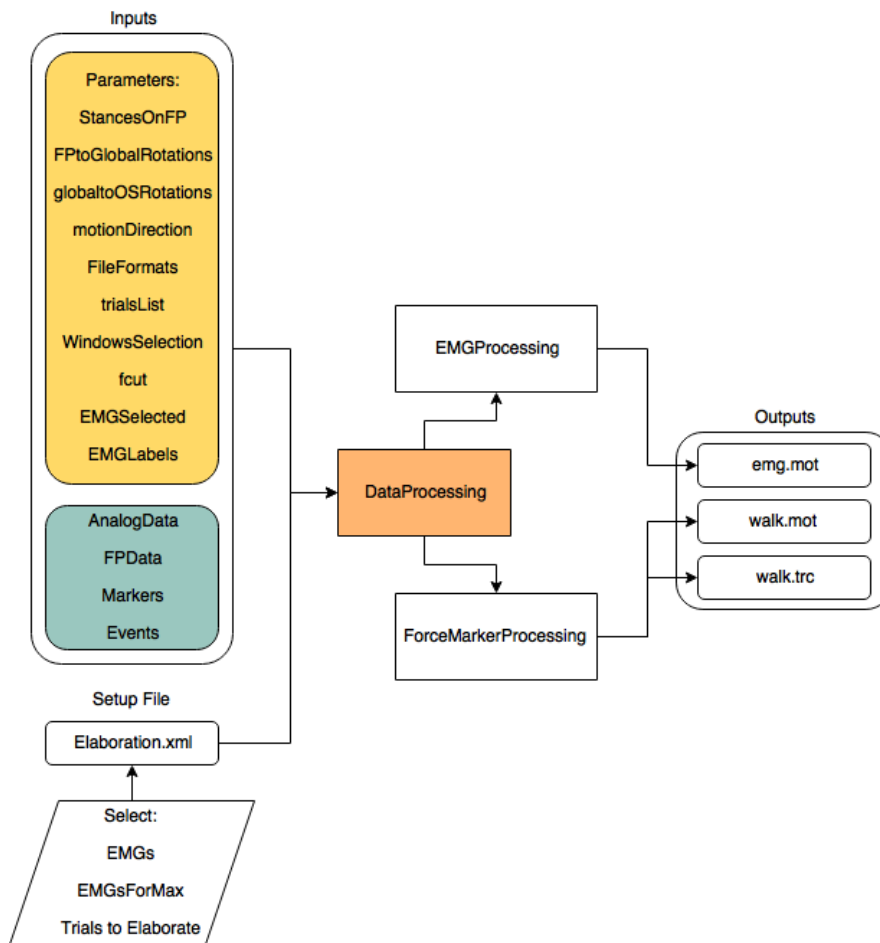


Figure 124: Data Processing flow diagram

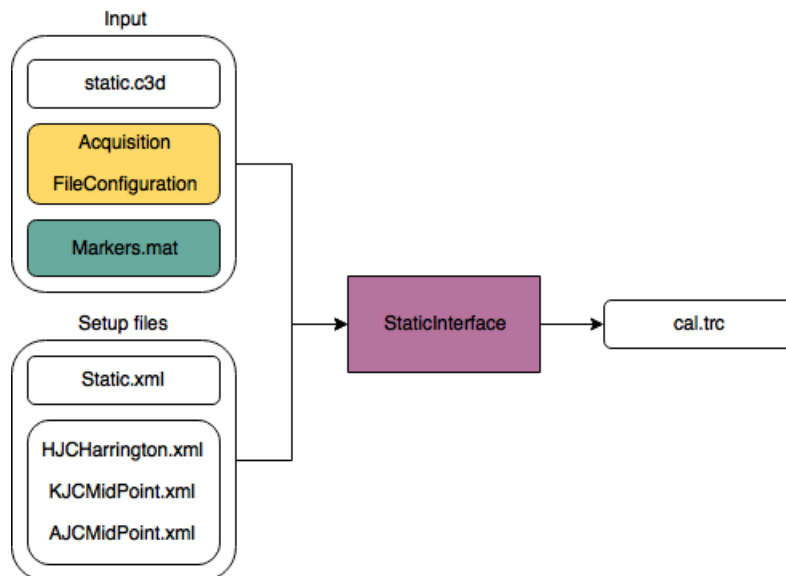


Figure 125: Static Interface flow diagram

G.2. OpenSim

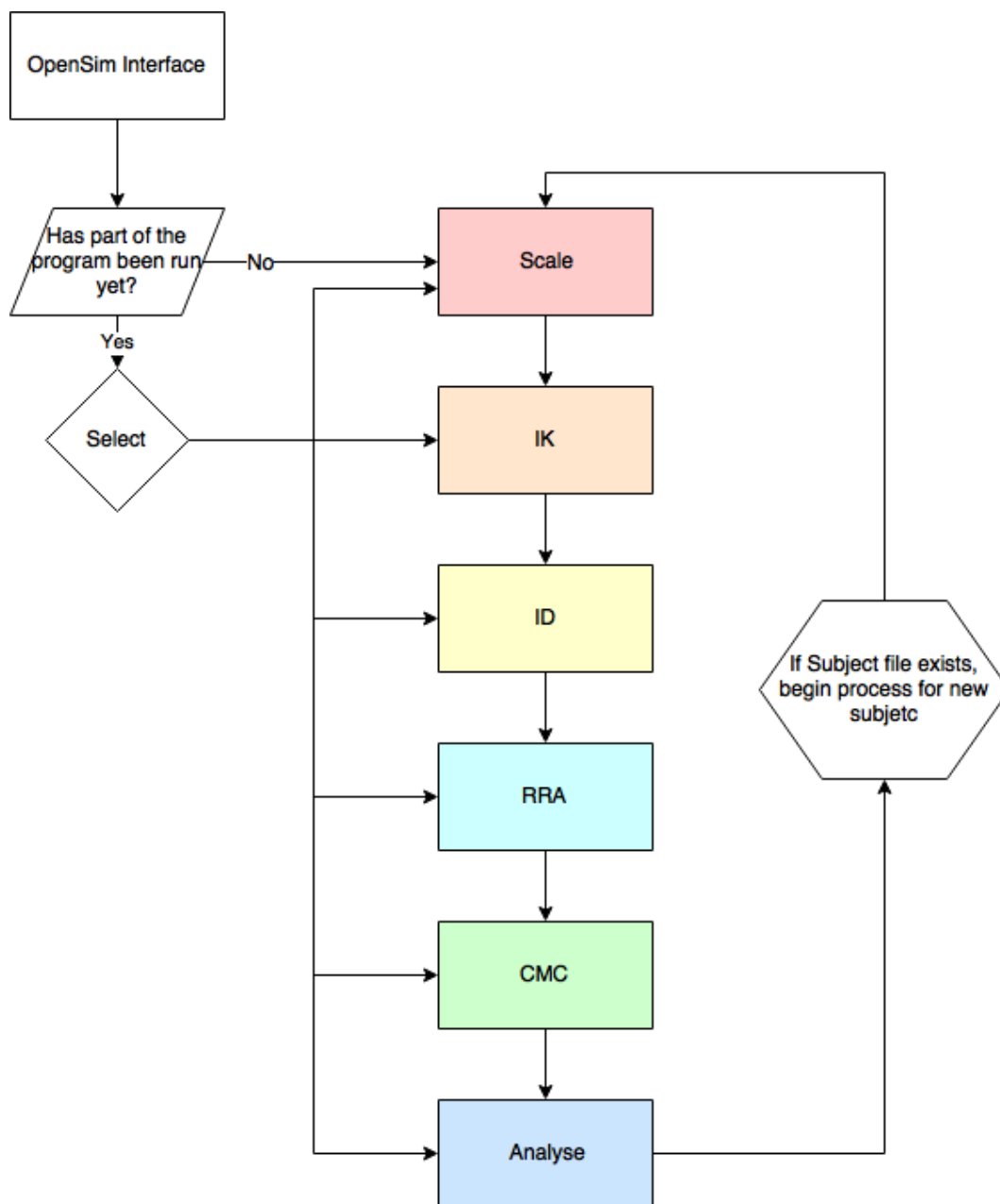


Figure 126: OpenSim flow diagram

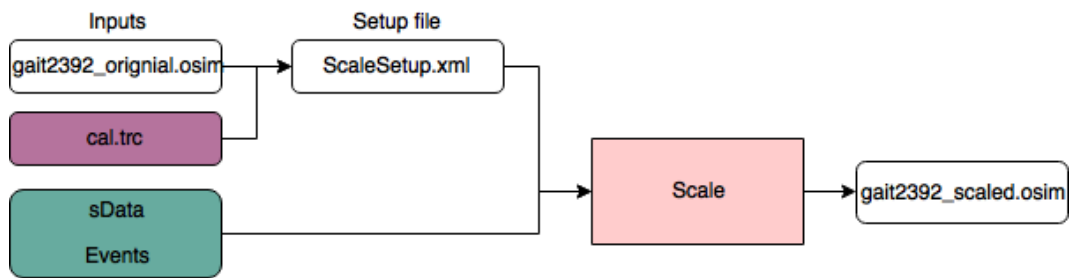


Figure 127: Scale flow diagram

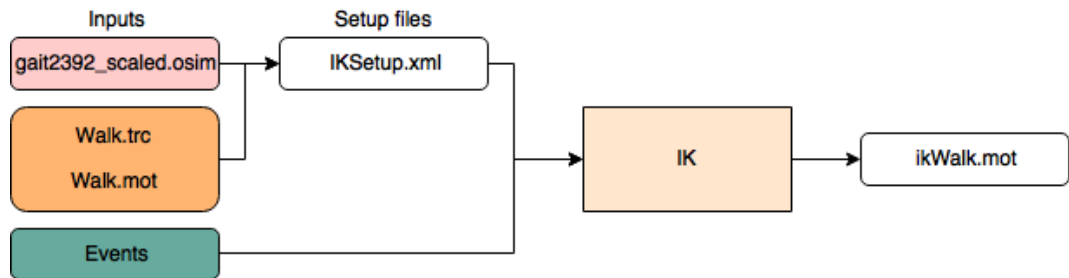


Figure 128: IK flow diagram

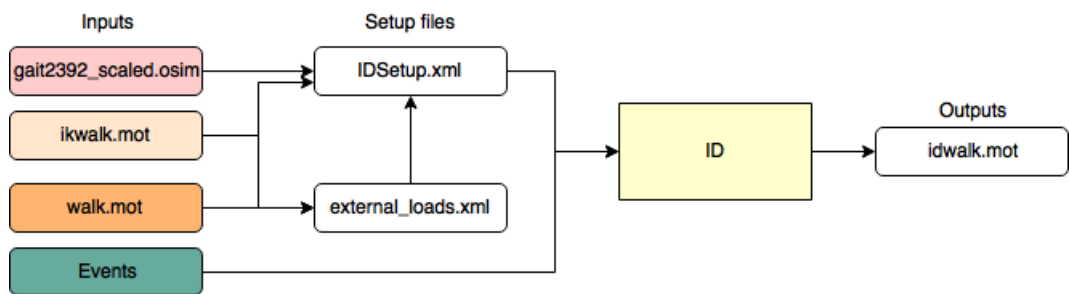


Figure 129: ID flow diagram

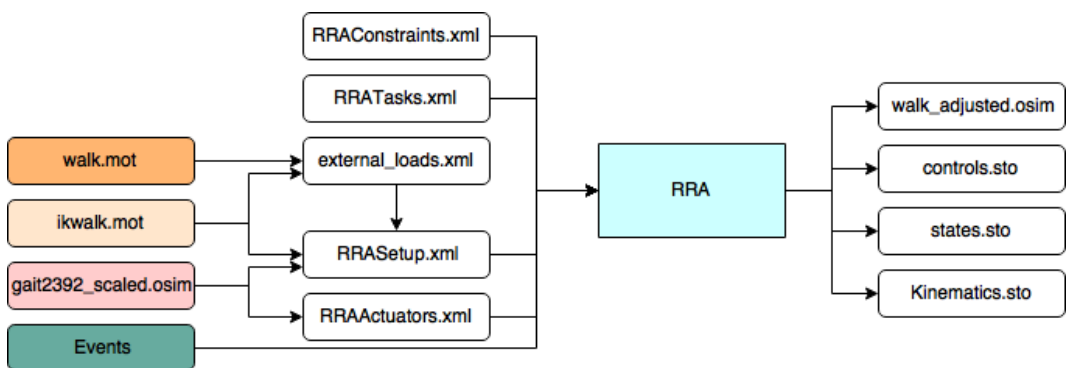


Figure 130: RRA flow diagram

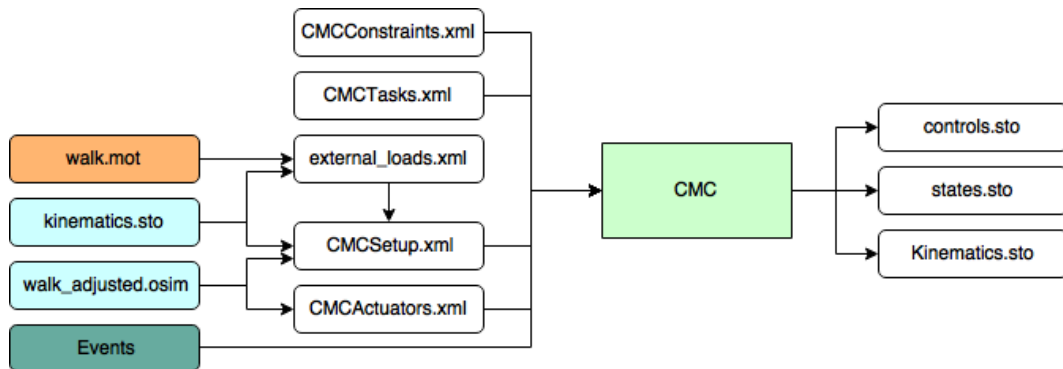


Figure 131: CMC flow diagram

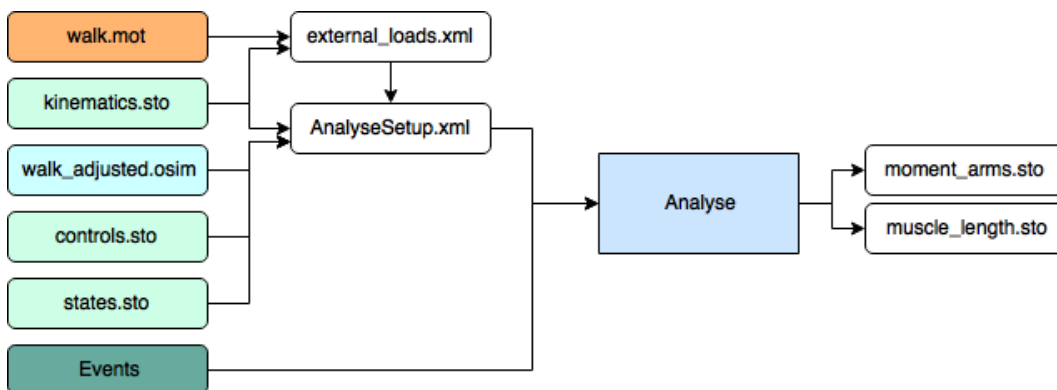


Figure 132: Analyse flow diagram

G.3. CEINMS

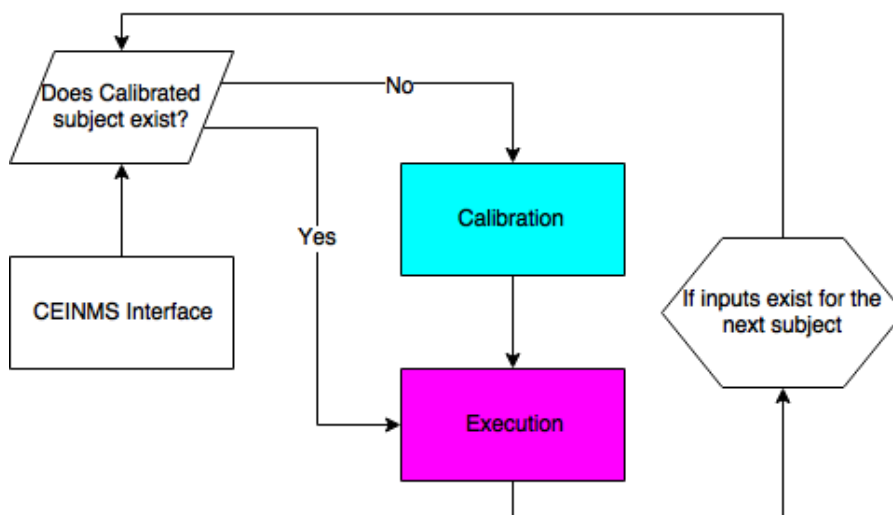


Figure 133: CEINMS outer flow diagram

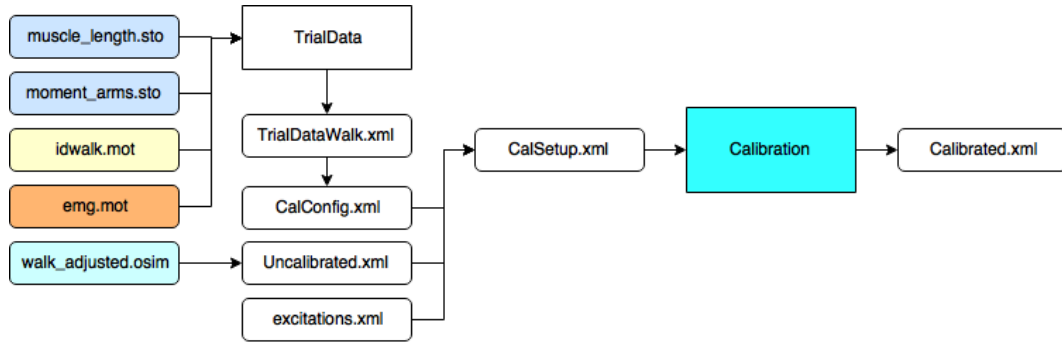


Figure 134: Calibration flow diagram

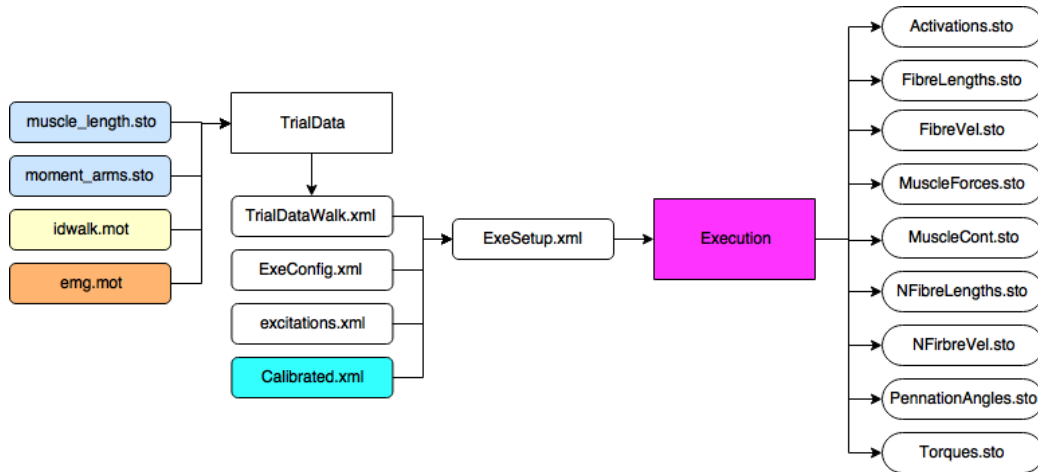


Figure 135: Execution flow diagram